Alma Mater Studiorum · University of Bologna

School of Science
Department of Physics and Astronomy
Master Degree in Physics

Fabrication by magnetron sputtering and characterization of electrodes based on $\mathbf{CuIn_{0.7}Ga_{0.3}Se_2}$ (CIGS)

Supervisor:
Prof. Luca Pasquini

Co-supervisor:
Dr. Alberto Piccioni

Submitted by:
Lorenzo Bellagamba

Academic Year 2021/2022

Contents

Abstract

This thesis work aims to produce and test multilayer electrodes for their use as photocathode in a PEC device. The CONDOR research project aims to create a photosynthetic device composed of two compartments, one of which is a photoelectrochemical cell (PEC) that splits water and CO_2 generating oxygen and syngas (mixture of H_2 and CO). My contribution to this research project concerns the realization and characterization of the photocathode using abundant and low cost elements that allows to achieve a sufficient current-density (about 10-15 mA/cm^2) and stability over time.

The electrode developed is based on CIGS, a I-III-VI_2 semiconductor material composed of copper (Cu), indium (In), Gallium (Ga) and selenium (Se). It has a bandgap in the range of 1.0-2.4 eV and an absorption coefficient of about $10^5 cm^{-1}$, which makes it a promising photocathode for PEC water splitting. The idea of our multilayer electrode is to deposit a thin layer of CdS on top of CIGS to form a solid-state p–n junction and lead to more efficient charge separation. In addition another thin layer of AZO (Aluminum doped zinc oxide) is deposit on top of CdS since it would form a better alignment between the AZO/CdS/CIGS interfaces, which would help to drive the charge transport further and minimize charge recombination. Finally, a TiO_2 layer on top of the electrodes is used as protective layer during the H_2 evolution. FTO (Fluorine doped tin oxide) and Molybdenum are used as back-contact.

We used the technique of RF magnetron sputtering to deposit the thin layers of material. In detail, we deposited with a base pressure of $8 \cdot 10^{-3}$ mbar, and an argon flux of 20 sccm. The different layers are deposit with different parameters of RF power, chamber temperature and deposition time: CIGS at a power RF = 80W, T = 350°C, t = 4h (film thickness $\simeq$ 900 nm and deposition rate $\simeq$ 0.625 Å/s); the CdS at a power RF = 30W, T = RT, t = 1:30h (film thickness $\simeq$ 50 nm and deposition rate $\simeq$ 0.093 Å/s); the AZO at a power RF = 40W, T = RT, t = 2:20h (film thickness $\simeq$ 80 nm and deposition rate $\simeq$ 0.095 Å/s); the TiO_2 at a power RF = 75W, T = RT, t = 45min (film thickness $\simeq$ 50 nm and deposition rate $\simeq$ 0.185 Å/s).

The structural characterization performed by XDR measurement confirm a polycrystalline chalcopyrite structural with a preferential orientation along the (112) direction for the CIGS. From linear fit of the Tauc plot, we get an energy gap of about 1.16 eV. In addition, from a four points measurements, we get a resistivity of 0.26 Ωcm.

We performed an electrochemical characterization in cell of our electrodes. The results show that our samples have a good stability but produce a photocurrent of the order of μA, three orders of magnitude smaller than our targets. The EIS analysis confirm a significant depletion of the species in front of the electrode causing a lower conversion of the species and less current flows.

1. Introduction

With a growing population and energy demand in the world, there is a pressing need for research to create secure and accessible energy options with greatly reduced emissions of greenhouse gases. While we work to deploy the clean and efficient technologies that we already have, which will be urgent for the coming decades, we must also work to develop the science for the technologies of the future.

1.1 The energy challenge

Secure, reliable and affordable energy resources are fundamental to sustained economic development. The threat of disruptive climate change and the world's growing demand for energy are the main features of the energy challenge. To meet these challenges and transform our energy system, better use of existing technologies will be required along with significant scientific innovation to spur the adoption of new energy technologies.

At the beginning of the 21st century, there are a number of potential scientific innovations that could provide solutions to our energy challenges. There are opportunities stemming from innovations in technologies and instrumentation, computing, communications, biotechnology, nanosciences, information technologies, and infrastructure. Together, these opportunities would accelerate scientific progress, and bring new discoveries to the market faster and at lower cost.

The most delicate challenge will be to avoid the use of fossil fuels in order to reduce their impact on the environment. The main concern in this regard is the emission of greenhouse gases, in particular CO_2, and their contribution to global warming (Figure 1). Such a rise is likely to have a severe adverse impact on ecosystems and human society, with effects that will be felt throughout the century. To reduce our dependence on fossil fuels and curb the exhaust of CO_2, we need to make a large-scale transition toward new, sustainable sources of energy. While most scientists and politicians nowadays agree that such a transition is unavoidable, there is much uncertainty about the route to follow, and the speed at which this can and should be done. More often than not, the viability of a certain route is determined by economical considerations, rather than technological impediments, so the cost will be a crucially important factor for the challenge to sustainable sources of energy.[1]

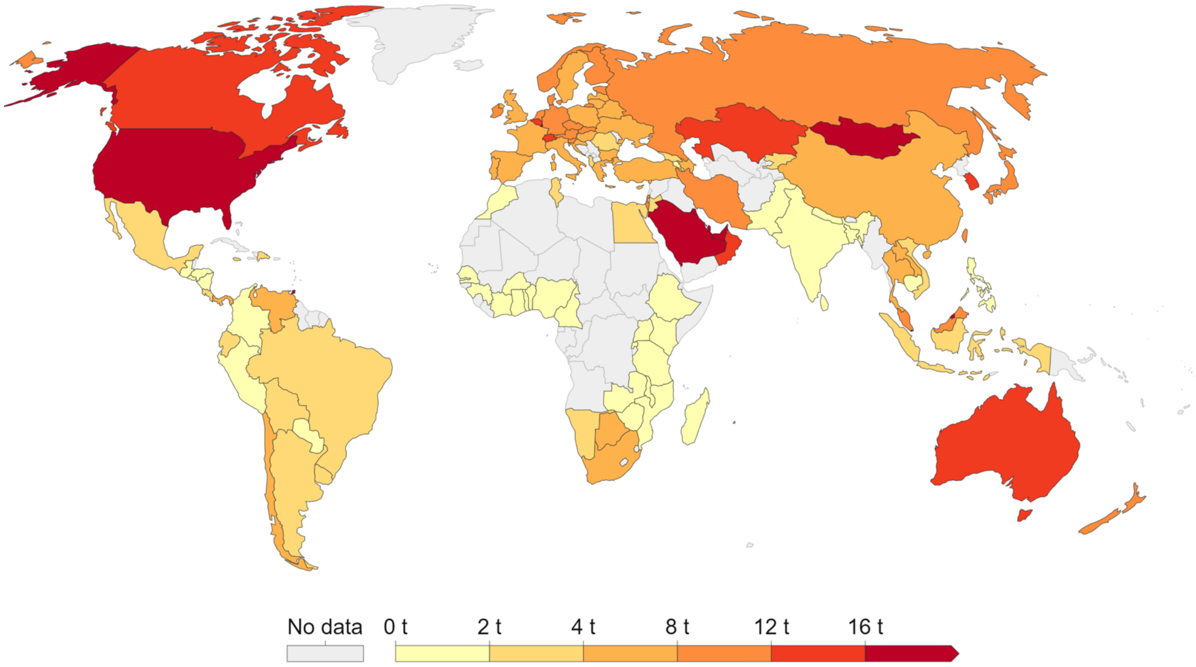

Figure 1: Annual consumption-based carbon dioxide (CO_2) emissions, measured in tonnes per person. Consumption-based CO_2 emissions have been converted from tonnes of carbon to tonnes of CO_2 using a conversion factor of 3,664.[2]

2. Photoelectrochemical cell

Photoelectrochemical (PEC) water splitting has been attracted significant attention lately due to its utilization of solar energy and H_2 production.

This chapter provides a review of the principles and prospect of PEC as solution for the energy problem.

2.1 Solar energy conversion

The solar cell market is one of the fastest growing markets today. It's hard to predict how this market will develop in the next few decades, but there's no doubt that solar energy is an important component in solving the energy problem. One of the most interesting possibilities for large-scale energy storage is to store solar energy in the form of chemical fuel. The energy of a photon at visible light varies between 1 and 3 eV, or 100-300 kJ/mol, which is more than enough for many chemical synthesis. Based on these considerations, the conversion of solar energy into hydrogen seems to be the most interesting path. Water is a convenient and abundant source of hydrogen, and there is plenty of water available (about 0.01% of the annual rainfall fall is enough to store the energy that the world uses in a year)[3]. The water splitting reaction can be seen as in Figure 2. The reduction half-reaction is an easy two-electron transfer reaction, while four electrons are involved in the oxidation of water to form oxygen.

One of the main concerns associated with hydrogen is the difficulty of storing it. An excellent solution is to store hydrogen by forming chemical bonds, in the form of metal hydrides, or by using hydrogen and CO_2 to produce chemical fuels. The latter is much simpler than the direct photochemical or electrochemical activation of CO_2. For example, CO_2 and hydrogen can be converted to CO by the slightly endothermic water-gas reversal reaction:

$$CO_2 + H_2 \Longleftrightarrow H_2O + CO \quad \Delta H = +42 \ kJ/mol \tag{1}$$

The CO and H_2 (syngas) can be separated out with a membrane and converted to liquid hydrocarbon fuels, such as methanol and diesel.

2.2 Photoelectrochemical water splitting

Many pathways exist for the conversion of water and sunlight into hydrogen, here we focus on the photoelectrochemical water splitting.

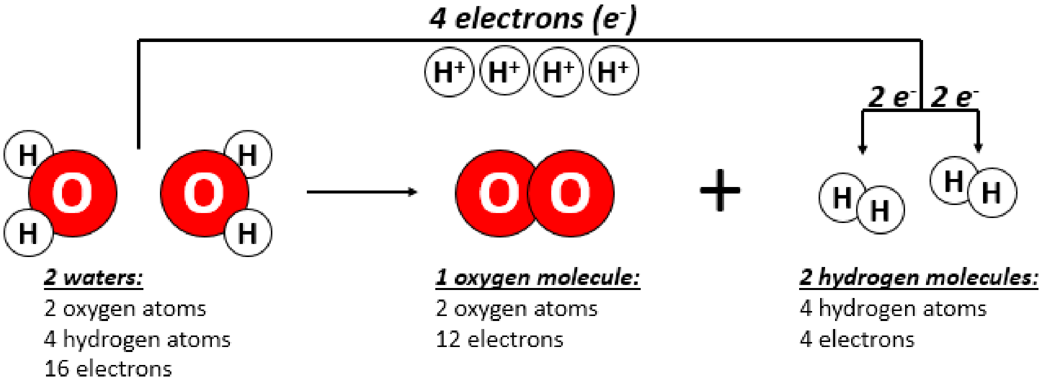

Figure 2: Water splitting reaction.[4]

There are several reasons why this approach is attractive. One of the main advantages is that hydrogen and oxygen are produced by separate electrodes. This avoids serious safety problems and allows easy separation of these gases without having to pay a heavy energy penalty for post-separation. A second advantage is that it can be carried out at room temperature, that is, there is no need for large-scale solar concentration that would limit its application. A third advantage is that a Photoelectrochemical water splitter can be constructed entirely from inorganic materials. This offers a degree of chemical strength and durability that is difficult to achieve for organic or biological systems. In addition, the current density in a semiconductor photoelectrode immersed in water is very small (10-20 mA/cm^2 maximum) and therefore the required overpotential.[3] Finally, a PEC system requires fewer packaging components, resulting in significant cost savings.

Photoelectrochemical splitting of water is based on the conversion of photons incident on the surface of a semiconductor into the electrochemical energy that can directly split water into molecular H_2 and O_2 (Figure 3). The essence of this reaction lies in the generation of minority charge-carriers upon illumination, i.e., electrons for p-type semiconductor and holes for n-type semiconductor, followed by the subsequent charge-migration. The migrated minority charge-carriers carry out the necessary electrochemical reactions at the electrode surfaces, leading to the reduction of water on p-type semiconductor, and the oxidation on n-type semiconductor, respectively. The following processes, take place in a photoelectrochemical cell: a) absorption of light b) charge generation c) charge separation d) charge transportation, and e) chemical reactions at the electrode surfaces.

Electrons get excited to the conduction-band upon illumination, leaving behind positively charged holes in the valence-band. A portion of these photogenerated charge-carriers migrates to the semiconductor/electrolyte interface due to the built-in electric field in the depletion region to carry out the desired chemical reactions. The built-in

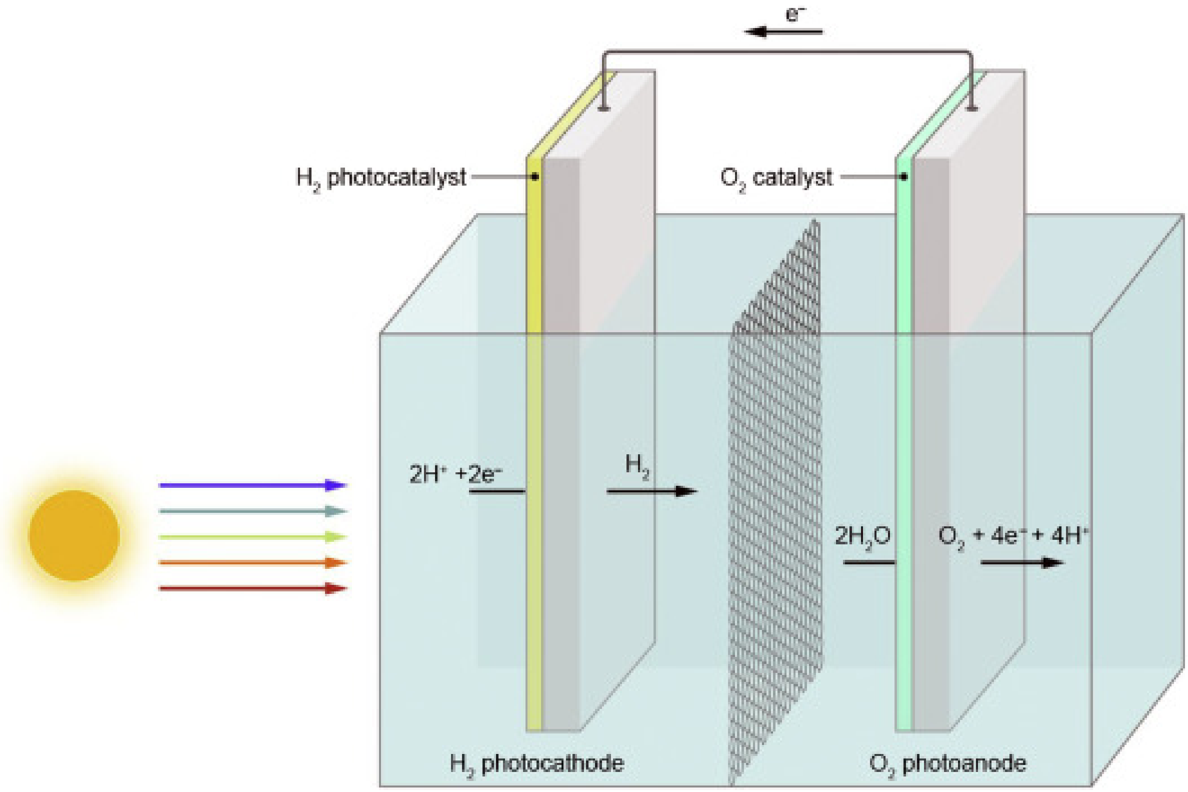

Figure 3: Schematic of a tandem photoelectrochemical cell. The photocathode where H_2O is reduced to H_2, and the photoanode, where water is oxidized to produce O_2.[5]

electric field in the depletion-region is formed due to the potential difference between the Fermi-level of semiconductor and the redox-potential of water. The reduction of water to generate hydrogen, known as hydrogen-evolution reaction (HER), and the oxidation of water to form molecular oxygen, oxygen-evolution reaction (OER), can be written as:

$$HER: \quad 2H^+ + 2e^- \longrightarrow H_2(g) \tag{2}$$

$$OER: \quad 2H_2O \longrightarrow O_2 + 4H^+ + 4e^- \tag{3}$$

$$Overall: \quad 2H_2O \longrightarrow O_2 + 2H_2 \quad \Delta E = -1.23V \tag{4}$$

The rest of the separated charge-carriers undergo recombination in bulk and release their energy thermally in the form of phonons, which ultimately hampers the overall activity of the photoelectrode.[6]

At standard temperature (298 K) and concentrations (1 mol/L, 1 bar), the electrochemical cell voltage ΔE of -1.23 V corresponds to a Gibbs free energy change of +237 kJ/mol H_2. This shows that the water-splitting reaction is thermodynamically uphill. In practice, the overpotential losses caused due to the impedances and photocorrosion, and the kinetic and mass-transport losses caused due to the generation of gas bubbles at the electrode surfaces, raise the potential-barrier for a successful water-splitting reaction.[3] In general, the photoelectrode materials should be able to generate the photovoltage of 2.0 V vs. RHE and 1.2 V vs. RHE, for photoanode and photocathode, respectively.[3] Hence, for hydrogen generation through PEC water-splitting, the use of appropriate photoelectrode materials is of prime importance.

2.2.1 The PEC process

Under irradiation, PEC water splitting involves important processes such as photon absorption, charge separation and the extraction of electrons and holes to the photoelectrodes for H_2 and O_2 evolution reactions. Each step has important influences on the overall performance of the system. In order to understand the system, it helps to examine each step separately.

1. **Photon absorption**. In order to maximize energy conversion efficiencies, the morphology, dimensionality and crystallinity of the semiconductor with an appropriate bandgap should be engineered to improve the light absorption and increase the photocurrent. An important parameter, the bandgap of a semiconductor, can be determined from the equation of the absorption coefficient. The absorption coefficient (units: m^{-1}) can be expressed as follows:

$$\alpha = \frac{A(h\nu - E_g)^m}{n\nu} \tag{5}$$

where A is a constant and m depends on the nature of the optical transition: m = 1/2 for a direct bandgap, and m = 2 for an indirect gap.

From Equation (5), the extrapolation of a plot of $(\alpha h\nu)^{1/2}$ vs. $h\nu$ plot gives the indirect bandgap, while a plot of $(\alpha h\nu)^2$ vs. $h\nu$ yields the direct bandgap of the material. Such a plot is known as "Tauc's plot." The absorption coefficient of indirect bandgap semiconductors is typically smaller than that of direct bandgap semiconductors (the difference can be up to two orders of magnitude or greater). Considering indirect semiconductors, the direction transition from the top of the valence band, E_v, to the bottom energy of the conduction band, E_c, is not permitted due to momentum mismatch. As such, the absorption of photons with energies close to the bandgap requires interactions between electrons and the lattice vibrations (phonons) and are much less likely to occur (Figure 4).[3] The electron–phonon interaction is not necessary for photon absorption by direct bandgap materials, so these materials typically feature high absorption coefficients.

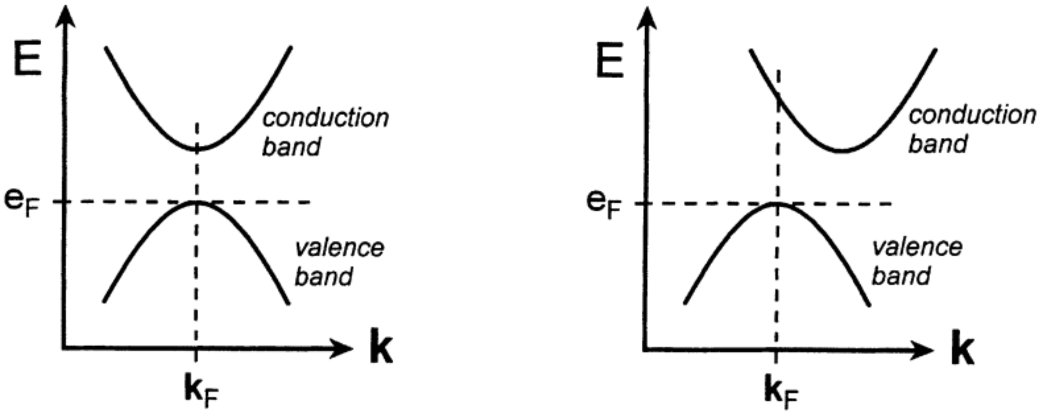

Figure 4: Optical transitions in semiconductors with a direct and an indirect bandgap. The indirect transition requires assistance of a phonon.[7]

2. **Photoelectrode junction formation**. In PEC photoelectrode systems, the semiconductor/electrolyte interface can form a rectifying junction, similar to the solid-state pn junctions or Schottky diode junctions used in solar cells. Such rectifying junctions exhibit built-in electric fields capable of separating photogenerated charge carriers (i.e., electron–hole pairs) created by absorption of photons in the semiconductor bulk. In PV cells, this charge separation mechanism drives photocurrents to produce electricity, while in the PEC case, the charge separation can drive the HER and OER half-reactions for water splitting. In both cases, illumination creates extra photoexcited electron–hole pairs which need to be separated and extracted before they recombine in order to be effective in the energy conversion process. Extraction of the photogenerated charge carriers with elevated electrochemical po-

tentials converts the solar energy to electricity or hydrogen in PV or PEC systems, respectively.

The descriptions of semiconductor/electrolyte junctions follow closely the solid-state junction analogies. Photoanodes using n-type semiconductors form PEC junctions similar to a Schottky barrier or an np^+ junction, and internal electric fields are set up to drive photogenerated holes toward the electrolyte interface promoting oxygen evolution. In contrast, p-type photocathode junction formation is analogous to a solid-state pn^+ device, and the internal fields promote the injection of photogenerated electrons at the interface to drive the HER.[7]

Specific steps in semiconductor/electrolyte junction formation are illustrated in Figure 5 for both the photoanode (5a) and photocathode (5b) cases. In Figure 5a (i), the n-type semiconductor and electrolyte are shown in thermal equilibrium prior to contact for the photoanode case. At equilibrium, the Fermi level in the semiconductor (F_n) is close to the conduction band (CB), and the Fermi level in solution (F_s) falls between the redox (reduction/oxidation) levels for hydrogen reduction (H^+/H_2) and water oxidation (H_2O/O_2). After contact, the electrode and electrolyte Fermi levels align to reach thermal equilibrium, as shown in Figure 5a (ii). Since the initial electrode Fermi level is higher than the electrolyte Fermi level, free electrons in the n-type semiconductor will migrate to the solid–liquid interface. Thus, the majority carrier of electrons will flow from the semiconductor to the electrolyte after contact until the Fermi level of the semiconductor and the electrochemical potential of the electrolyte are aligned. The energy bandedges in the semiconductor are also shifted due to the change of carrier concentrations, the band bending occurs. The ionized donors stay inside the semiconductor and create a positively charged region, whereas negative charges concentrate on the interface within the electrolyte. Consequently, an electric field forms at the interface. This field counter-balances continuous flow of charges, reaching a dynamic equilibrium. The electrons form a surface charge layer at the interface which induces a thin Helmholtz layer in the electrolyte, basically similar to a capacitor. A depletion-region, also known as a space-charge region (SCR), forms where free charge carrier diffusion is counter-balanced by the built-in electric field generated by the fixed charges close to the junction. An important parameter, the depletion width or the space charge region width, W_{sc}, is used to describe the characteristic length of this region. W_{sc} depends on the doping density, N, the relative permittivity, ϵ, and the potential drop across the space charge region, $\Delta\phi_{sc}$, which corresponds to a band bending of $q\Delta\phi_{sc}$, as follows:

$$W_{sc} = \Big(\frac{2\Delta\phi_{sc}\epsilon\epsilon_0}{qN}\Big)^{1/2} \tag{6}$$

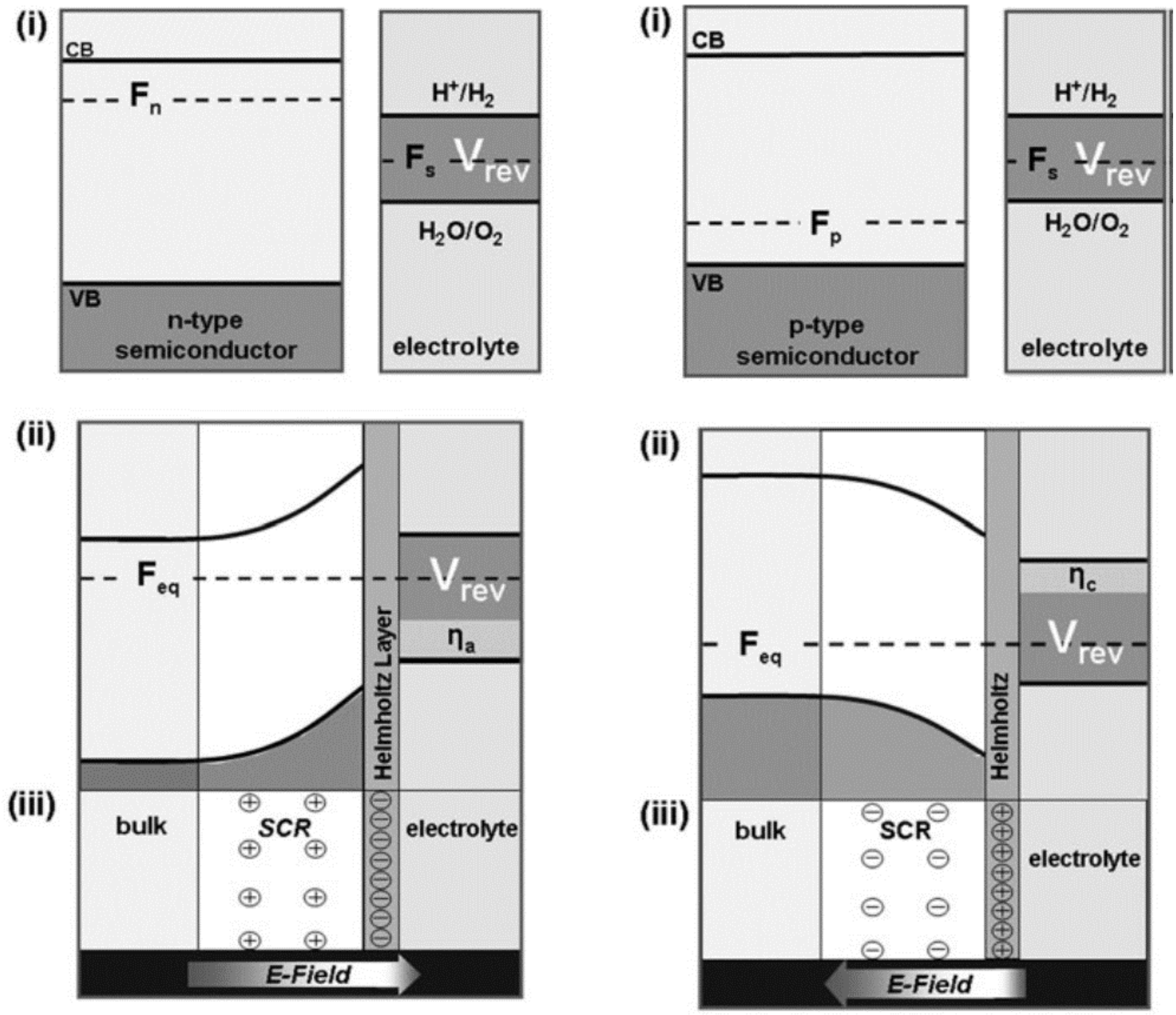

Figure 5: Semiconductor/electrolyte junction formation for (a) n-type semiconductor and (b) p-type semiconductor junction. Subheadings (i), (ii), and (iii) represent the energy diagrams before contact, the energy diagrams after contact, and the charge distributions, respectively.[]

3

The charge distributions including the fixed space charges in the solid-state electrode and the Helmholtz layer charges in solution are shown in Figure 5a (iii). Typically, Helmholtz layers are on the order of a few nm, compared with several μm for the semiconductor space-charge region. For the p-type photocathode case, the equilibrium charge distribution process is the same, but, as shown in figure, the charges and band bending are reversed. As illustrated in Figure 5b (i) and (ii), the initial migration of holes toward the interface during contact equilibration creates a space charge region of fixed negative acceptor charges, reversing the direction of the built in electric field compared with the photoanode cases. In both cases, the thermal equilibrium is disturbed upon exposure to light, and the illumination process need to be described in terms of "quasi-equilibrium" statistics.

3. **Surface state**. Surface states can be electronic states on the surface due to the termination of the lattice periodicity. They can also be due to adsorption of chemical species such as H_2O molecules (including its derivatives; e.g., OH^- and H^+). Usually, the density of surface states can be large in comparison with the bulk dopant states. Therefore, the Fermi level of the semiconductor on the surface is almost independent of the bulk doping concentration and is pinned by these surface states. Under these conditions, changes in the potentials between the semiconductor bulk and the solution will mainly affect the potential drop across the Helmholtz layer ($\Delta\phi_H$) rather than the drop within the semiconductor ($\Delta\phi_S$). Therefore, surface states with energy levels within the bandgap could reduce the built-in field and, hence decrease photovoltages and compromise the overall energy conversion efficiency. Moreover, surface states could act as recombination centers to quench photogenerated electrons and holes, which lower the utilization efficiency of these charges. Detailed knowledge of these surface states is important to the efforts of constructing photoelectrodes with optimized performance.

4. **Flat Potential**. Flatband potential, V_{fb}, describes the potential at which energy level the band is flat. It is an important measure of the equilibrium potential of the photoelectrode relative to the electrolyte. Often, V_{fb} can be inferred from the measurement of the photocurrent onset potential, V_{on}, which can be obtained directly by examining the polarization curve. The V_{on}, however, also contains information of the kinetic overpotentials and is not reliable for the extraction of V_{fb}. To correct the deficiency, one may use the Mott–Schottky method to measure V_{fb}. Based on the assumption that the change of the applied potential (V_{app}) is used to alter the width of the space charge region, its capacitance change follows the Mott–Schottky relationship as shown below:

$$\frac{1}{C_{SC}^2} = \frac{2}{\epsilon\epsilon_0 eN}\Big(V - V_{fb} - \frac{kT}{e}\Big) \tag{7}$$

From Equation (7), we can calculate V_{fb} from the intercept of C_{SC}^{-2} with the axis that measures the potential.

5. **Illuminate response**. Under illumination, the electron–hole pairs generated by photon absorption in the vicinity of the space-charge regions can be separated by the built-in electric fields. Some of the photocharges will be successfully extracted in the water splitting process, while the remainder will recombine, losing energy as radiation or heat. In the photoanode case, the photogenerated holes will be driven by the built-in field toward the electrolyte interface, where, with the appropriate energetics and kinetics, they can drive the OER oxidation reaction. At the same time, photoexcited electrons are driven toward the electrode's back contact, where they can be extracted to solution at counter-electrode surfaces appropriately conditioned to promote the HER. For photocathodes, the charge separation supplies photogenerated electrons to the hydrogen evolution process at the electrolyte interface, and drives photogenerated holes to an OER counter electrode surface. Under these operating conditions, the initial thermal equilibrium has been disturbed by the energy influx of the light, and the band descriptions with Fermi levels are no longer valid. Under conditions of quasi-equilibrium, a useful alternative description can be developed in terms of "quasi-Fermi" levels. Figure 6 illustrates PEC junction response to solar illumination for both photoanodes (6a) and photocathodes (6b) using the quasi-Fermi level descriptions. For both configurations, the photoelectrode is immersed in solution, and the back contact is connected by external wiring to a counter electrode also in solution. In addition, the η_a and η_c overpotentials for the OER and the HER in solution have been added to the reversible potential of the redox system to stress the minimum voltage requirement to sustain water splitting. With the absorption of sunlight in the semiconductor bulk, the original Fermi levels split into separate quasi-Fermi levels for electrons (F_e) and holes (F_h) resulting from the excess concentration of photogenerated electron–hole pairs over the equilibrium populations. [] For the photoanode case (6a), the excess hole population significantly alters the minority carrier distribution with respect to the equilibrium populations, while the excess electrons barely affect the majority carrier numbers. As a result, the hole quasi-Fermi level shifts substantially in contrast to insignificant change in the electron quasi-Fermi level. Conversely, in the photocathode case in (6b), there is a significant shift in the electron quasi-Fermi level, but little hole quasi-Fermi level shift. In both cases, near the back contact away from the effects of illumination, the two quasi-Fermi levels converge back to a bulk equilibrium Fermi level. The back contact potential is tied to the counter electrode potential, which under operating conditions is coupled to the back half reaction. As an important result, the quasi-Fermi separation in the semiconductor determines the usable energy for driving the front half reaction.

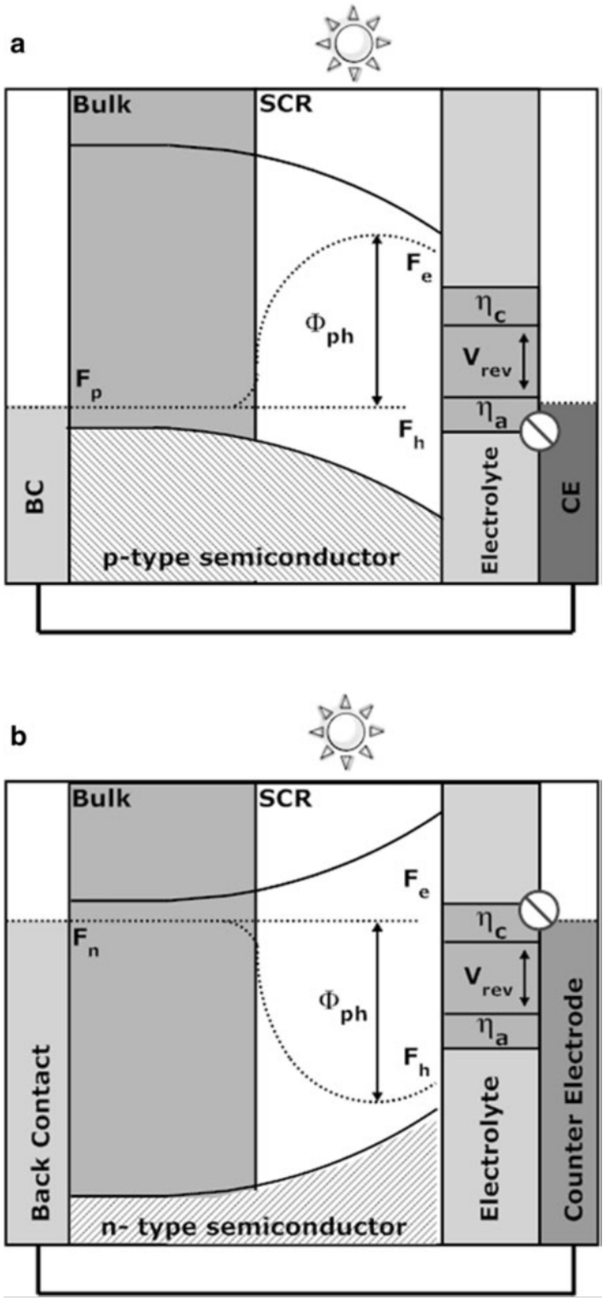

Figure 6: Operational illuminated PEC junctions (a) n-type junction with correct hole energy alignment for oxygen evolution and electron energy alignment for hydrogen production, (b) p-type junction with correct electron energy alignment for hydrogen production and electron energy alignment for hydrogen evolution.[3]

2.2.2 Semiconductor photoelectrode

There are several principles for selecting a semiconductor as a photoelectrode:

1. **Potential requirement**. Under standard conditions, the water splitting reaction can take place only when the potential difference of the two half reactions exceeds 1.23 eV (G = 237.1 kJ/mol). That is, the combined bandgap of the semiconductors should be larger than 1.23 eV. The concept of the quasi-Fermi level split is extremely important to how much usable photopotential a semiconductor device can generate, specifically in relation to the bandgap energy. Thermodynamically, semiconductor band diagram representations reflect the internal energy of electrons and holes, not the usable energy. Electricity can be extracted from a PV cell only at potentials below the open-circuit voltage, which is typically 50–70% of the semiconductor bandgap energy. The output voltage limit can be increased using higher bandgap cells, but as a tradeoff, fewer solar-spectrum photons would be absorbed, limiting the saturated photocurrent. The concept of useable potential is even more important in the case of PEC water-splitting devices. The usable potential of a PEC device must be sufficiently high to drive both half reactions in addition to the overpotential losses. This can restricts optical absorption, saturated photocurrent, and therefore, the efficiency. Other energy losses have to be taken into account, especially the overpotential loss at the electrodes and ionic conductivity loss in the electrolyte.

2. **Loss minimization**. There are numerous losses in PEC devices and systems that can limit the efficiency, and which need to be minimized. These include losses in solution, at interfaces, and in the semiconductor bulk. The optoelectronic losses in the semiconductor photoelectrode, for example, need to be as low as possible. Photons with energies below the semiconductor bandgap cannot be absorbed or converted. Photons with energies exceeding the bandgap are absorbed, but at rates dependent on the allowed transitions in the semiconductor. In all semiconductors, photogenerated electron–hole pairs rapidly thermalize to band-edge energy levels within picoseconds, losing energy to heat. Large bandgap semiconductors generate little photocurrent due to poor absorption, while small bandgap semiconductors can suffer from low conversion efficiencies due to high thermalization losses. At the band-edge energy states, the electron–hole pairs can often survive for several microseconds before recombining, and they must be separated and transported to electrochemical interfaces for extraction during this time for effective energy conversion. This separation is assisted by the electric fields set up by charge distributions in the semiconductor and at the solid/liquid interface. Defects in the bulk and at the interface can adversely affect the separation fields, and also result in poor mobility for charge transport.

To minimize overpotential loss due to interfacial charge extraction and electrochemical product formation, the interface conditions need to be optimized. Ideally, charge is extracted via the water-splitting half-reaction at the solid/liquid interface. The extraction process can be slowed or completely inhibited by poor energetic alignment or poor surface kinetics at the photoelectrode or counter electrode surfaces. Parasitic or corrosion reactions competing with the water-splitting reactions can also result in substantial loss; though surface treatments can be employed to kinetically and/or energetically favor water-splitting over the parasitic processes. Surface incorporation of nanoparticle catalysts is one approach, though light blockage due to such particles must be avoided. Since PEC water-splitting is a low-current density process, typically operating below 20 mA/cm^2, nonprecious metal catalysts can be used. Additionally, nanostructuring of electrode surfaces can increase effective surface area for enhanced charge extraction, although this can also lead to higher surface recombination loss.
Overall, the key condition for PEC hydrogen production is that the quasi-Fermi levels under solar illumination generate sufficient usable photopotential to drive the redox reactions for water splitting after all the solid-state, interfacial and solution overpotential losses have been taken into account.

3. **Appropriate band structure**. Aside from an appropriate bandgap, proper conduction and valance bandedge positions should be taken into consideration for water reduction and oxidation reactions, respectively.

4. **High crystallization and surface area**. In order to achieve efficient charge separation and collection, semiconductors with high crystallinity for charge transport and high surface activities for the OER/HER reactions are desired.

5. **Stability**. Stability is of paramount importance to the application of solar water splitting. The optimized photoelectrode material should be stable in electrolytes of a certain pH range, often in the extreme acidic or basic regime. Effective protection may be needed to prolong the lifetime of the photoelectrodes. For this purpose, an optically transparent protective layer that does not compete with the photoelectrode in absorbing light is needed.

6. **Low cost**. Low cost is yet another critical consideration. For large-scale implementations, we need materials composed of earth abundant elements.

In summary, the ideal photoelectrode fulfills several tasks at once: light absorption, charge separation, charge transport, and H_2 or O_2 evolution at its surface. Moreover, it needs to be stable in an aqueous solution, and have the potential to be made at low cost. No semiconducting material has yet been found that comes even close to meeting these contradictory demands. This means that trade-offs have to be made, leading to the development of composite photoelectrodes in which different materials fulfill different functionalities.[8]

2.2.3 The evaluation of electrochemical performances

[9] In order to evaluate the electrochemical performance of the photoelectrode, a PEC cell device should be constructed which consists of a work electrode (photoelectrode), a reference electrode, a counter electrode and an electrolyte.

1. **Potential–current curves**. First, we need to record the potential–current curves by applying an external potential bias to the cell and measuring the passing photocurrent. All potentials should be normalized to a common standard reference. For water splitting, the RHE potential is most popularly used. From the potential–current curve, we obtain the onset potential, the fill factor and the photocurrent at a given potential. Repeating the potential–current curve can help us to analyze the stability of the photoelectrode. For comparison,the polarization curve of the photoelectrode in dark condition is also included.

2. **Stability**. In order to assess the dynamics of water oxidation, we will perform photocurrent intensity vs. time measurements. During stability tests, the photoelectrode are continuously irradiated by a simulated solar light, and the photocurrent density–time curves are recorded. In addition, these measurements will be repeated at the end of characterization. If the photoelectrode is not stable in electrolyte or the catalyst is detached from the photoelectrode, obvious decay would be observed.

3. **Photocurrent Transients**. The photocurrent–voltage curve is sometimes recorded while switching the light on and off. Small differences between the dark current and the photocurrent can be easily observed with this technique, and this can help to accurately determine the photocurrent onset potential. Such transients are often observed and indicate recombination of the photogenerated charge carriers. This recombination can be due to accumulation of holes near the surface, accumulation of electrons in the bulk (i.e., slow electron transport), or trapping of electrons or holes at surface states.

4. **Impedence of a photoelectrode**. Of the techniques discussed in this chapter, impedance measurements are arguably the most complicated measurements to perform and interpret. The donor density, $\mathrm{N_D}$, in a semiconductor film can be determined by measuring the space charge capacitance, $\mathrm{C_{SC}}$, as a function of the applied potential ϕ_A:

$$\frac{1}{C_{SC}^2} = \frac{2}{\epsilon_0 \epsilon_r e N_D A^2}\Big(\phi_A - \phi_{FB} - \frac{kT}{e}\Big) \tag{8}$$

A plot of the slope of $1/C_{SC}^2$ vs. ϕ_A should give a straight line with a slope that is proportional to $1/N_D$, while the intercept with the potential axis gives the flatband potential, ϕ_{FB}. The challenge is to distinguish $\mathrm{C_{SC}}$ from other contributions of the photoelectrochemical cell. These can be either capacitive or resistive in nature. Other capacitive elements are the Helmholtz capacitance and surface state capacitances. Examples of resistive elements are the semiconductor bulk, the electrolyte, contacts, and charge transfer resistances. The contributions of all these elements can be modeled by a so-called equivalent circuit (Figure 7a). Extracting the space charge capacitance from the overall response of such a complicated circuit can be difficult. Fortunately, many contributions can be ignored, and in the most simple case this leads to an RC series circuit whose overall impedance is given by

$$Z = R - j\frac{1}{\omega C_{SC}} \tag{9}$$

where, $j = \sqrt{-1}$ and ω represent the angular frequency at which the impedance is measured. It is equal to $2\pi f$, with f the frequency in Hz. For this simple RC series circuit (Figure 7b), it can be easily seen that the real part of the impedance, $\mathrm{Z_{Re}}$, corresponds to the resistance R, and the imaginary part, $\mathrm{Z_{Im}}$, is equal to $-1/\omega C_{SC}$. This means that the space charge capacitance can be directly determined from the imaginary part of the impedance. Thus, by measuring the imaginary part of the impedance as a function of the applied potential, one can obtain a Mott–Schottky curve in which $1/C_{SC}^2$ is plotted against ϕ_A. In figure 7c it can be seen the equivalence circuit that usually encountered in practice for photoelectrodes.

2.2.4 Photoelectrochemical reactor configurations

A number of reactor configurations for PEC devices have been explored for maximum light-absorption per unit volume of the reactor. Main focus lies on achieving a good separation of products to avoid the undesired back reactions, and to achieve a sufficient current-density (about 10–15 mA/cm2). The main configurations can be described as follows: [10]

1. **Single-photoelectrode based PEC reactors**. One of the two electrodes is made up of the photoactive material for carrying out the photoelectrochemical half-cell reaction, while the other electrode is a metal-based material. The photoactive electrode is illuminated with light of suitable energy that results in the generation of charge-carriers in the electrode bulk. Figure 8a shows a single photoelectrode PEC reactor based on the n-type photoanode. One of the main disadvantages of such reactors is the unfavorable semiconductor band-edge positions and the requirement of a large additional bias. Efforts should be made to improve the

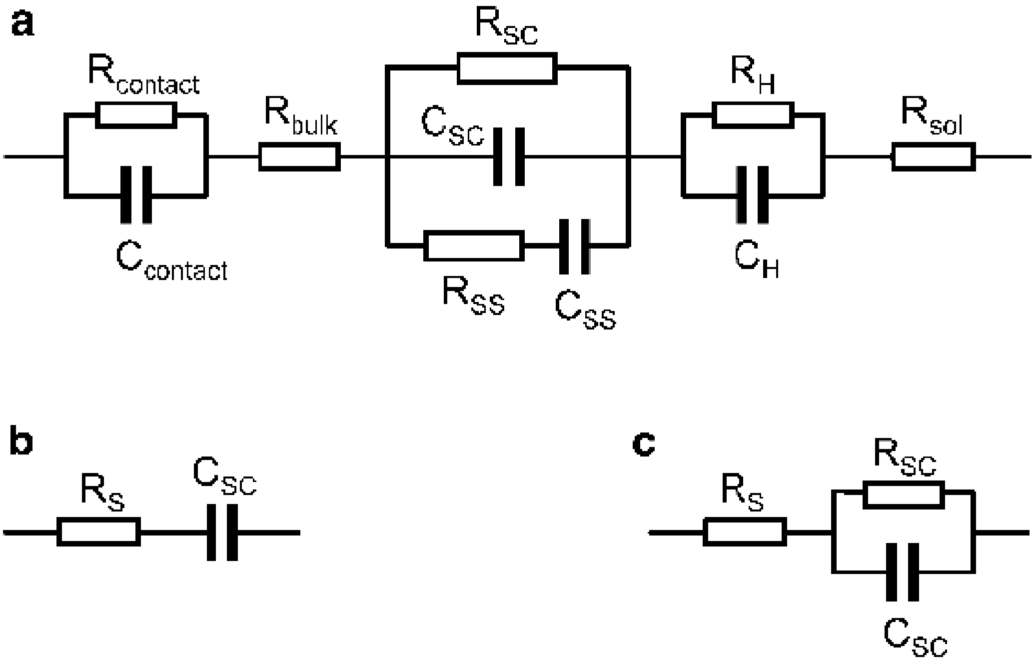

Figure 7: Equivalent circuit diagrams for photoelectrochemical cells. (a) Extensive circuit that contains contributions from the semiconductor/back contact interface ($\mathrm{R_{contact}}$, $\mathrm{C_{contact}}$), the semiconductor bulk resistance ($\mathrm{R_{bulk}}$), the space charge region ($\mathrm{R_{SC}}$, $\mathrm{C_{SC}}$), surface states ($\mathrm{R_{SS}}$, $\mathrm{C_{SS}}$), the Helmholtz layer ($\mathrm{R_H}$, $\mathrm{C_H}$), and the electrolyte resistance ($\mathrm{R_{sol}}$). (b) Simplest circuit possible in which only the space charge capacitance and an overall series resistance is present. (c) Circuit that is often encountered in practice for photoelectrodes.[3]

electronic-structures of the materials, while addressing the instability in aqueous media so that the band-energetics are well suited for water-redox reactions.[]

2. **Dual-photoelectrodes based PEC reactors**. In such a tandem configuration, both electrodes are photoactive, wherein an n-type semiconductor is used as a photo-anode and a p-type semiconductor as a photo-cathode. Such a system generates a higher photovoltage than a single-electrode system for the overall water-splitting. Photovoltages generated by the two photoelectrodes are added, and hence overcome the thermodynamic barrier for water-splitting without the necessity of any additional biasing. In such systems, the valence band-edge of the photocathode should be below the conduction band-edge of the photoanode for the external migration of electrons. Several studies have been conducted on different arrangements of the two photoelectrodes and the influence of the overall configuration on reactor efficiency. The configuration that has proven to be more effective in the overall water-splitting is the one where the two electrodes are arranged parallel to each other and separated by a certain distance so that both are illuminated by sunlight, and also any back-reaction between the products is prevented (Figure 8b).

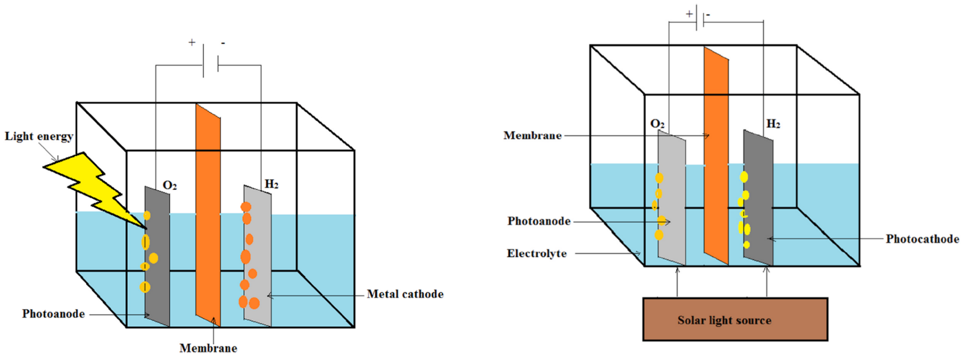

Figure 8: PEC reactors configuration: (a) PEC device with one photo-absorbing semiconductor electrode (photoanode). (b) PEC reactors based on the dual-photoelectrodes system (parallel arrangement of photoelectrodes).[10]

2.3 CONDOR project

All that has been described so far are the basic elements for the description of the CONDOR research project (EU-funded for a period of 4 years).

The CONDOR (COmbined suN-Driven Oxidation and CO_2 Reduction for renewable energy storage) project is aimed at the production of fuels by using carbon dioxide (CO_2) as feedstock and sunlight as the sole energy source. The project proposes a photosynthetic device made of two compartments (Figure 9):

(a) a photoelectrochemical cell (PEC) that splits water and CO_2 and generates oxygen and syngas (a mixture of H_2 and CO);

(b) a (photo)reactor that converts syngas into methanol and dimethylether (DME), via bi-functional heterogeneous catalysts.

The final target is a full photosynthetic device with 8% solar-to-syngas and 6% solar-to-DME efficiencies with three-months continuous outdoor operation. The process will contribute to the decarbonization of the economy, curtailing our dependence on fossil fuels as sources of carbon. The overall system will have a low-environmental impact, thanks to the use of earth abundant elements in catalyst/electrodes and of low energy/low temperature routes for their production.[11]

My contribution to this research project concerns the realization and characterization of the photocatalyst using abundant and low cost elements that allows to achieve a sufficient current-density (about 10–15 mA/cm2) and stability over time.

In the following chapters will be presented and described the elements and alloys that will be used for the realization of the photoelectrode; how they have been synthesized to produce the p-n junction and a description of it. Finally, it will be described the methods used to characterize the various photoelectrodes, the obtained current-density values and the stability achieved.

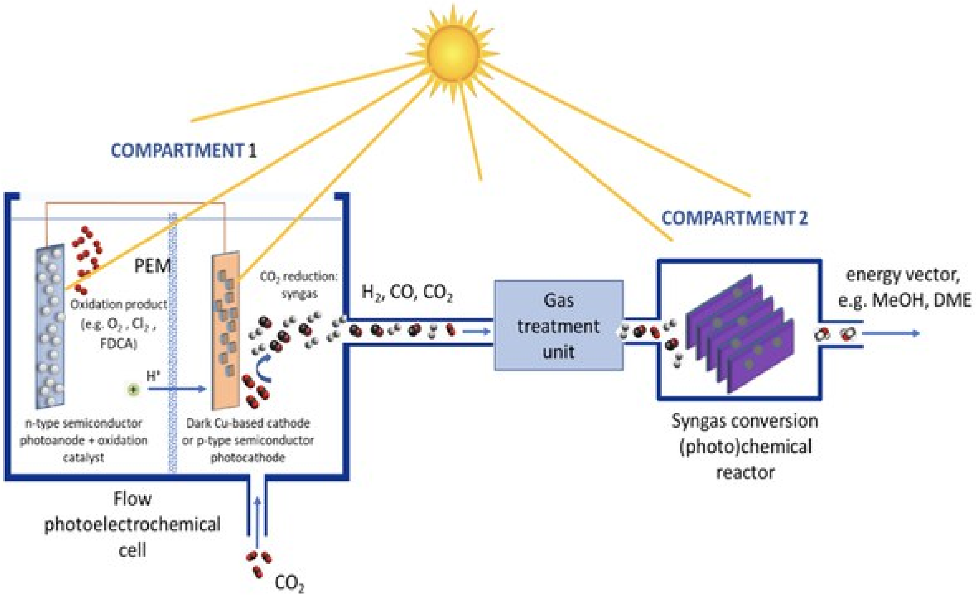

Figure 9: Scheme of operation of the solar conversion device of CO_2 into fuels. At compartment 1 the photoelectrodes absorbs the high-energy portion of the solar spectrum to begin the conversion process: electrons extracted from electronic donors (water or biomass) are used at the cathode to produce a mixture of CO and hydrogen (syngas) converted to compartment 2 by special catalysts based on silicon and metals. The final product is methanol or dimethylether.[]

3. Material properties

In this chapter, the characteristics of the multilayer electrodes and alloys used to create them will be presented.

3.1 CIGS-based electrode

For direct PEC water splitting, the minimum theoretical electrical potential that is required to split water under standard conditions is 1.23 V. Owing to several factors such as cell resistance, irreversible processes etc., the actual voltage required to achieve water electrolysis is typically in the range of 1.8–2.0 V. Metal oxides have been widely studied as photoelectrodes in PEC water splitting due to their suitable band edge position and good chemical stability. For example, doped TiO_2, Fe_2O_3, ZnO, $BiVO_4$ and WO_3 are generally considered as promising photoanode materials, while Cu_2O, NiOx and Co_3O_4 are widely studied as photocathode materials.[12]

However, the band gap of most metal oxides is relatively too large to absorb sufficient sunlight, which limits the efficient absorption of visible light. As compared with metal oxides, CIGS has a tunable bandgap in the range of 1.0-2.4 eV, and its excellent light harvesting characteristics (i.e. absorption coefficients of $10^5 cm^{-1}$) allow a high light harvesting efficiency of close to unity. Solar cells using a CIGS absorber have achieved efficiency approaching 22.6%, making the p-type CIGS semiconductor film a promising photocathode for PEC water splitting.[12] After light absorption, the electrons and holes generated in CIGS are quickly separated; holes would flow to the counter electrode and the external circuit, where oxygen (O_2) is produced. While electrons flow from CIGS to the semiconductor/electrolyte interface, where H^+ ions in the electrolyte are reduced to H_2.

FTO (Fluorine-dopen Tin Oxide) is used as a backcontact for the electrical characterization. It is a transparent conductor and oxide that can be used both in air and in solution as a backcontact. We will try as a backcontact in solution also the Molybdenum (Mo).

It is necessary to introduce a protective layer, which limits the corrosion of the electrode in the cell. Furthermore, it must promote the PEC water splitting efficiency by accelerating the H_2 generation process. The TiO_2 has been used as both protective overlayer and a catalyst to improve the hydrogen evolution kinetics of CIGS photocathodes.

3.1.1 CIGS

Copper indium gallium (di)selenide (CIGS) is a I-III-VI_2 semiconductor material composed of copper (Cu), indium (In), gallium (Ga) and selenium (Se). The material is a solid solution of copper indium selenide (CIS) and copper gallium selenide. It has a chemical formula of $CuIn_xGa_{(1-x)}Se_2$ where x vary from 0 (pure copper indium selenide) to 1 (pure copper gallium selenide). The idea of the CIGS is to mix this two compounds in order to conserve the good performance in optoelectronics devices of CIS and, at the same time, obtain a tunable energy gap mixing it with $CuGaSe_2$.

From x-ray analyzes, it has been confirmed that CIGS conserve the chalcopyrite structure of the CIS, thetraedrally bonded. Upon heating it transforms to the zincblende form and the transition temperature decreases from 1045 °C for x=0 to 805 °C for x=1.[13] Figure 10a show the tetrahedrally bonded semiconductor, with the chalcopyrite crystal structure.

The dependence of the band gap relative to the percentage of In in the material is show in Figure 10b. In many semiconducting systems, the band gap in semiconductors is approximately a linear function of the lattice parameter. Therefore, if the lattice parameter of a semiconducting system follows Vegard's law, one can also write a linear relationship between the band gap and composition:

$$E_g^{CIGS}(x) = E_g^{CIS} + [E_g^{CGS} - E_g^{CIS} - b(1-x)]x \tag{10}$$

where E_g^{CIS} and E_g^{CGS} are the band gaps of $CuInSe_2$ and $CuGaSe_2$. From the fit of Figure 10b, we can get a value for b = 0.175eV, value that is called Bowing parameter, term that take into account the disorder effect in the alloy, caused by the different electronegativities of In and Ga[13]. Substituting b, E_g^{CIS} (1.620 eV) and E_g^{CGS} (0,955 eV)[13], the equation 10 can be rewritten as:

$$E_g^{CIGS}(x) = (1.620 - 0.840x + 0.175x^2) \tag{11}$$

3.1.2 Substrate as back-contact

We use two different substrate as back-contact: Fluorine doped tin oxide (FTO) and Molybdenum (Mo).

Fluorine doped tin oxide (FTO) is a transparent conducting oxide which is widely used in different applications ranging from sensors, digital displays, smart window coatings, catalysts supports, and electrode substrates for various electrochemical applications. FTO has a tetragonal structure with fluorine incorporated as a donor with a direct bandgap of 3.6 eV and an optical bandgap of > 4 eV.[14] It is considered a direct bandgap material, the electron transition occurs by conserving momentum and no energy is dissipated by phonon or photon emissions. It is generally considered that fluorine

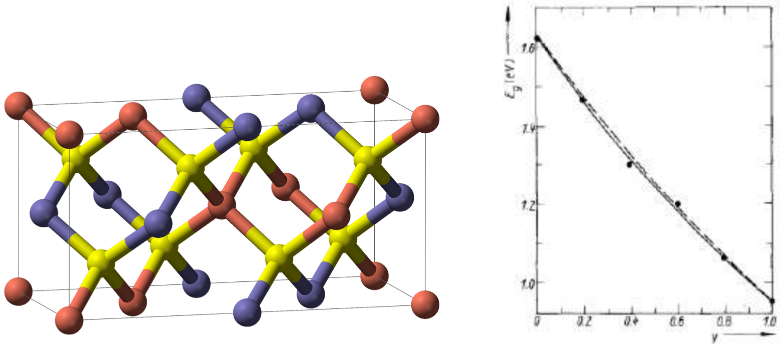

Figure 10: Characteristic of the CIGS: (a) chaclopyrite structure of the material: Red = Cu, yellow = Se, blue = In.[13]

occupies the oxygen site as a singly charged donor because of its similar atomic radius to that of O^{2-} and similar bonding energies of Sn-O and Sn-F (Figure 11. Fluorine doping of SnO_2 results in low electrical resistivity of FTO $(4 \cdot 10^{-4} \Omega cm)$. An increased level of F doping increases the resistivity which could be due to compensation of donors. Oxygen vacancies (V_O) participate in the charge transfer reaction of SnO_2 and the conductivity varies inversely with p_{O_2}.[14]

Molybdenum (Mo) is the most important material used as a back-ohmic contact in copper indium gallium diselenide (CIGS) thin film solar cells. The metallic back-contact, Mo, serves as substrate on which the absorber layer i.e., CIGS is deposited. Mo is more favorable as a back-contact layer in CIGS thin film solar cells because its diffusion into the absorber starts above 600 °C and, in addition, it offer a resistance to alloying with copper and indium.[15]

3.1.2 Protective overlayer

TiO_2 layer on top of the electrodes may be used to protect them during photocatalytic H_2 evolution. Although TiO_2 is a semiconductor, it behaves like a metallic conductor in photocathodic H_2 evolution conditions. This behavior is due to the alignment of the TiO_2 conduction band with respect to the hydrogen evolution potential, which allows it to conduct electrons while simultaneously protecting from surface passivation.[16] TiO_2 has attracted immense interest because it is low-cost, abundant, and photoresponsive. The lack of stability is a challenge for most heterogeneous catalysts. During operations, the agglomeration of particles may block the active sites of the catalyst, which is believed to contribute to its instability. Recently, titanium oxide (TiO_2) was introduced as an alternative support material for catalyst due to the effect of its high surface area stabilizing the catalysts in its mesoporous structure.[17] The aforementioned properties make

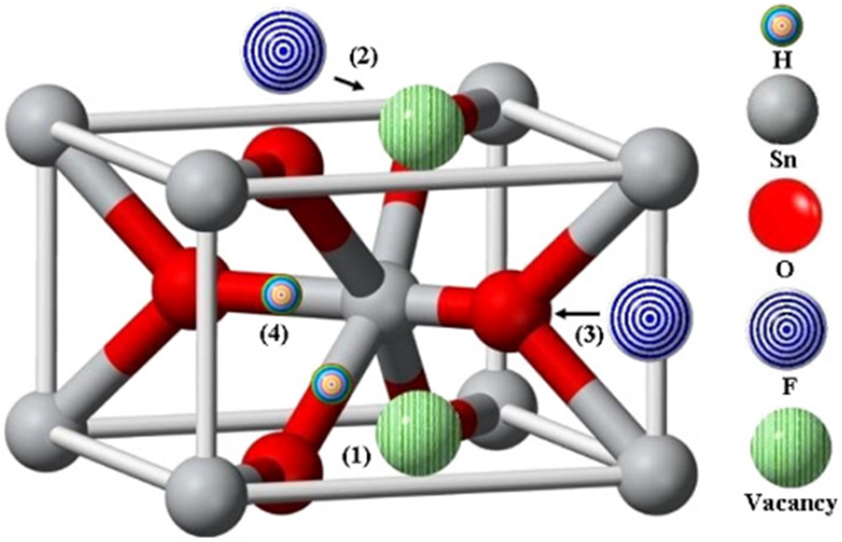

Figure 11: Fluorine doped tin oxide (FTO). Reference: Work function of fluorine doped tin oxide.[14]

TiO_2 supported catalysts show a high potential in photocatalyst-related applications, electrodes for solar cells, synthesis of fine chemicals, and others.

3.2 CIGS/CdS/TiO_2

However, although CIGS has high absorption efficiency, its charge transfer efficiency is not satisfactory, especially at the electrode/electrolyte interface.

CIGS is a p-type semiconductor with strong light absorption characteristics. If bare CIGS was used as a PEC photocathode, it would not perform well due to the lack of favorable energetics alignment with the electrolyte. Thus, this would result in inefficient separation of photogenerated charge carriers. Whereas, the deposition of a thin layer of CdS on top of CIGS could form a solid-state p–n junction and lead to more efficient charge separation.

The deposition of the n-type CdS layer over the p-type CIGS layer forms a space charge (depletion) region at the solid-solid interface (p-n junction), which results in better separation of the charge carriers. Moreover, the potential difference in the valence band of the CIGS and CdS layer further enhances the charge separation. Strong electric fields form at the CIGS/CdS interface, which drives the electron transport from CIGS to CdS, and the slightly positive band-offset at this interface further minimizes the interfacial recombination.

3.2 CIGS/CdS/AZO/TiO_2

As compared with CdS, AZO has a wider bandgap (3.37 eV) which is more favorable for driving the water reduction reaction while maintaining suitable valence and conduction band positions. Thus, by depositing another thin layer of AZO on top of CdS, it would form a better alignment between the AZO/CdS/CIGS interfaces, which would help to drive the charge transport further and minimize charge recombination. Moreover, the band alignment at the CdS/AZO interface occurs in such a way that the position of the conduction band minimum gradually decreases from CdS to AZO, enhancing the transport of the photogenerated electrons from CIGS to AZO. On the other hand, because AZO has a direct bandgap, AZO is favorable for driving the water reduction reaction while maintaining suitable conduction and valance band positions. Moreover, AZO promotes the flow of electrons from CIGS/CdS towards the electrode-electrolyte interface and the flow of holes in the opposite direction towards the back-contact.

Aluminum doped zinc oxide (AZO) films have been extensively used for thin film solar cells as transparent conductive oxide, liquid crystal displays (LCD) and large area flat panel displays.

ZnO semiconductor is an attractive material in the research community for photoelectrochemical (PEC) solar cells due to its wide, direct band gap (E_g = 3.37 eV at 300 K), and large exciton binding energy (60 MeV), large non-linear optical coefficients, high thermal conductivity and excellent electrochemical stability.[18] However, the large photonic energy requirement of ZnO semiconductor only limits its light absorption with in a small fraction of the solar spectrum. Thin film properties such as crystal structures, surface structures, band gap and optical absorption and electrical/optical conductivity of ZnO has been improved by introducing dopants in to ZnO lattice. The transition metals (Al, Cu, Ni, Ag, Co) doped ZnO show better properties which are suitable for photovoltaic (PV) application, as these metals have ionic radius nearly similar to ZnO. $Al3^+$ has been the most used dopant element due to its small ionic radius and low material cost (Figure 12). The substitution of $Zn2^+$ ions with $Al3^+$ in ZnO lattice improves the electrical conductivity through the increase of charge carriers.[18]

Therefore, in the CIGS/CdS/AZO/TiO_2 photoelectrode, the CdS layer enhances the charge carrier separation. Furthermore, the presence of the AZO layer promotes charge migration to the electrode-electrolyte interface at which water reduction occurs. Finally, a protective overlayer of TiO_2 is used to prevent the corrosion of in the electrolyte and as HER catalyst to promote the surface reaction.

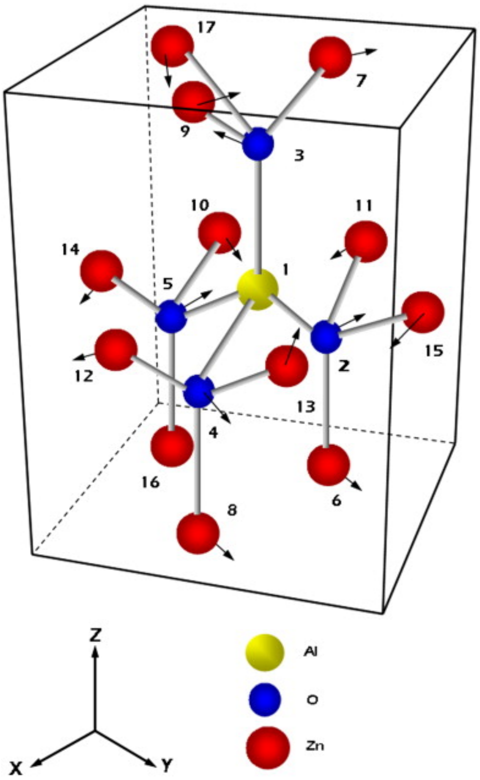

Figure 12: Schematic diagram showing Al impurity within the wurtzite-type structure of the ZnO crystal. The pointers indicate the direction of absolute atomic movements due to the defect-produced perturbation. Reference: Al-doped ZnO: Electronic, electrical and structural properties.[18]

4. Experimental apparatus

In this chapter, I will describe the main experimental techniques and related setups used to synthesize the materials and to perform measurements.
In particular, I will focus on the description of the RF magnetron sputtering technique used to deposit thin layers of material to form the multilayer electrodes and the PEC cell used to an electrochemical characterization. Finally, a description of the XRD and SEM for a structural and morphological characterization.

4.1 Radio frequency magnetron sputtering

Radio frequency magnetron sputtering, also called RF magnetron sputtering is a process that is used to make thin film, especially when using materials that are non-conductive. In this process, a thin film is grown on a substrate that is placed in a vacuum chamber. Powerful magnets are used to ionize the target material and encourage it to settle on the substrate in the form of a thin film.

4.1.1 Sputtering deposition

Sputtering is a phenomenon in which energetic particles of plasma or gas hit the surface of a solid and microscopic particles are separated from it. Due to the collision of high-energy ions with the target material atoms, momentum transfer occurs between them. These ions, called incident ions, cause a series of collision cascades on the surface of the target. Sometimes these successive collisions cause the ions to travel long distances and lose their energy. If the ion energy at the time of reaching the target surface is greater than the bonding energy between the atoms of the target material, the collided atom separates from the target material. This phenomenon is called sputtering. One of the applications of sputtering phenomenon is the deposition. Deposition using sputtering is a method of creating thin films of a few nanometers to a few micrometers on the desired substrate. This type of deposition is a physical vacuum deposition method (Physical Vapor Deposition), a set of deposition methods in which the material enters the vapor phase from the dense state and returns to the dense phase as a thin film.

Approximately one percent of the ions that hit the surface of the target material have a ballistic impact and return to the substrate, causing Resputtering. The average number of atoms separated from the surface of the target material by the collision of each ion is called the Sputter Yield.[19] The sputter yield depends on many factors, such as:

- the angle at which the ions strike the surface of the target material
- the amount of ion energy during the collision
- the weight of the ions
- the weight of the atoms of the target material
- the binding energy between the atoms of the target material
- if the structure of the target material is crystalline, the orientation of the crystal axis relative to the surface is also an important factor in the sputtering yield.

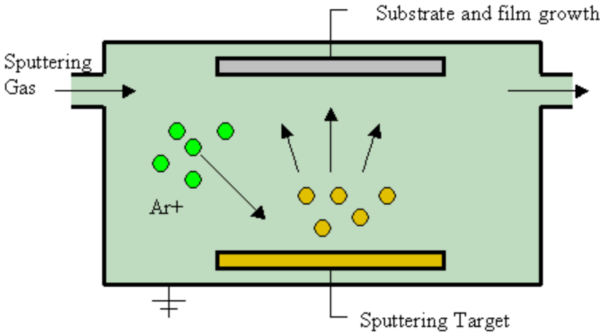

Figure 13: A schematic of sputter deposition.

4.1.2 DC sputtering

DC Sputtering is the most basic type of sputtering for PVD metal deposition and electrically conductive target coating materials. Two major advantages of DC as a power source for this process is that it is easy to control and is a low cost option. The basic configuration of a DC Sputtering coating system is show in Figure 14a. It consist in the target material to be used as a coating placed in a vacuum chamber parallel to the substrate to be coated. The vacuum chamber is evacuated to a base pressure removing H_2O, Air, H_2, Ar and then backfilled with a high purity inert process gas, usually Argon due to its relative mass and ability to convey kinetic energy upon impact during high energy molecular collisions in the plasma that creates the gas ions that are the primary driving force of sputter thin film deposition. Typical sputter pressures range from 10^{-3}-10^{-2} mbar.[120]

As the voltage is increased, the electrically neutral argon gas atoms are first ionized as a result of the forceful collision of these gas atoms onto the surface of the negatively charged target which eject atoms off into the plasma, consisting of roughly half gas ions and half electrons that emits the visible plasma glow (Figure 14b). The ionized argon gas atoms are then driven to the substrate which is the anode or positive charged bias attracting ionized gas ions, electrons and the vaporized target coating atoms which condense and form a thin film coating on the substrate to be coated. DC Magnetron sputtering uses magnets behind the negative cathode to trap electrons over the negatively charged target material so they are not free to bombard the substrate, allowing for faster deposition rates. The deposition rate depends on the pressure inside the vacuum chamber ad the current. If the pressure is low the electron mean-free path between collisions is large and electrons collected by the anode are replaced by ion-impact-induced cathode secondary emission. Therefore, ionization efficiencies are low. By increasing the pressure, the electron mean-free path decreases and more ions are generated. But if the pressure is too high, the sputter atoms undergo increased collisional scattering and are not efficiently deposited.

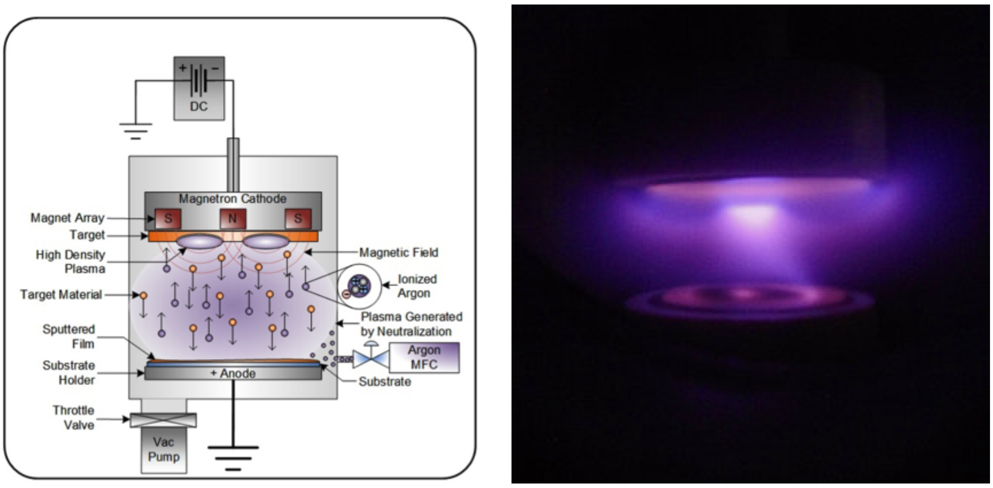

Figure 14: (a) Diagram of the DC Sputtering Process; (b) Argon glow discharge plasma generated in sputtering processes.

4.1.3 Radio-frequency magnetron sputtering

RF or Radio Frequency Sputtering is the technique involved in alternating the electrical potential of the current in the vacuum environment at radio frequencies to avoid a charge building up on certain types of sputtering target materials, which over time can create quality control issues on the thin films and can even lead to the complete cessation of the sputtering of atoms terminating the process. DC Sputtering is limited when it comes to dielectric target materials, coatings which are non-conducting insulating materials that can take on a polarized charge. By alternating the electrical potential with RF Sputtering, the surface of the target material can be “cleaned” of a charge buildup with each cycle. On the positive cycle electrons are attracted to the target material or cathode giving it a negative bias. On the negative portion of the cycle, ion bombardment of the target to be sputtered continues. RF Sputtering can sustain a plasma throughout the chamber at a lower pressure. The result is fewer ionized gas collisions equaling more efficient line-of-site deposition of the coating material.

However, as a result of the AC modulation of the power at radio frequencies, the material to be coated with RF Sputtering does not acquire as great a charge buildup due to it being discharged each half cycle and becoming insulated – which over time can eventually lead to a cessation of the thin film deposition. With RF Magnetron Sputtering the magnetic field forms a boundary “tunnel” which traps electrons near the surface of the target improving the efficiency of gas ion formation and constraining the discharge of the plasma. In this way, RF Magnetron Sputtering allows for higher current at lower gas pressure that achieves an even higher deposition rate.[20]

4.1.4 Experimental setup

Figure 15: RF magnetron sputtering setup. In this figures are show: (a) The chamber, argon cylinder, LabView software, Kenosistec module, turbomolecular and scroll pump, pressure sensors and RF machine; (b) The chamber and the cathodes below it; (c) The interior of the chamber

In Figure 15a the RF magnetron sputtering system that I used for preparing the samples is reported. The system is composed by a cylindrical ultra-high vacuum chamber at the bottom of which an turbomolecular pump (Edward EXT 250) together with an scroll pump (Agilent IDP-10) is connected. This pumping setup allows to reach 10^{-7} mbar in about a day.

Pressure is monitored by two different sensors: a Pfeiffer Compact Full Range Gauge PKR 251 is used during the evacuation and venting procedure, exploiting its wide working pressure range, from 10^{2} to 10^{-9} mbar, while a more accurate MKS absolute Baratron is used during the sputtering evaporation (working range 10^{-1}-10^{-4} mbar). In figure 16 we can see the pfeiffer pressure sensor. Near it, there is the mass flow and pressure controller, that has the aim to control the flux of argon entering in the sputtering chamber. The turbomolecular pump controller for the on, off, and stand-by status. The radio-frequency is controlled by a Kenosistec BDS HF. Argon gas is introduced using an MKS GE50A flowmeter.

Pressure, gas flow and temperature are monitored and controlled by a software written in LabVIEW (Figure 18). In addition, I integrated the LabView program allowing the control of the RF machine by remote. I show the details in the appendix A.

The target material is attached to the KENOS-2 cathode, equipped with a manual shutter. Substrates are attached to the sample holder in front of the target (Figure 15b, 15c).

The sputtering procedure is the following:

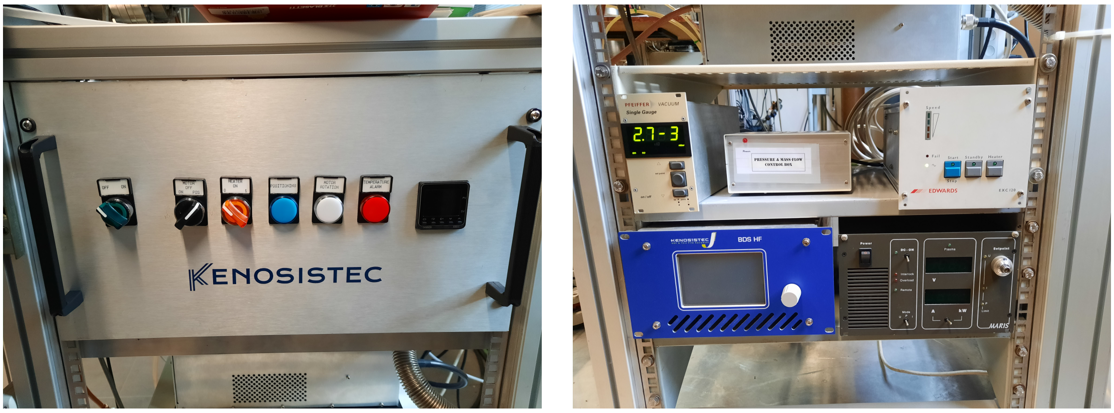

Figure 16: Kenosistec module. (a) Temperature and rotate plate controller; (b) pressure, mass flow, pump and RF controller.

1. The chamber is evacuated initially with the scroll pump and then using the turbomolecular pump in order to get a pressure up to 10^{-7} mbar;
2. Possibly, if the deposition is not done at room temperature, we set a default temperature using a temperature controller in the Kenosistec module. The set temperature will not be exactly equal to that obtained due to temperature sensor distance from material substrate, so we will use a calibration curve to set the desired temperature (Figure 17). Set T_{final} the real temperature felt by the material and T_{set} the set temperature, the calibration curve is:
$$T_{final} = 0.7538T_{set} + 40.071 \tag{12}$$
3. The rotation of the plate is turned on, from the Kenosistec module, in order to obtain a more homogeneous deposition;
4. We set the Argon flux using the LabView software, generally we set the flux at 20 sccm flux;
5. The pressure is reduced to $3{\cdot}10^{-2}$ mbar (putting the turbomolecular pump on stand-by) and increasing the power of radio-frequency we will see the ignite the glow discharge;
6. The turbomolecular pump is restarted and the pressure is stabilized and maintained at $8{\cdot}10^{-3}$ mbar;
7. Finally, the RF power is increased to the desired value.

The deposition will have a duration depending on the thickness that you want to obtain, it will depend mainly on the deposition rate of the target.

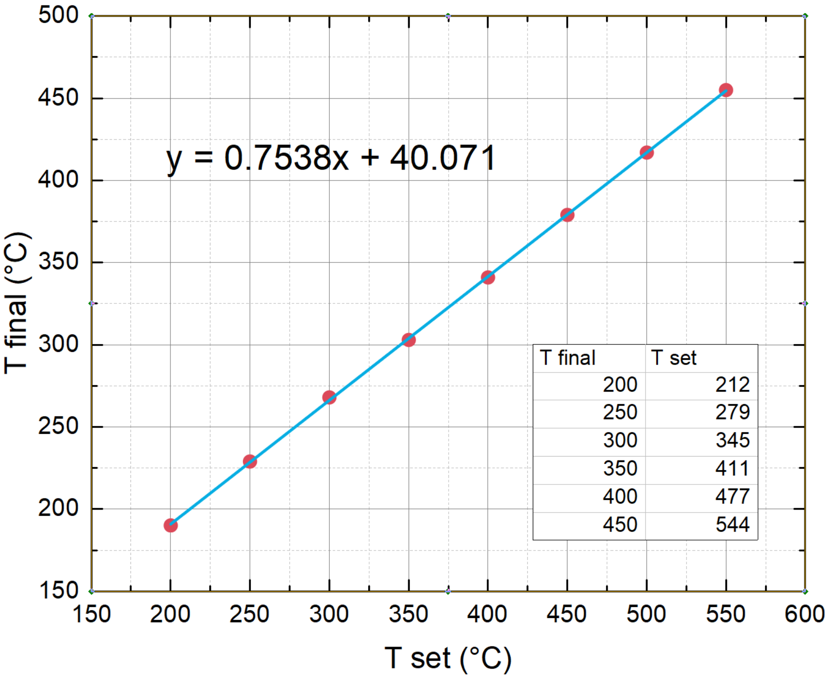

T final	T set
200	212
250	279
300	345
350	411
400	477
450	544

Figure 17: Calibration curve for the temperature: on the y axis the real temperature felt by the substrate, on the x axis the temperature set to the controller.

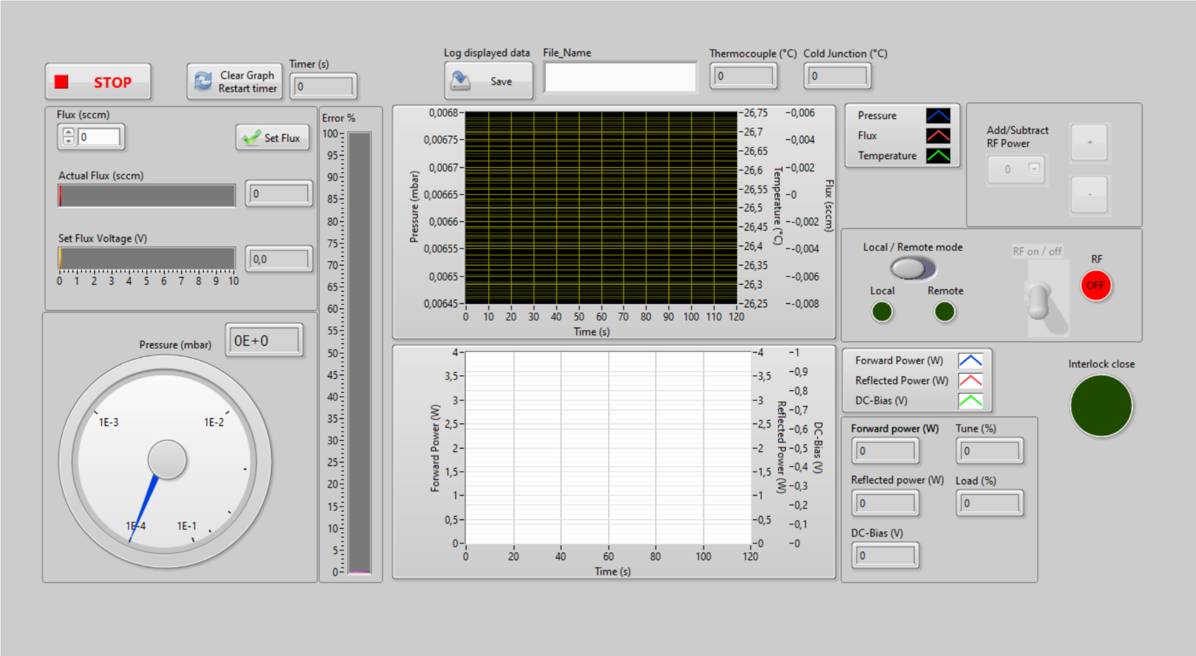

Timer (s): 0

File_Name:

Thermocouple (°C): 0

Cold Junction (°C): 0

Flux (sccm): 0

Actual Flux (sccm): 0

Set Flux Voltage (V): 0,0

Pressure (mbar): 0E+0

Forward power (W): 0

Tune (%): 0

Reflected power (W): 0

Load (%): 0

DC-Bias (V): 0

Figure 18: LabView software. It allow us to control the argon flux and the radio-frequency by remote. There are some indicators and graphs that show us the temperature, pressure inside the chamber, argon flux and the power selected.

4.2 PEC device

In this work we will study only the half reaction for the photocathode (Figure 19). The idea is to separate the study of both cathode and anode, studying the half reaction. Once efficient materials for the two half reactions are found, it should in principle be possible to combine them into a device for the overall reaction.

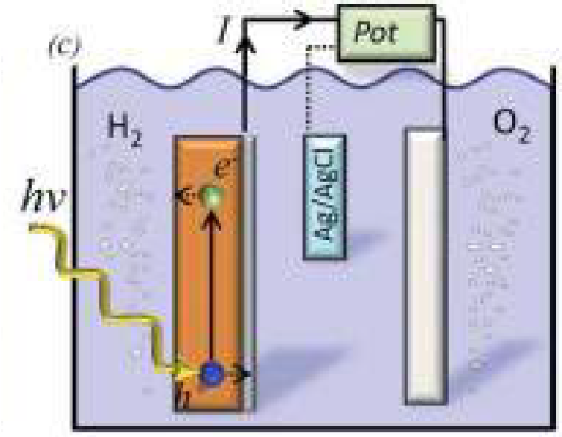

Figure 19: Architecture of a PEC cell with three electrodes, to test the performance of half cells.

In an electrochemical cell we need a reference electrode, a counter electrode and a working electrode. The working electrode (WE) is our electrode. The reference electrode (RE) was needed to mantain the solution in a certain potential, and was done with an electrode with an inner solution of Ag/AgCl. The counter electrode (CE) is the electrode at which we applied the potential. Finally, the cell was keep at ground with a fourth electrode.

Our overall device (Figure 20) is compound by:

- The PEC cell setup
- The electrolyte
- LED source
- The potentiostat
- The Frequency Response Analyzer (FRA)
- NOVA software

Below we analyze in detail the various elements:

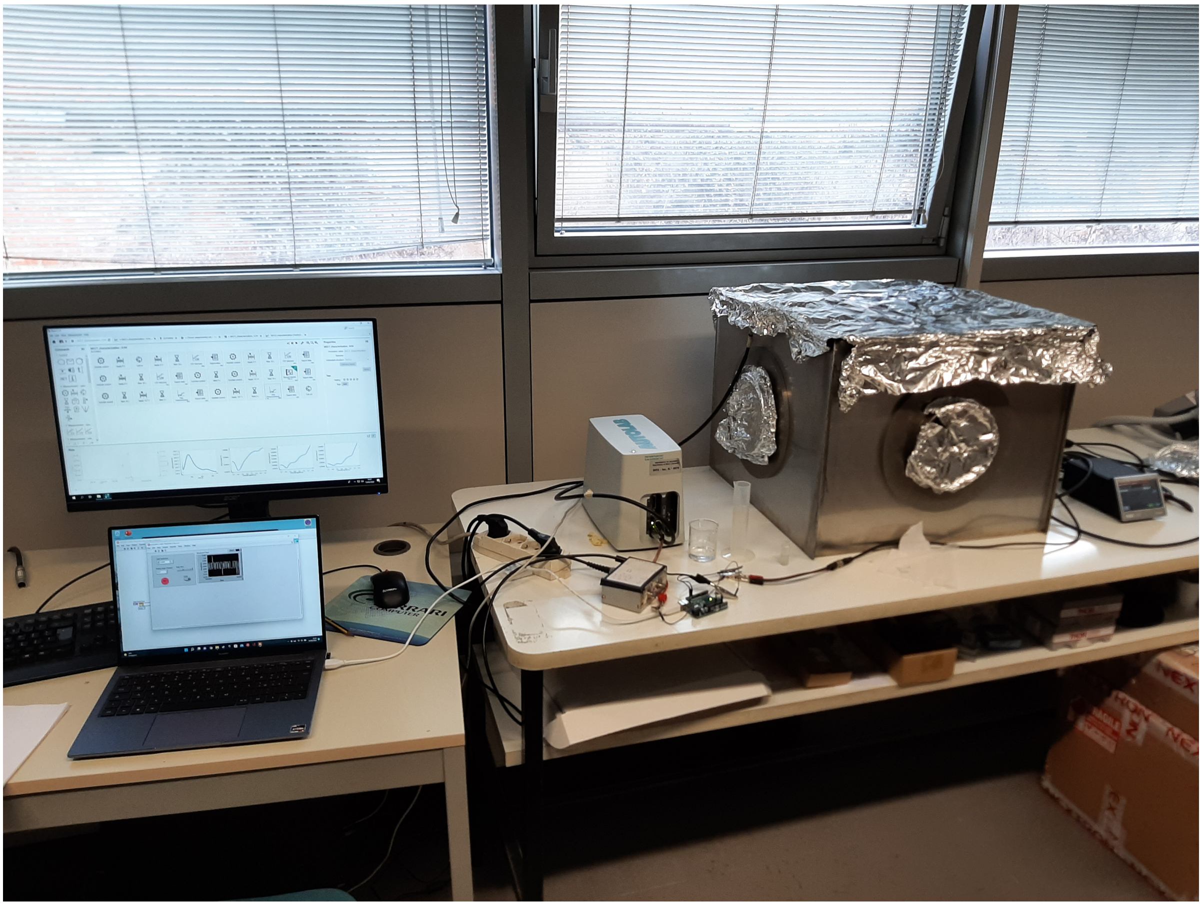

Figure 20: Setup for photoelectrochemical measurements. From left to right: NOVA software, potentiostat, the cell and the lamp controller.

4.2.1 PEC cell setup

The cell used is shown in the Figure 21. It is composed of a hollow plastic material inside it to insert the electrolyte solution. On one side it has a quartz window through which the sample is illuminated and on the opposite side the sample holder, consisting of two discs of different diameters, between which the electrode is inserted. Also on this side there is a central hole (about 0,5 cm) necessary to pass the light and an additional hole to let out the contact to be connected to the WE terminal of the potentiostat. Inside the cavity, in addition to the electrolyte solution, the reference electrode (RE) and the counter electrode (CE) are kept in position in contact with the solution thanks to the removable top cover, which has holes for their placement. Since the electrode must be fully immersed in the solution, part of it must be covered, to avoid direct contact between the solution and the back-contact of the electrode (FTO or Mo layer). To do this, an oxidation-resistant silicone membrane with good insulating properties is used. At the center of the membrane there is a hole, of the same diameter of the hole of the cell, necessary not to compromise the functionality of the electrode.

The various components of the cell are held together through screws that ensures the liquid does not escape.

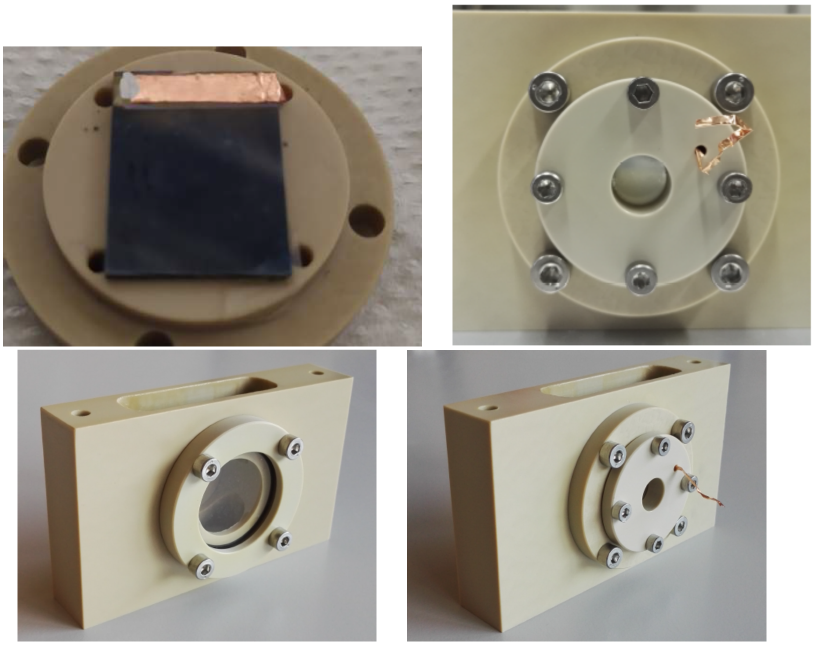

Figure 21: Photoelectrochemical cell. (a) Photoelectrode on the sample holder; (b) copper wire used to connect to the WE terminal of the potentiostat; (c) face with quartz window; (b) face with sample holder.

The cell is mounted inside an aluminum box to isolate external noise. In Figure 22a it is possible to see the box with the cell fixed to it where the reference and counter electrodes are inserted in contact with the electrolyte solution and the potentiostat terminals connected to the various electrodes and on the ground. In figure 22b we observe the LED lamp in front of the cell. The lamp is positioned in such a way as to completely illuminate the quartz window.

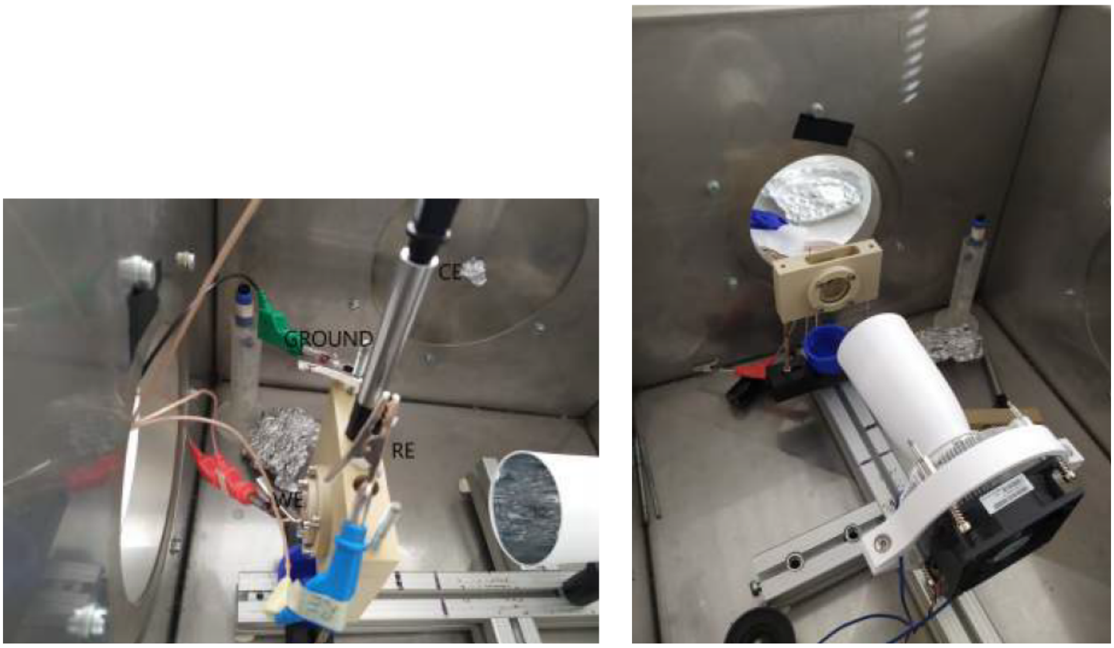

Figure 22: (a) Cell with working electrode, counter electrode, reference electrode and ground. (b) Lamp in front of the cell.

4.2.2 Electrolyte

In an electrochemical cell the electrolyte consists of a solvent in which the active species to be reduced or oxidized are dissolved. In the present case, the solvent and the active species is the same, water. However, since distilled water is poorly conductive, it is necessary to add additional ions so that the current can flow without resistances into the cell. For the experiments a solution consisting of 150 ml of NaH_2PO_4 0.1M and 3 ml of $NaHPo_4$ 0.1 M was used. Obtaining a solution with PH 5.0.

4.2.3 LED source

The used lamp was a sunlight LED COB of seoul semiconductors with dimension of 19x19 and a diameter of surface emission of 14.5 mm. The emitted spectra of the led is shown in figure 23a. In this image, the led spectra is compared with an usual white led spectra and we can see that the led used is more optimized to simulate sunlight spectra. To concentrate the light on our sample a cilinder with a reflective interior was put above the lamp (Figure 22b).

The lamp was controlled with a Thorlabs driver (Figure 23b) that allowed to control the intensity and the modulation. To control the switching on and off of the lamp and to use the lamp in chopped mode during measurements was used the Thorlabs driver by remote (using an Arduino board) and a software in labview that I developed (Figure 23c).

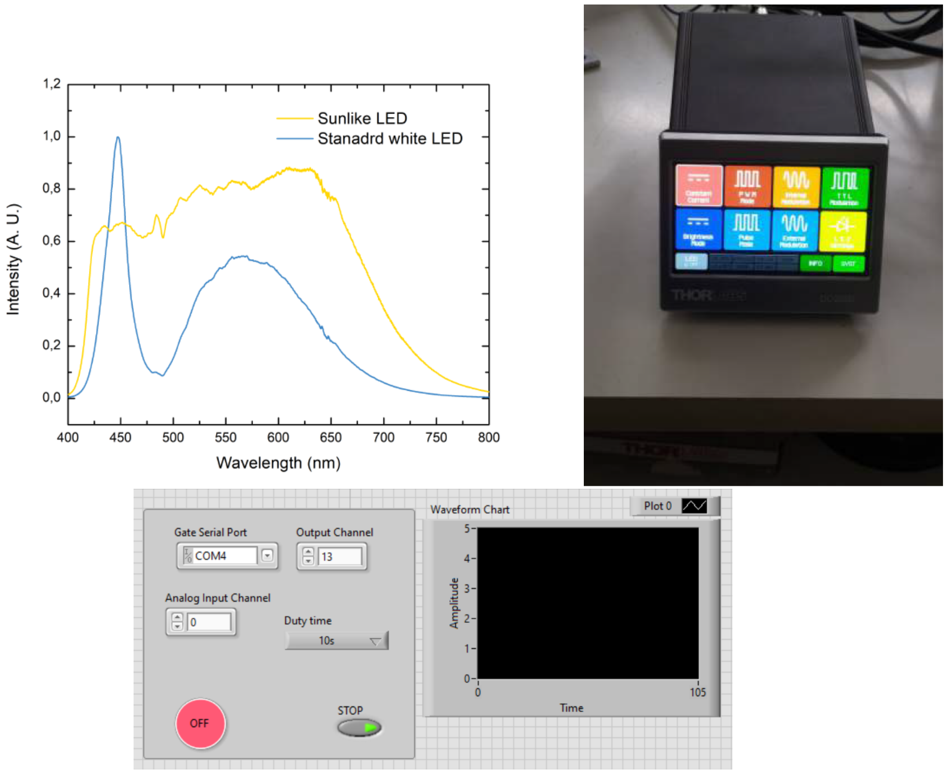

Gate Serial Port: COM4
Output Channel: 13
Analog Input Channel: 0
Duty time: 10s

Figure 23: (a) Comparison between an usual white led (blue) and the sunlike LED used (yellow); (b) Thorlab driver used for controlling the lamp; (c) LabView software used to control the switching on and off of the lamp and set the chopper mode with the possibility to set the duration of the alternation.

4.2.4 Potentiostat

The potentiostat used in this work is a PGSTAT204 from Metrohm Autolab (Figure 24). The function of the potentiostat is simple: it measures the potential difference between the RE and the WE and makes it equal to the desired value, modifying the potential of the CE with respect to the WE. The potential difference is controlled between the WE and the EC. WE is maintained at a pseudo-ground potential (stable potential) by controlling CE polarization. The potential difference between RE and WE is checked for the duration of the measurement, while the potential difference between WE and CE is not measured. The CE only has the function of providing voltage and current necessary to maintain the potential difference between WE and REF to the desired value.

Figure 24: Potentiostat unit: PGSTAT204 from Metrohm Autolab.

4.2.5 Frequency Response Analyzer

The Frequency Response Analyzer (FRA) is an instrument that allows you to measure the real and imaginary part of the impedance of a sample. In this work, the FRA called FRA32M was used and it is integrated into the potentiostat.

Its function is to generate a sine wave of voltage with a certain frequency and a certain amplitude, which is then used to modulate the potential applied to the cell by the potentiostat. If the system responds linearly, the measured current output from the cell is sinusoidal and differs only in amplitude and phase with respect to the input voltage perturbation. The potential and the measured current are sent back to the

FRA through the analog potentiostat inputs and are further processed by the FRA to calculate the impedance. For the system to respond linearly it is necessary that the wave amplitude is small, typically 5-10 mV for photoelectrochemical devices.[] As a result, the current response is also very small and must be isolated from the main signal (DC) of the potentiostat, to which the background electronic noise is inevitably added. To do this a phase sensitive detector (PSD) is used. The PSD multiplies the signal that arrives as input, given by the overlap of sinusoidal signals at different frequencies, by a sinusoidal reference signal generated internally and integrates the result for a whole number of cycles of the reference signal. Mathematically speaking, sine waves with different frequencies are orthogonal, and therefore the integration operation always results in zero, unless the input signal has a frequency equal to that of the reference signal. In this case the PSD returns a DC voltage output proportional to the amplitude of the signal while for any other frequency the output signal is zero. In an FRA there are four PSDs: two for voltage measurements and two for current measurements, from which you can get the real and imaginary part of voltage and current measured and then impedance, dividing the first by the second through a microprocessor.

4.2.6 NOVA software

NOVA is a package designed to control Autolab instruments with a USB interface. We used NOVA software for the following characterizations:

- **Open Circuit Potential (OCP)**. It is the potential established between the working electrode and the environment, with respect to a reference electrode.

- **Linear Sweep voltammetry (LSV)**. It is a voltammetric method where the current at a working electrode is measured while the potential between the working electrode and a reference electrode is swept linearly in time. Oxidation or reduction of species is registered as a peak or trough in the current signal at the potential at which the species begins to be oxidized or reduced.

- **Transient Photocurrent (TPC)**. It is a measurement technique that allows to study the time-dependent extraction of charges generated by photovoltaic effect in semiconductor devices.

- **Electrochemical Impedance Spectroscopy (EIS)**. This measurements allows the characterisation of heterogeneous systems formed by a series array of layers with different electrical/structural properties by using equivalent circuits as models. This technique is used in the case of membrane/electrolyte systems, which allow the characterisation of membranes in “working conditions” (in contact with electrolyte solutions).

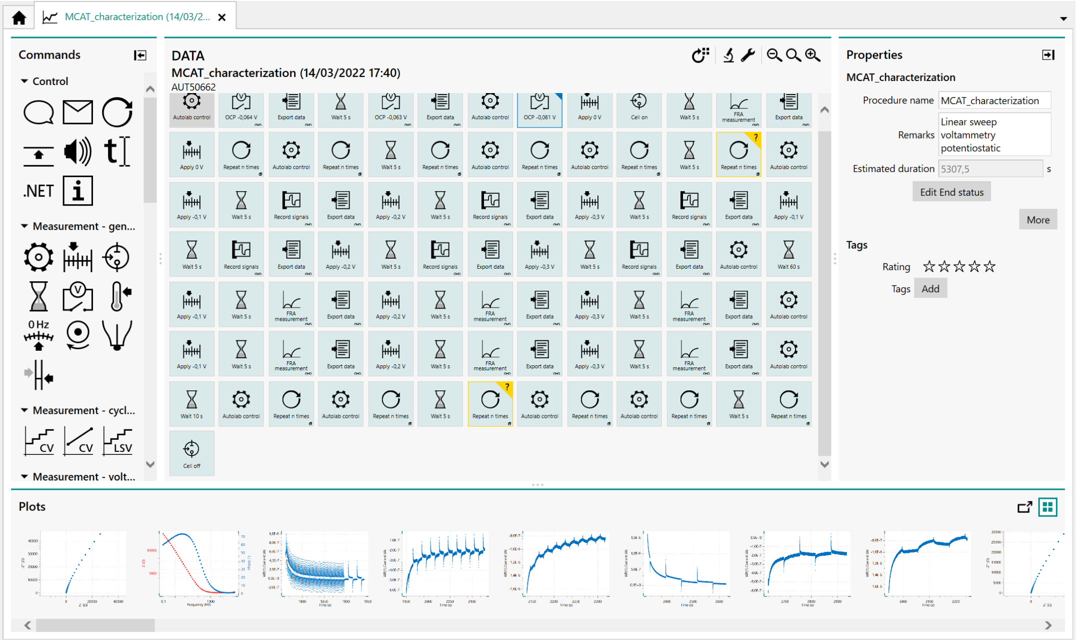

MCAT_characterization (14/03/2022 17:40)
AUT50662

MCAT_characterization
Procedure name: MCAT_characterization
Remarks: Linear sweep voltammetry potentiostatic
Estimated duration: 5307,5 s

Figure 25: Example of procedure within the NOVA software.

In particular, within the software you can create a procedure that allows you to make the measurements sequentially. An example of this procedure is shown in the figure 25.

4.3 Structural and morphological characterization

The samples obtained were analyzed both structurally, using the X-Ray Diffraction (XRD) technique, and morphologically, using a scanning electron microscope (SEM), that also allows the analysis Energy Dispersive X-Ray (EDX) to study their composition.

4.3.1 X-ray diffraction

X-ray diffraction (XRD) is a widely used technique to investigate the crystallinity and structure of solid samples. The crystal X-ray diffraction phenomenon results from a scattering process in which X-rays are scattered by the electrons of atoms present in the sample without changing the wavelength. Since X-rays have wavelengths (between 0.2 and 10 nm) comparable to the interatomic spacing of a crystalline solid, the incident X-ray beam diffracts in specific directions predicted by Bragg's law (Figure 26):

$$2dsin\theta = n\lambda \tag{13}$$

Specifically, the atomic structure of a substance can be deduced by observing the angular position and the relative intensity of the various diffraction peaks obtained by subjecting a material to X-rays. The characteristic parameters of this process, such as the λ wavelength of the incident radiation, the θ angle at which the radiation affects a lattice plane, and the d distance between the interatomic planes, are bound by Bragg's law; it expresses the conditions under which diffraction peaks are observed, that is, when the reflected radiation from the ions composing the lattice interferes constructively or, equivalently, when the difference in optical path between the various incident rays is equal to a whole number of wavelengths.

The resulting diffraction pattern, given by the positions and intensities of the diffraction effects, is a fundamental physical property of the material, providing not only the identification but also the complete description of its structure.

Usually, it refers to a family of lattice planes with the coordinates in the reciprocal space of the vector of the reciprocal lattice perpendicular to the planes. These coordinates are indicated by Miller indices, commonly referred to as hkl. For example, for a cubic lattice, the distance between a family of lattice planes is given by the following equation:

$$d = \frac{a}{\sqrt{h^2 + k^2 + l^2}} \tag{14}$$

where a represents the lattice parameter. By combining the equation 13 with 14, a combination of Miller indices can be matched to each diffraction peak. Moreover, since each lattice has only a few possible combinations of the Miller indices, comparing the diffraction structure obtained from the sample with the tabulated diffraction found in the literature can be obtained the crystalline structure characterizing the material of which the sample is composed.

X-ray diffraction (XRD) patterns were recorded employing a PANalytical X'Pert Pro automated diffractometer equipped with an X'celerator multielement solid-state detector. The diffractometer was operated in Bragg-Brentano focusing geometry using Ni-filtered Cu Kα radiation.

4.3.2 Scanning electron microscope

A scanning electron microscope (SEM) projects and scans a focused stream of electrons over a surface to create an image. The electrons in the beam interact with the sample, thereby producing various signals that can be used to obtain information about the surface's topography and composition. The main SEM components include:

- Source of electrons
- Column down which electrons travel with electromagnetic lenses
- Electron detector

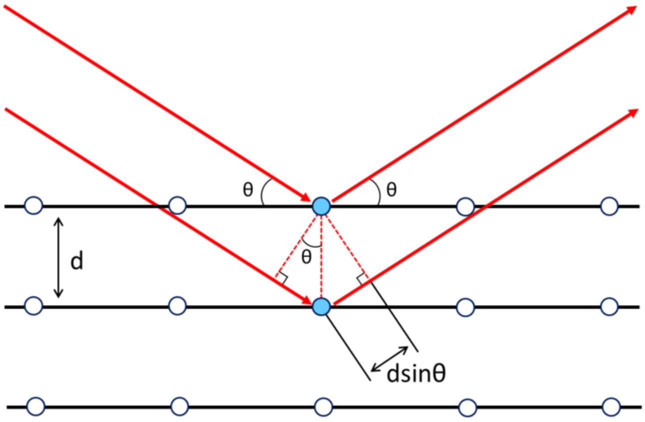

Figure 26: Geometric representation of the Bragg relationship.[21]

- Sample chamber
- Computer and display to view the images

Electrons are produced at the top of the column, accelerated down, and passed through a combination of lenses and apertures to produce a focused beam of electrons which then strikes the surface of the sample. The sample itself is mounted on a stage in the chamber area and both the column and the chamber are evacuated by a combination of pumps. The level of the vacuum will depend on the design of the microscope. The position of the electron beam on the sample is controlled by scan coils situated above the objective lens. These coils allow the beam to be scanned over the surface of the sample. This beam scanning enables information about a defined area on the sample to be collected. As a result of the electron-sample interaction, a number of signals are produced. These signals are then detected by appropriate detectors (Figure 27a).

As the electrons interact with the sample, they produce secondary electrons, backscattered electrons, and characteristic X-rays (Figure 27b). These signals are collected by one or more detectors to form images which are then displayed on the computer screen. When the electron beam hits the surface of the sample, it penetrates the sample to a depth of a few microns, depending on the accelerating voltage and the density of the sample. Many signals like secondary electrons and X-rays are produced as a result of this interaction inside the sample. The maximum resolution obtained in an SEM depends on multiple factors like the electron spot size and interaction volume of the electron beam with the sample. While it cannot provide atomic resolution, some SEMs can achieve resolution below 1 nm.

Back-scattered electrons (BSE) are the incident beam electrons that undergo an almost elastic reflection of 180°. The BSE signal is proportional to the atomic number of

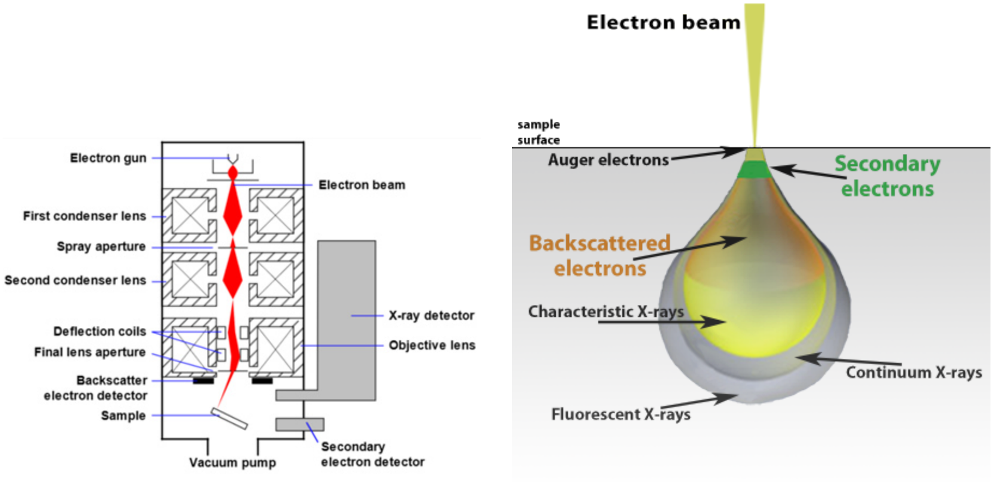

Figure 27: (a) Scanning electron microscope operation; (b) Electron beam interaction.[22]

the species, allowing a mapping with compositional information of the sample. Since the electrons coming from the beam are very energetic, they can penetrate up to a depth of about 1 μm, giving information about the inner structure of the sample. The secondary electrons (SE) are the product of the interaction of the beam with the valence electrons of the surface atoms. It is possible to detect only the outgoing electrons which do not undergo recombination processes and therefore come from a surface layer of about 5 nm. Their energy is therefore lower than the back-scattered electrons. The SE provide information related to surface morphology. The X-rays derive from the desiccation of atoms as a result of the ionization caused by the impact of the electrons of the primary beam with the electrons core atoms of the sample. A ionized electrons creates a hole that is filled by an electron coming from a more external shell; the energy dispersion in form of X-ray is the consequence of this transition. Each element has emission lines at different energy, which depends on its atomic number. By analyzing the X-rays that are emitted from the sample it is possible to obtain the atomic species that compose it. This type of analysis is called EDX (Energy Dispersive X-Ray).

The SEM used in the laboratory is called thermionic emission SEM, because the electron beam is obtained by heating a filament (usually tungsten) through the current flow; the beam is then accelerated towards the sample by a potential difference (about 40 kV) and focused by a system of magnetic lenses. The model used is the Cambridge Stereoscan 360.

5. Experimental results

In this chapter the main results of the electrodes characterization are shown. In particular, in the first paragraph, will be presented the films obtained with magnetron sputtering and the morphological, structural characterizations of each material. Subsequently, the electrochemical characterizations of the electrodes.

5.1 Characterization of multilayer electrode

We deposited the materials on three different substrates: silicon, glass, FTO and Mo. We used a silicon wafer for the morpholgical and chemical characterization. Silicon is highly pure, so we can perform an EDX characterization and knowing the silicon peaks we can get precisely the spectrum of the investigated material. Furthermore, when it is broken, silicon tends to break along the crystal lines. This means that we can break the wafer in order to get a section of the material.
Glass is used for the XRD characterization: it is amorphous and therefore does not introduce peaks in x-ray diffraction.
FTO (Fluorine-dopen Tin Oxide) and Mo is used as a backcontact for the electrical characterization.

5.1.1 CIGS

Deposition characterization

We deposited CIGS with a base pressure of $8 \cdot 10^{-3}$ mbar, and an argon flux of 20 sccm.
Changing the deposition parameters like temperature, RF power and deposition time affects the morphological and electrical property of the film. In particular, a series of morphological and electrical characterization of CIGS deposited with different parameters is in the figure 28, 29 and 30. In all the analyses made by SEM we can see that thickness of the CIGS change with the deposition parameters. In the first three results (Figure 28) with 1h of deposition, we increase the RF power from 30 to 80 W to get higher film but it never exceeded 250 nm of height. To get higher film, we increase the deposition time to 3h and 4h (Figure 29). With a deposition time of 3h and a temperature of 350°C we still got less than 700 nm of height. Bringing the deposition time to 4h we got strange and very high elongated worm-like structures of CIGS with a temperature of 450°C. Finally, in figure 30, a good film of CIGS was achieved with 4h of deposition,

80 W of RF power and temperature of 350°C.

characterization of composition

The EDX analysis allow to found the percentage of elements in the deposited layer. We have make the analysis for three different CIGS deposition layer at different temperature: 250-350-450°C (RF power = 80W, time = 4h).

As we can see from the figure 31, the percentage of the elements in the deposited layer varies slightly. There seems to be an excess of Se, In compared to Ga and Cu compared to In+Ga. The values tend to reach the target values as the temperature increases.

Structural characterization

We perform XRD measurements on the obtained films. The result are shown in figure 32a. We can see the XRD profiles of the three films obtained, with three different temperatures of deposition, 250°C, 350°C, 450°C. We obtain one peak higher then the other. This is a consequence of the type of deposition: the crystals tend to be oriented in the same direction, increasing only the contribution of one peak. Therfore, we can confirm that all the samples exhibit polycrystalline chalcopyrite structural $CI_{0.7}G_{0.3}S_2$ phase with a preferential orientation along the (112) direction. In the figure 32b we can see the intensity and the FWMH of the peak as a function of the temperature deposition. The intensity of (112) peak increases with the increasing substrate temperature, indicating a better crystallinity of the samples. In addition, using the Debye-Scherrer inverse relation:

$$\tau = \frac{K\lambda}{\Delta(2\theta)cos\theta} \tag{15}$$

where τ is the width of a crystal, K is a dimensionless shape factor (with a value close to unity), λ is the X-ray wavelength, $\Delta(2\theta)$ is the line broadening at half the maximum intensity (FWHM) and θ is the Bragg angle; we can associate the width of a crystal with the FWMH of the peak. It show that the peaks are very thin, denoting large crystals.

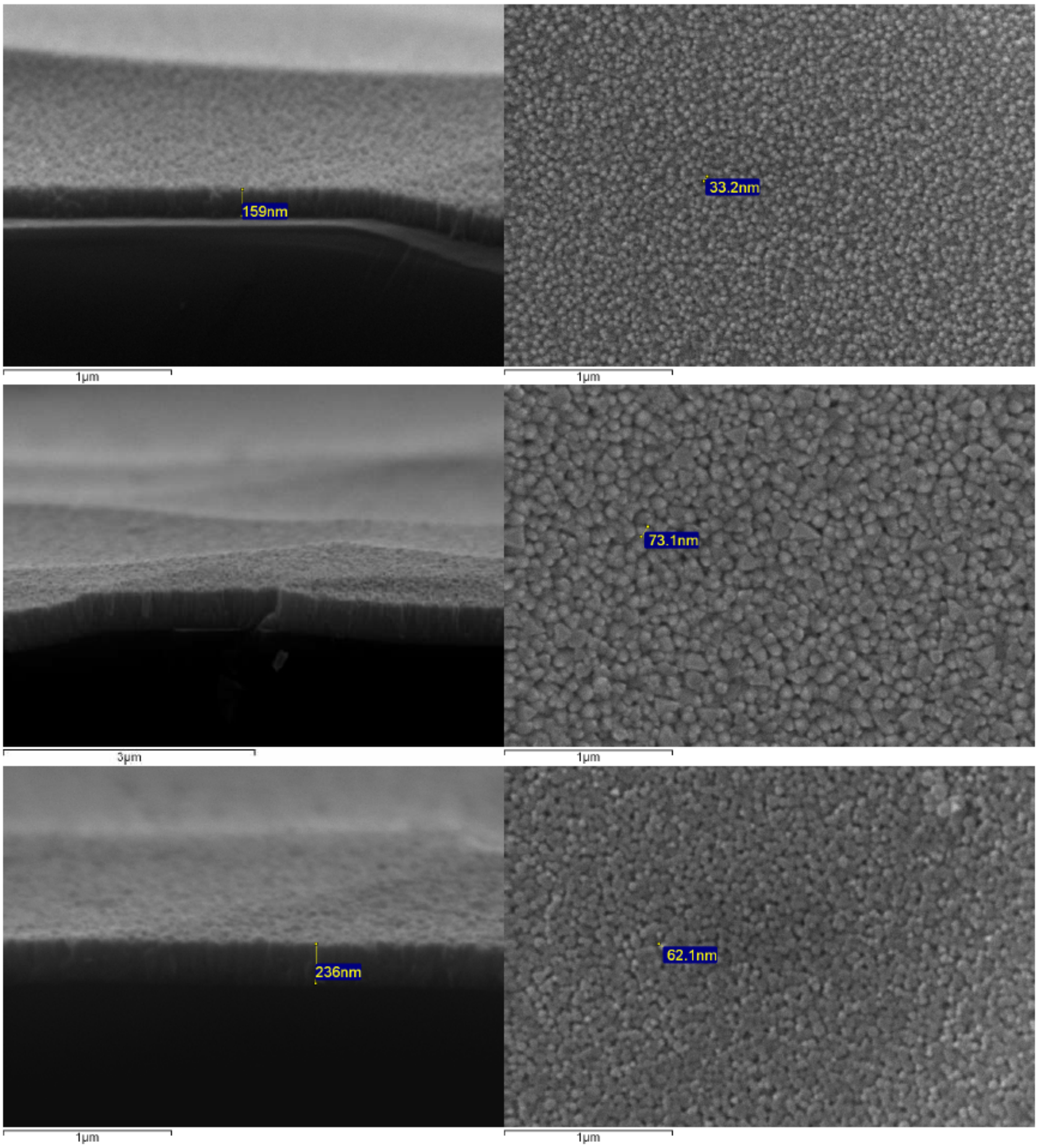

Figure 28: CIGS deposited with the following parameters: (a) RF power = 30W, time = 1h, T = 450°C; (b) RF power = 40W, time = 1h, T = 450°C, (c) RF power = 80W, time = 1h; T = 450°C.

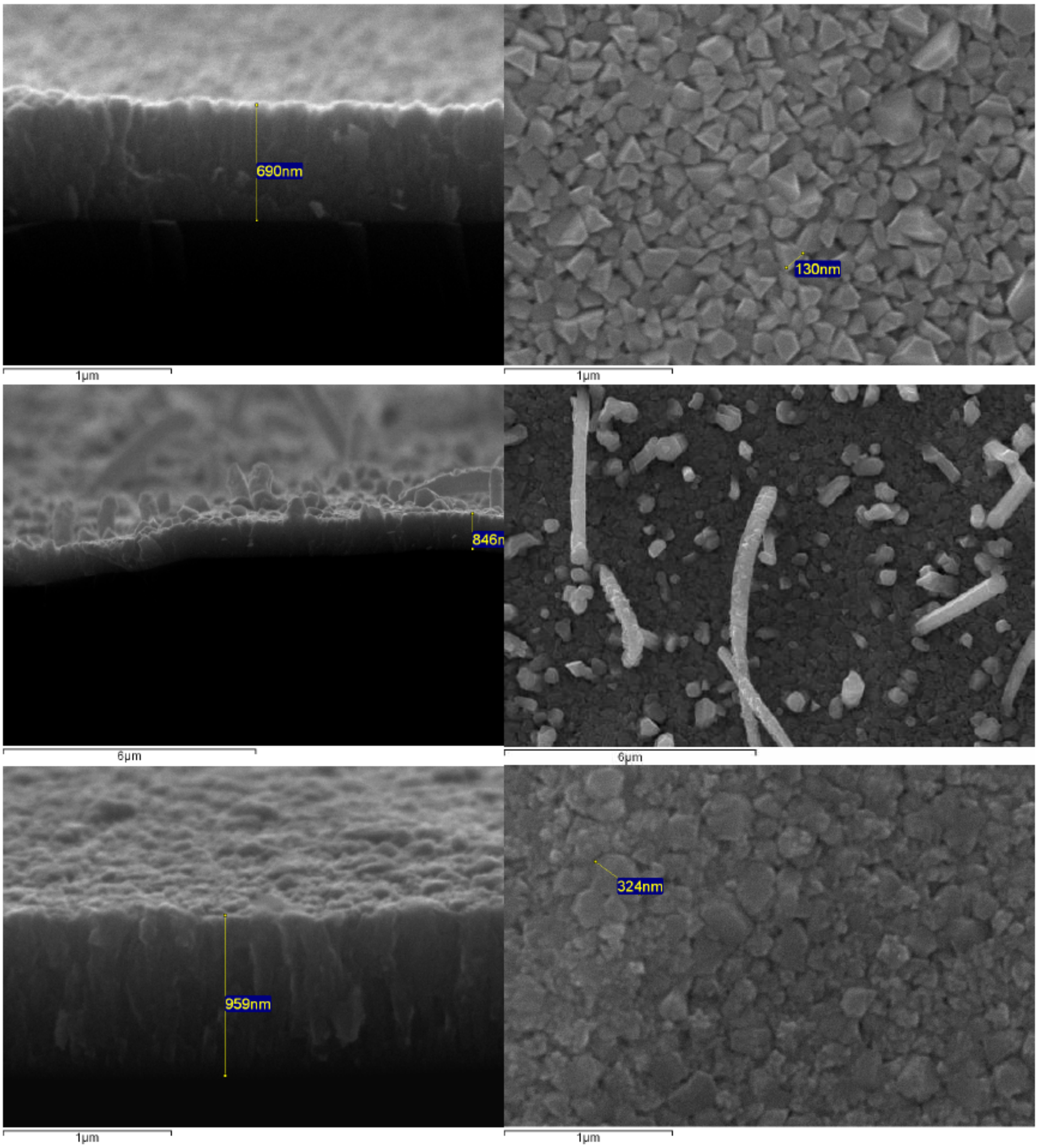

Figure 29: CIGS deposited with parameters: (a) RF power = 80W, time = 3h, T = 350°C; (b) RF power = 80W, time = 4h, T = 450°C, (c) RF power = 80W, time = 4h; T = 250°C.

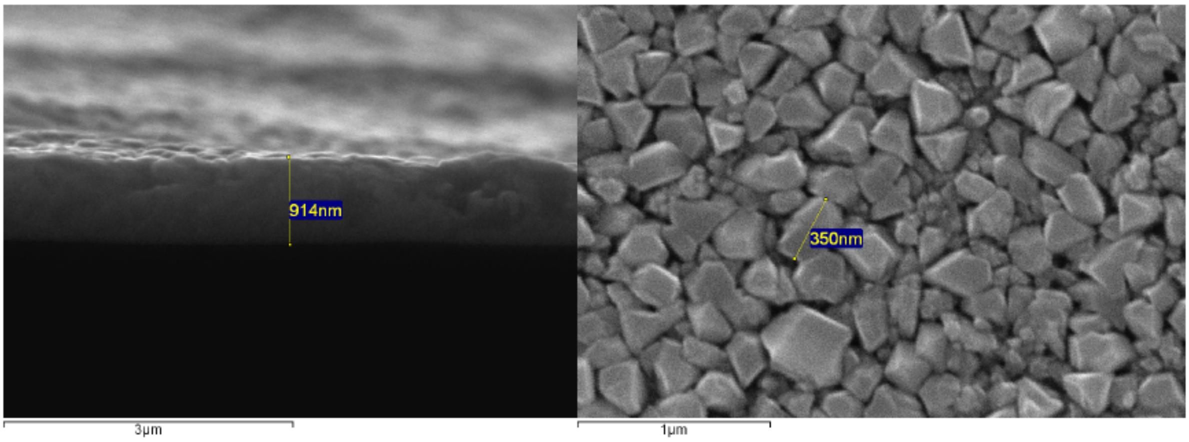

Figure 30: Good film deposition of CIGS with: RF power = 80W, time = 4h, T = 350°C

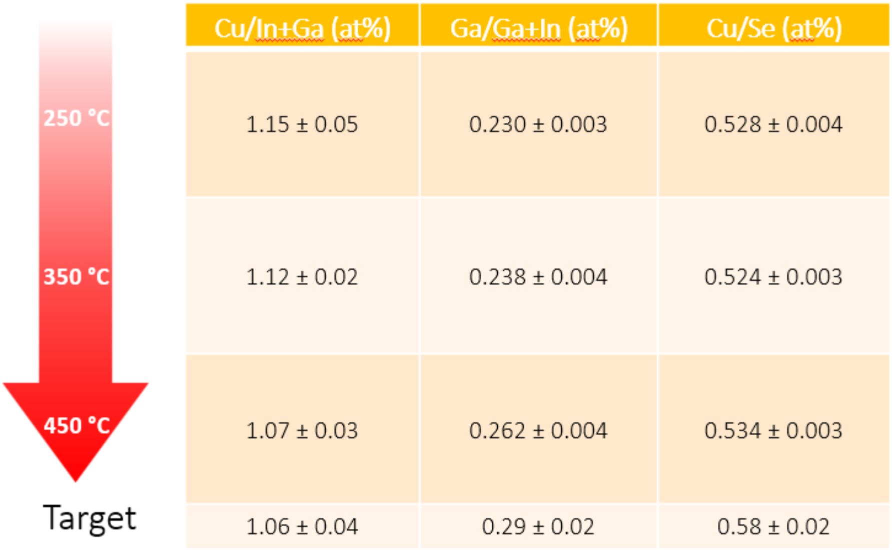

	Cu/In+Ga (at%)	Ga/Ga+In (at%)	Cu/Se (at%)
250 °C	1.15 ± 0.05	0.230 ± 0.003	0.528 ± 0.004
350 °C	1.12 ± 0.02	0.238 ± 0.004	0.524 ± 0.003
450 °C	1.07 ± 0.03	0.262 ± 0.004	0.534 ± 0.003
Target	1.06 ± 0.04	0.29 ± 0.02	0.58 ± 0.02

Figure 31: EDX analysis on CIGS deposition layer at temperature 250-350-450°C.

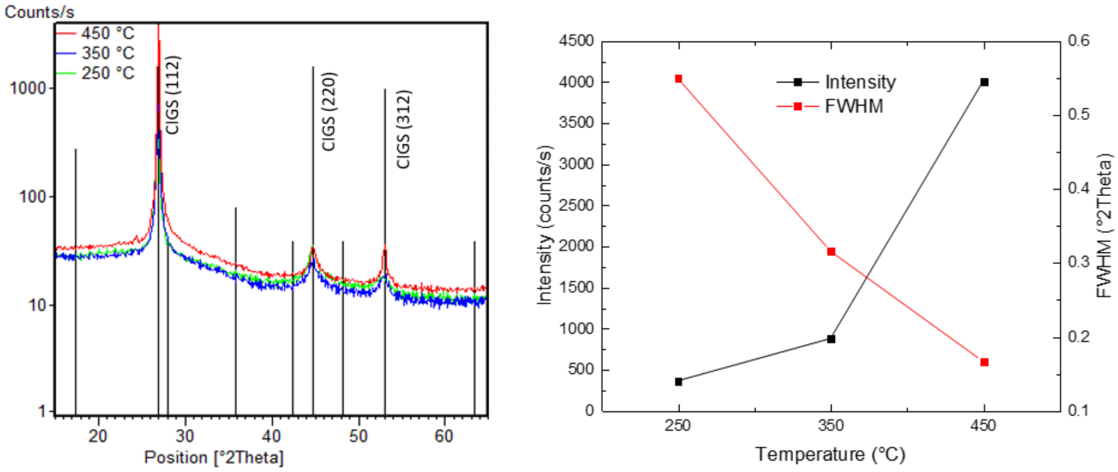

Figure 32: (a) XRD spectra of three CIGS deposition layer at T = 250-350-450°C (RF power = 80W, time = 4h); (b) The crystalline extension in the direction of the scattering vector, i.e. perpendicular to the film plane.

Band gap measurement

A measure of the optical spectra of the obtained thin film can give us information about the band gap of the material. Transmission experiment was performed with an optical bench that we show in figure 33b. The transmision spectrum is obtained using a diffraction grating that divide intensitiy of differents wavelengths. From the transmittance spectrum we get the absorbtion coefficient, from which we can get Tauc plot. From a linear fit in the increasing region, we can get the value of the band gap: in fact, when the energy of the photons is below the value of the band gap, they are transmitted, and the absorption coefficient is very small. When the photons exceed band gap energy, they start to be absorbed by electrons promoted to the conduction band. As we can see from figure 33a, we get a value of band gap of about (1.16-1.16-1.19 ± 0.01)eV respectively, comparable with the theoretical value of 1.2 eV and with those presents in literature.[23]

Resistivity measurement

The resistivity is measured with a two point measurement in the case of bulk resistance and a four point measurement in the case of sheet resistance (Figure 34a, 34b). The two wires measurement for sheet resistance is actually unrealizable. It is always affected by a great systematic error: the 'wire' resistance as well as the contact resistance is always added in series to the sample resistance. In the four points method, instead, the voltmeter measures the voltage drop across the two inner contact, sourcing the current of sample with the outer contacts. Furthermore, the precision in the distance between

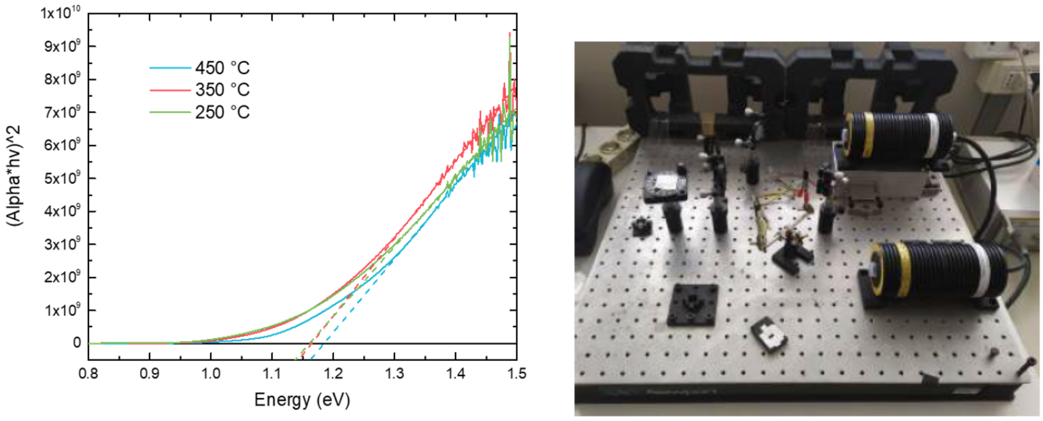

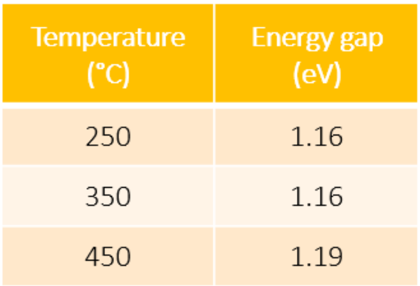

Temperature (°C)	Energy gap (eV)
250	1.16
350	1.16
450	1.19

Figure 33: (a) Tauc plot of the obtained CIGS; (b) Optical bench for the transmission measurements; (c) Energy gap result.

the tips is not so important in the two point measurements but become very important in the case of four point measurements. If the distance between the tips is too high or the tips are not aligned the measure can be compromised. We chose a 2 mm distance between the tips. The measured resistivity as a function of the deposition temperature is shown in figure 35. The resistivity values are in agree with those in the literature. In particular, it is observed that the resistivity increases up to a deposition temperature of about 400 °C, then begins to decrease at higher temperatures.[] This could be due to higher deposition temperature that contributes to larger crystalline grain which increases carrier mobility.

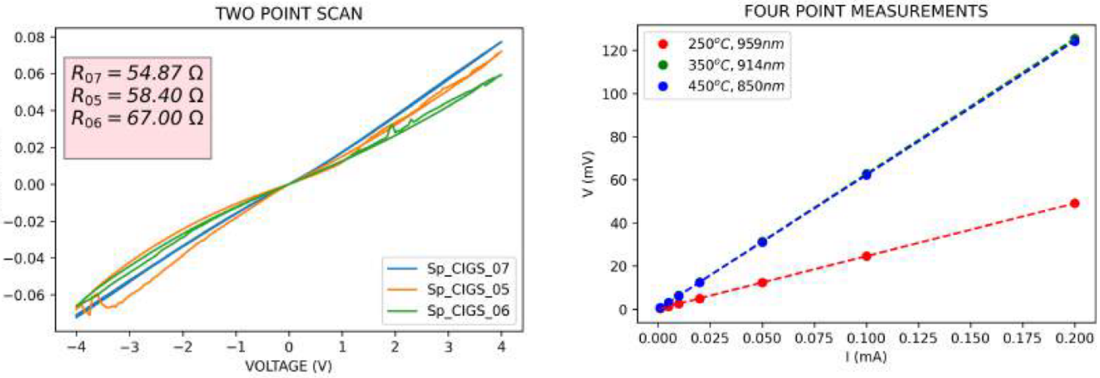

Figure 34: (a) Two point measurement. Sp-CIGS-05-06-07 is the layer deposited at 250-350-450 °C respectively. We got a resistivity of: 54.9 Ω, 58.4 Ω and 67 Ω; (b) Four points measurements.

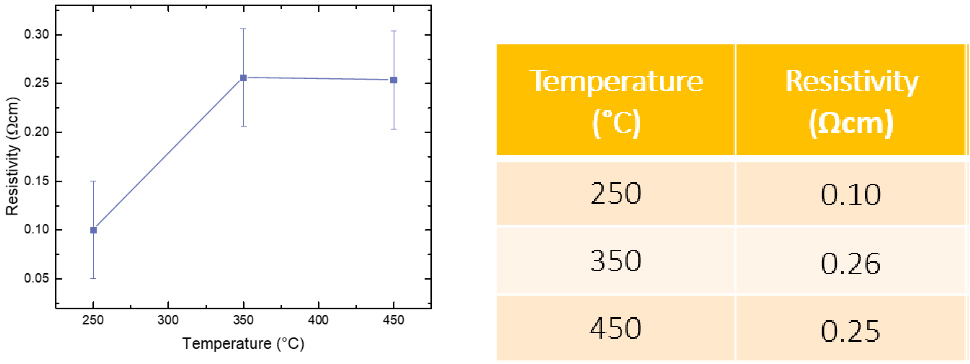

Temperature (°C)	Resistivity (Ωcm)
250	0.10
350	0.26
450	0.25

Figure 35: (a) Resistivity as a function of the deposition temperature; (b) Resistivity result.[]

5.1.2 CdS

Deposition characterization

For the deposition of the thin layer of CdS, we started from a deposition at room temperature with an RF power of 50W and for a duration of 4h (Figure 36a) on a silicon substrate. In order to decrease the size of the film we reduced both the power of the RF to 30W and the duration of the deposition to 3h, obtaining a film of about 200 nm (Figure 36b). Finally, we attempted a deposition at a temperature of 100 ºC to increase the homogenity of the deposited layer, not achieving a better result (Figure 36c). We then returned to a deposition at room temperature (RF power = 30W) for a duration of 1:30h in order to obtain a film size between 50-100nm. We want to remark the fact that this is only an extrapolation and a nominal value, since we have not a SEM able to resolve this scale.

Structural and electrical characterization

Structural characterization was performed on samples deposited for 3h at an RF power of 30W and at temperatures of 100 ºC and RT.
For XRD measurements (Figures 37a) the main peaks of the present materials are observed. Again, we get very thin peaks that denote large well-oriented crystals.

The electrical characterization is carried out by depositing a thin layer of CdS (RF power = 30W, T = RT, t = 1:30h) on FTO substrate.
For the electrical characterization of the thin film CdS, we used the same setup to make 2-point measurements for bulk resistance and 4-point measurements for sheet resistance. We expected sheet resistance in the order of magnitude 103-104 Ω and ohmic behavior in bulk resistivity. We obtained different result: a dielectric behavior in the sheet resistance and a diode behavior in bulk resistance measurements (Figure 37b, 37c). We think that the characteristic of the diode can be explained by considering the CdS-FTO as a semiconductor-metal junction that creates a charge accumulation at the interface due to the contact and, therefore, a change in Fermi energy. This type of behavior is known as Mott-Schottky contact. For our purposes, this behavior can be a problem because the CDS that we are getting can influence the overall behavior of the device due to its interaction with FTO and its very high sheet resistance.

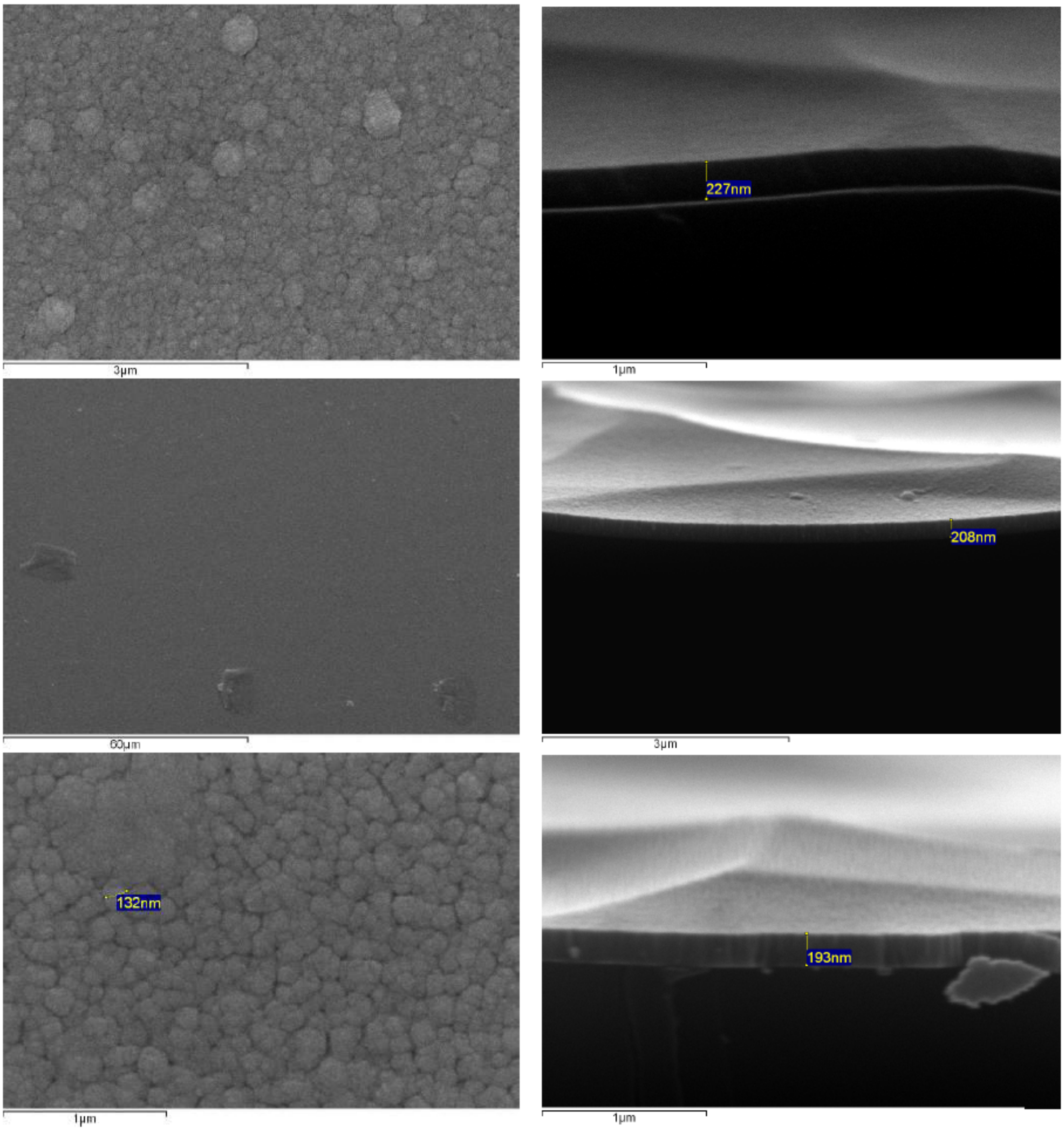

Figure 36: Thin deposited layer of CdS: (a) RF power = 50W, time = 4h, T = RT; (b) RF power = 30W, time = 3h, T = RT, (c) RF power = 30W, time = 3h; T = 100°C.

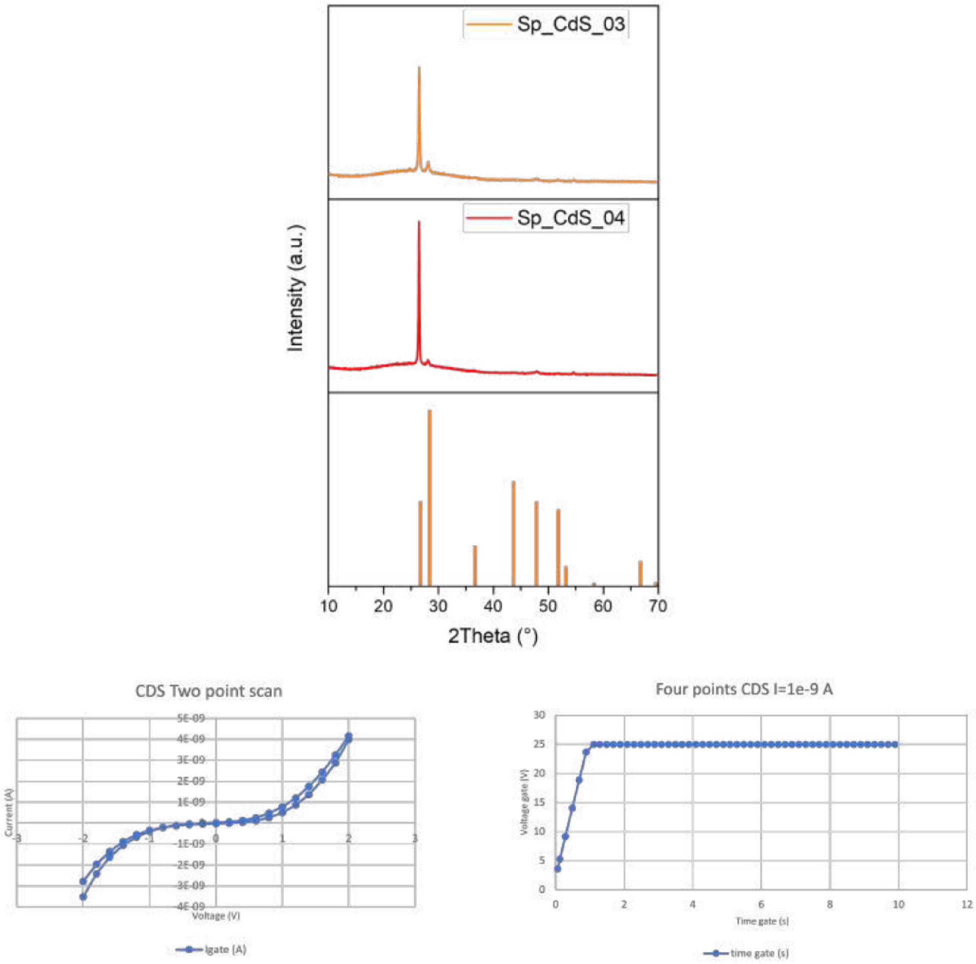

Figure 37: (a) CdS XRD characterization: the samples analysed were deposited at RF power = 30W, t = 3h and T = RT (SP-CdS-03), 100°C (SP-CdS-04); (b) and (c) Electrical characterization of CdS thin film.[24]

5.1.3 CIGS/CdS

Deposition and structural characterization

As a starting point for our research we take parameters and results present in literature for the CIGS/CdS junction. In [24] is deposited a CIGS-CdS with 350-50 nm of width. In literature, CIGS cells are build with 1 μm of CIGS and 300 nm of CdS.[25] In order to obtain a very thin film of CdS, of about 50 nm, the deposition of the CdS over the CIGS are performed with RF power = 30W, T= RT and t = 1:30h and the CIGS deposition is made with RF power = 80W, T = 350°C and 4h of deposition time. The obtained device is a CIGS-based pn junction with about 900nm of CIGS and 50nm of CdS (Figure 38).

The obtained XRD are shown in figure 39. The XRD confirms the elements present in the film.

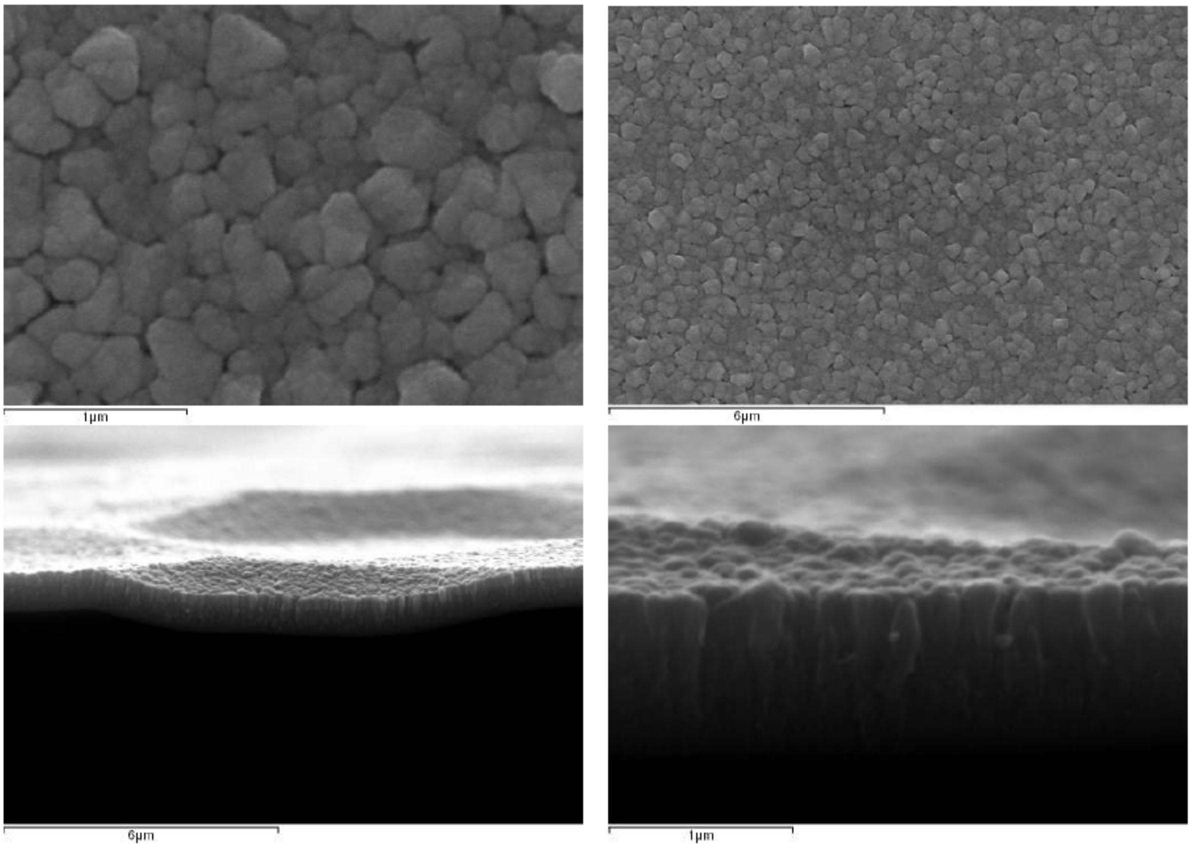

Figure 38: CIGS/CdS juction: (a) Top view of CIGS/CdS morphology at two different scales (1 μm and 6 μm); (b) Section of CIGS-CdS at scales of 6 μm and 1 μm. Difficult to observe the presence of the cds because of its reduced thickness compared to the CIGS.

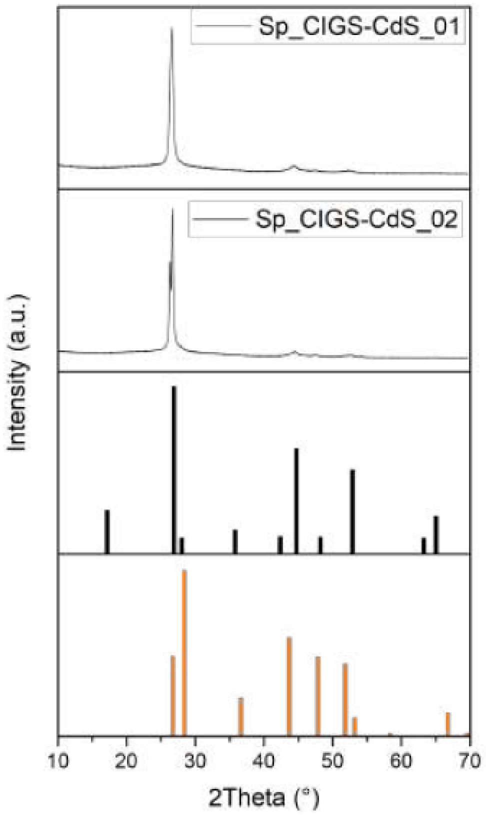

Figure 39: XRD spectra of 2 samples of CIGS-CdS: in the bottom panel are present the expected peaks of CIGS and CdS respectively.

5.1.4 CIGS/CdS/TiO_2

I want to remark the main usage of TiO_2: it is commonly used in photoelectrochemical cells as both for its great stability in water and for its good Fermi energy, it tends to favour cathodic reactions.

Deposition characterization

The TiO_2 was deposited over the CIGS/CdS with a RF power of 75W, at room temperature and for a duration of 45 min of deposition time. The morphological characterization of the deposition of TiO_2 was made by Scanning Electron Microscope. From the figure 40, we can see that the CdS and TiO_2 are very thin films above the CIGS. The limit of the used SEM is about hundred of nm, therfore, it is impossible to give precise measures of the thickness of the CdS and TiO_2 layer. We can extrapolate a measure of the TiO_2 of about 50 nm, as such as the CdS. Over the TiO_2 was not performed electrical characterization since we used it not as contact but as a stabilizer.

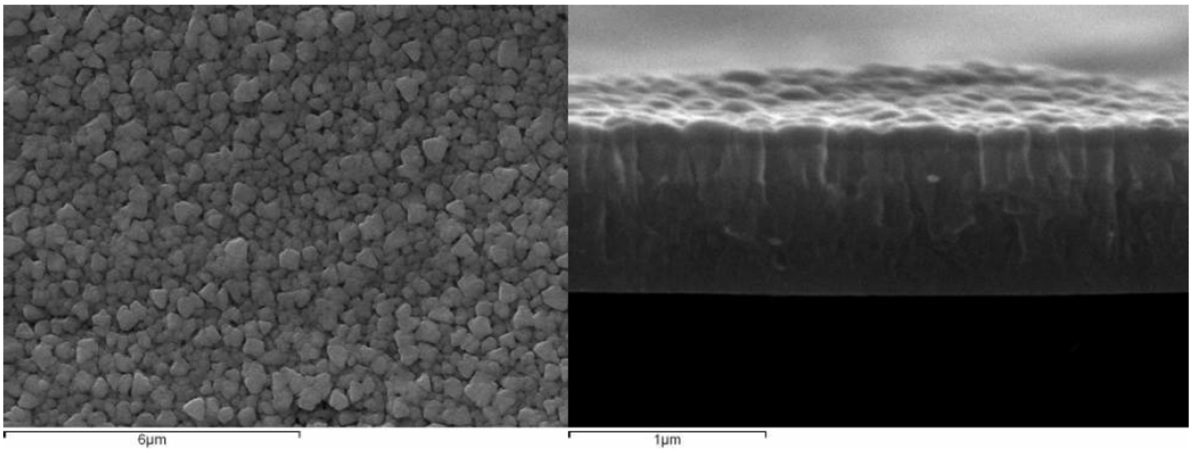

Figure 40: Top and section view of CIGS-CDS-TiO_2 thin film. It is possible to see the different layers over the CIGS.

5.1.5 AZO

In order to find a layer both conductive and stable in water, we use AZO over the CdS layer. The AZO is a promising material since it is conductive and it is an oxide, this means that it could be very stable in water or in solution.

Deposition and structural characterization

We deposited AZO, that is conductive and transparent material, with RF magnetron sputtering with a FR power of 40W, at room temperature and 2:20 h of deposition time. The section of the sample confirms the sample size of about 80 nm as we see in figure 41a.

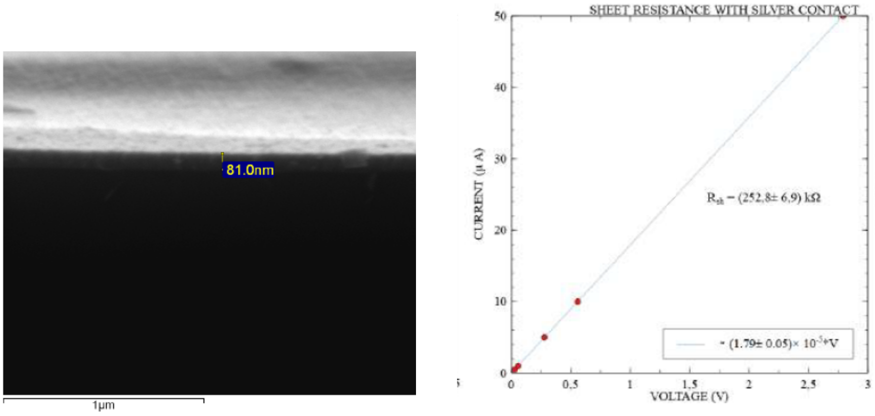

Regions	Elemental Composition (at %) O	Al	Si	Zn	Al/(Al+Zn)
Region 1	40,25	0,82	35,48	23,45	3,378657
Region 2	51,3	1,03	23,83	23,84	4,141536
Region 3	43,15	1,15	22,29	33,42	3,326584
Region 4	51,03	0,86	19,24	28,87	2,892701
Region 5	34,82		36,27	28,91	0

Figure 41: (a) Deposition characterization of AZO: we get a layer of about 81 nm of thickness; (b) Sheet resistance: (252.8 ± 6.9) kΩ. It seemed not to be conductive; (c) EDX spectra result for different regions of the sample.

In order to obtain information about the conductivity of the AZO, we made a four points measurement to get its sheet resistance (Figure 41b). We made the measurement using a Ar paste to avoid contact problem and so a change of current during the measurement. Anyway, the sheet resistance obtained (about 250 kΩ) is four orders of magnitude out of the expected one (order of Ω). The AZO seemed not to be conductive.
As we said, its conduction is due to both the presence of Al and the presence of oxygen vacancy. After an EDX spectrometry towards the AZO surface (Figure 41c), it was clear that the concentration of Al in the material was not homogeneous. It seems that Al

tend to forms clusters with high density of Al in certain regions, whereas in others it was absent. This can be a cause in the drop of conductivity, or the presence of very good conductivity regions and regions with very poor conductivity. Furthermore, the multimeter measurements of the AZO soon after it was taken out from the oven told us that the AZO is a good conductor (hundreds Ω). But after a few time, the same measurements became three order of magnitude bigger. This suggested that the vacancy of oxygen, important for the conductivity of AZO, could be fullfilled when AZO is in contact with air. Thus, the corrosion of the oxygen vacancy determines a drop in conductivity.

In any case, we tested these multilayer electrodes on the PEC device to determine the photoelectrochemical characteristics of charge generation and transmission.

5.2 Electrochemical characterization

We have prepared several multilayer electrodes for their characterization in the PEC cell:

- CIGS/TiO_2 (CT)
- CIGS/CdS/TiO_2 (CCT)
- CIGS/AZO/TiO_2 (CAT)
- CIGS/CdS/AZO/TiO_2 (CCAT)

Each of these thin layers have been deposited with the techniques and characteristics described in the previous paragraph.
The goal of this analysis is to analyze how each thin layer of material carries the charges to the next interface.
Each of these multilayers were deposited on an FTO (F) substrate and a Molybdenum (M) substrate as a back-contact.

5.2.1 Open Circuit potential

The OCP measurement give us the potential in which there is no current that flows in the device and it is related to an equilibrium of oxidation and reduction at the surface of the film. It was found by changing the potential of the counter electrode until the current in the cell was null. OCP measurement is a characteristic measurement of a film and a PH solution. It tells us a lot about the working point of the device, and it is important for the next measurements.[26] We performed OCP chopper measurements

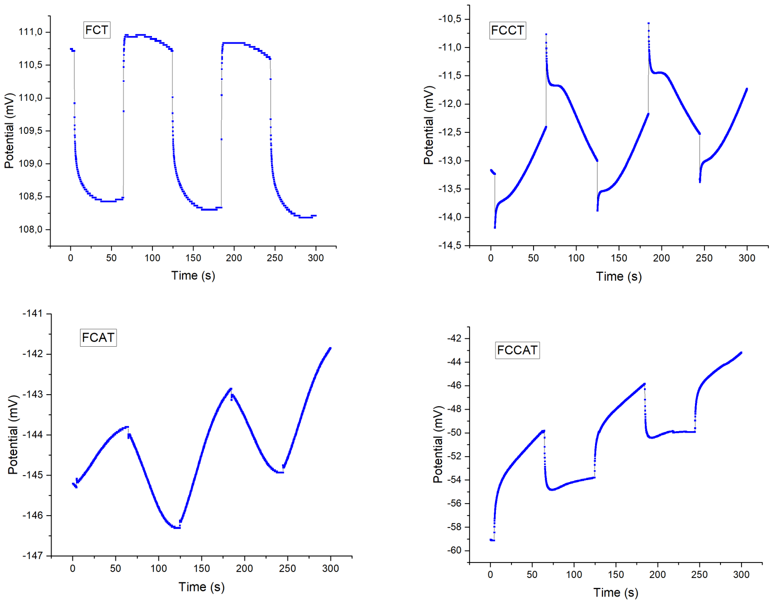

Figure 42: OCP measurement of different multilayer on FTO substrate: (a) FTO/CIGS/TiO_2 (FCT); (b) FTO/CIGS/CdS/TiO_2 (FCCT); (c) FTO/CIGS/AZO/TiO_2 (FCAT); (d) FTO/CIGS/CdS/AZO/TiO_2 (FCCAT).

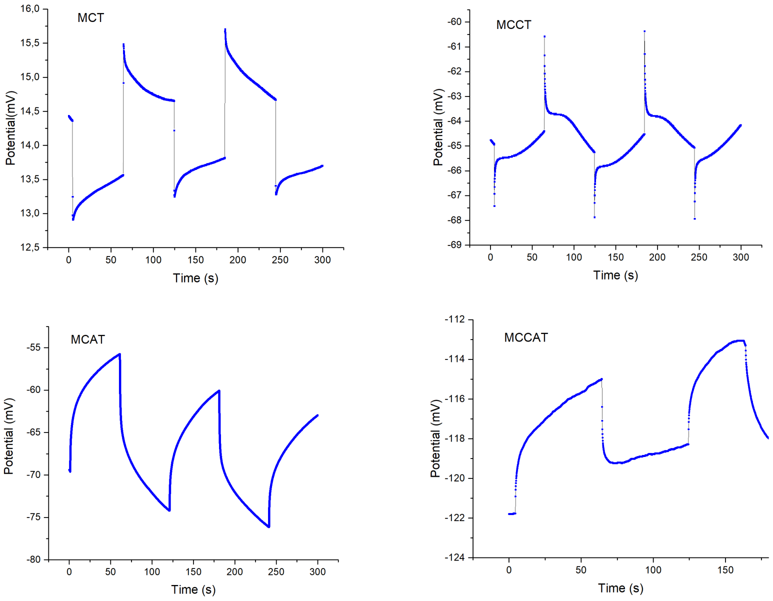

Figure 43: OCP measurement of different multilayer on molybdenum substrate: (a) Mo/CIGS/TiO_2 (MCT); (b) Mo/CIGS/CdS/TiO_2 (MCCT); (c) Mo/CIGS/AZO/TiO_2 (MCAT); (d) Mo/CIGS/CdS/AZO/TiO_2 (MCCAT).

with a time interval of 60s between dark and light. In the figures are shown the results of measurements on both FTO (Figure 42) and Mo substrate (Figure 43).

From the figures we can observe different phenomena of generation and recombination of charges based on the presence or not of the thin layers deposited. In particular: in CIGS/TiO_2 electrodes the process of generating charges is almost instantaneous, then, after a few milliseconds, a recombination phenomenon is observed; in CIGS/CdS/TiO_2 electrodes, again, the generation of charges occurs instantaneously, but the process of recombination happens more quickly, moreover, different phenomena of recombination are observed with different times and characteristics. With the presence of AZO, the process of generating charges is slower than the electrodes without the layer of AZO, an evident effect of the low conductivity of the deposited material. The back-contacts of FTO and Mo do not seem to vary the processes mentioned above.
Finally, a true OCP value could not be determined in these measurements because of the large fluctuations observed. In any case, the OCP values do not exceed tens of mV. For the subsequent measurements it was decided to apply a potential up to -0.3V compared to the reference (RE), to avoid degradation of the electrodes during the examination measurements (actually, we arrived at a potential of -0.5V, but the corrosion of the electrode was present visually).

5.2.2 Linear Sweep voltammetry

Linear sweep voltammetry is a voltammetric method where the current at a working electrode is measured while the potential between the working electrode and a reference electrode is swept linearly in time.[27]
We made these measurements in order to detect how the current varies according to the voltage applied (vs RE) in the various samples. In particular, we compared these measurements in case of dark and light, at different scan rates and between different samples. In the results given below, only comparisons between the different samples will be shown, since in the other characterizations there are only small changes in the current trend. In particular, between dark and light, the trend and the current values reached is about the same; increasing the scan rate from 0.01 to 0.02 V/s the current values reached slightly increases. Finally, we repeated this voltammetric method at the end of the subsequent measurements in order to determine the degree of corrosion of the multilayer electrodes under examination.

Figures 44 and 45 show the analysis of the data by comparing the trend of the current between different electrodes.

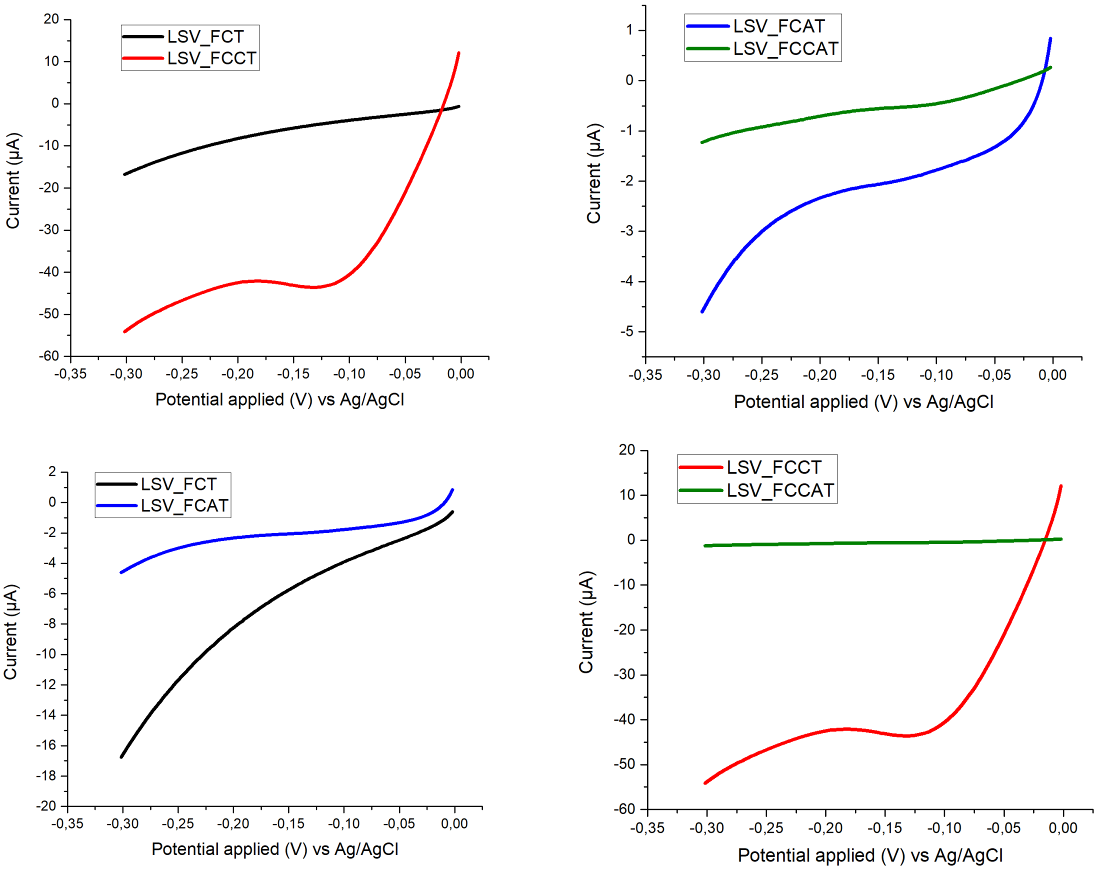

Figure 44: LSV measurement of different multilayer on FTO substrate: (a) and (b) compare different trends based on the presence or absence of CdS; (c) and (d) compare different trends based on the presence or absence of AZO.

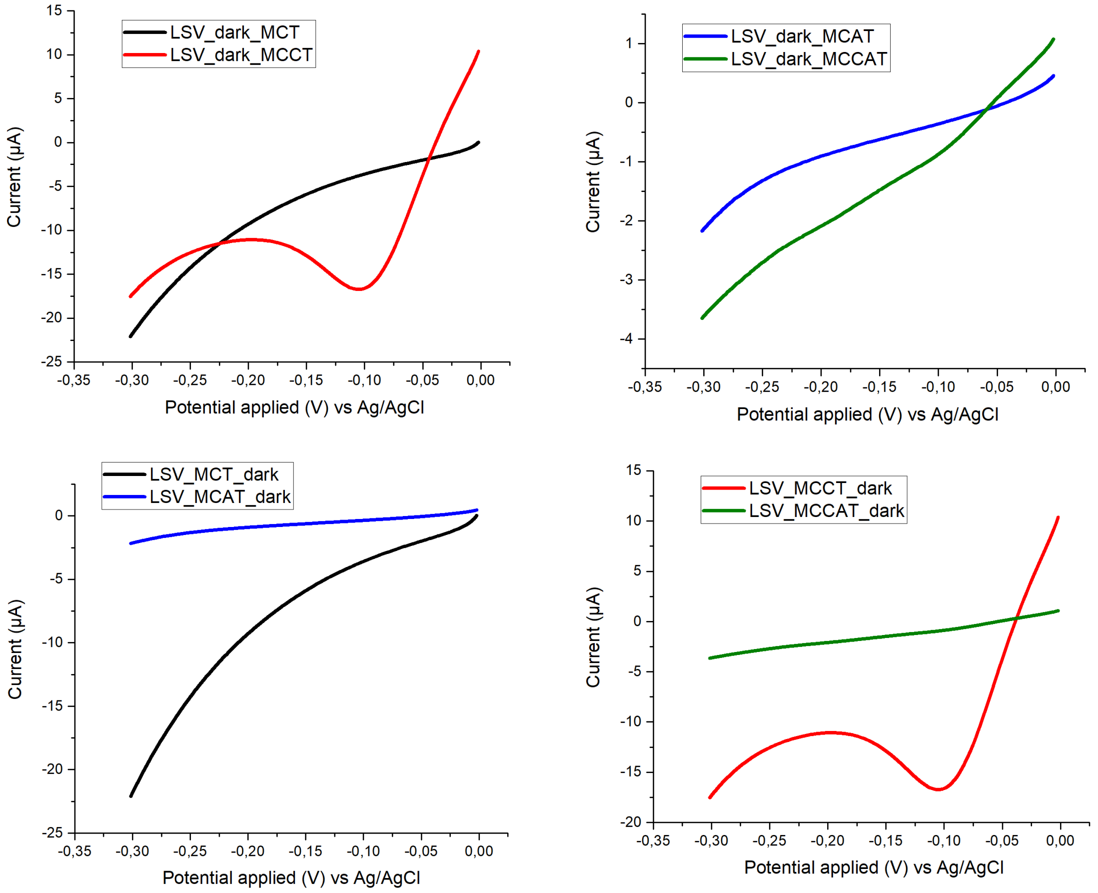

Figure 45: LSV measurement of different multilayer on molybdenum substrate: (a) and (b) compare different trends based on the presence or absence of CdS; (c) and (d) compare different trends based on the presence or absence of AZO.

Depending on the present or not of several thin layers of materials, the current-voltage characteristic of the various electrodes varies considerably.

With the presence of the CdS layer, in the case of the electrodes on the FTO substrate (Figure 44a, 44b), a different trend of the current is observed. The peak (or plateau) showing the function, with the presence of the CdS, could be associated with the highest velocity at which electrons are exchanged through the electrode-electrolyte interface, with respect to the rate at which reducing species can diffuse from the mass of the electrolyte to the surface of the electrode.[] In addition, the current, at the potential value of -0,3V vs RE, reaches a value about four times greater than the electrodes without the presence of the CdS layer.
In the electrodes with the molybdenum substrate (Figure 45a, 45b), the same trends are observed in the form of functions, less evident in the samples with the presence of AZO. In this case, unlike the previous ones, the current values are about the same.
Independent of the substrate used, the obvious characteristic of the presence of the AZO layer is the value of the current as the applied voltage increases. In particular, at a voltage of -0.3V with respect to the RE, a lower current of orders of magnitude ranging from 5 (MCT-MCAT) to 60 (FCCT-FCCAT) is observed. This shows how the thin layer of AZO is an obstacle to the proper functioning of the device.

In the figure 46, the current-voltage characteristics of the electrodes with the molybdenum substrate are observed after subsequent analysis (about 1:30h in cell). The graphs show that the shape of the function varies slightly, but the value of the current as the voltage increases remains almost the same. This shows that the samples do not degrade excessively with time and with this potential applied. In addition, after removing the electrodes from the cell, no visible corrosion was observed.

5.2.3 Transient Photocurrent

I report the transient photocurrent studies on the charge transport of the electrodes in analysis.
We performed this analysis at a potential value of -0.3V vs RE and alternating light and dark with an interval of 60 seconds, in order to stabilize the response and calculate the photocurrent produced by the different samples. The data analyses are shown in figure 47. I have shown the analysis only for the sample without the AZO layer, as they exhibit a higher activity for the reasons mentioned above.

As we expected, from the figure we observe a photocurrent produced on the order of μA, about 3 orders of magnitude less than our objectives (mA). In particular, on samples with FTO substart, the thin layer of CdS increase the activity of the electrode, while on samples with molybdenum substrate, the activity remains almost the same. A confirmation of the LSV analysis results, the MCT and MCCT electrodes have similar

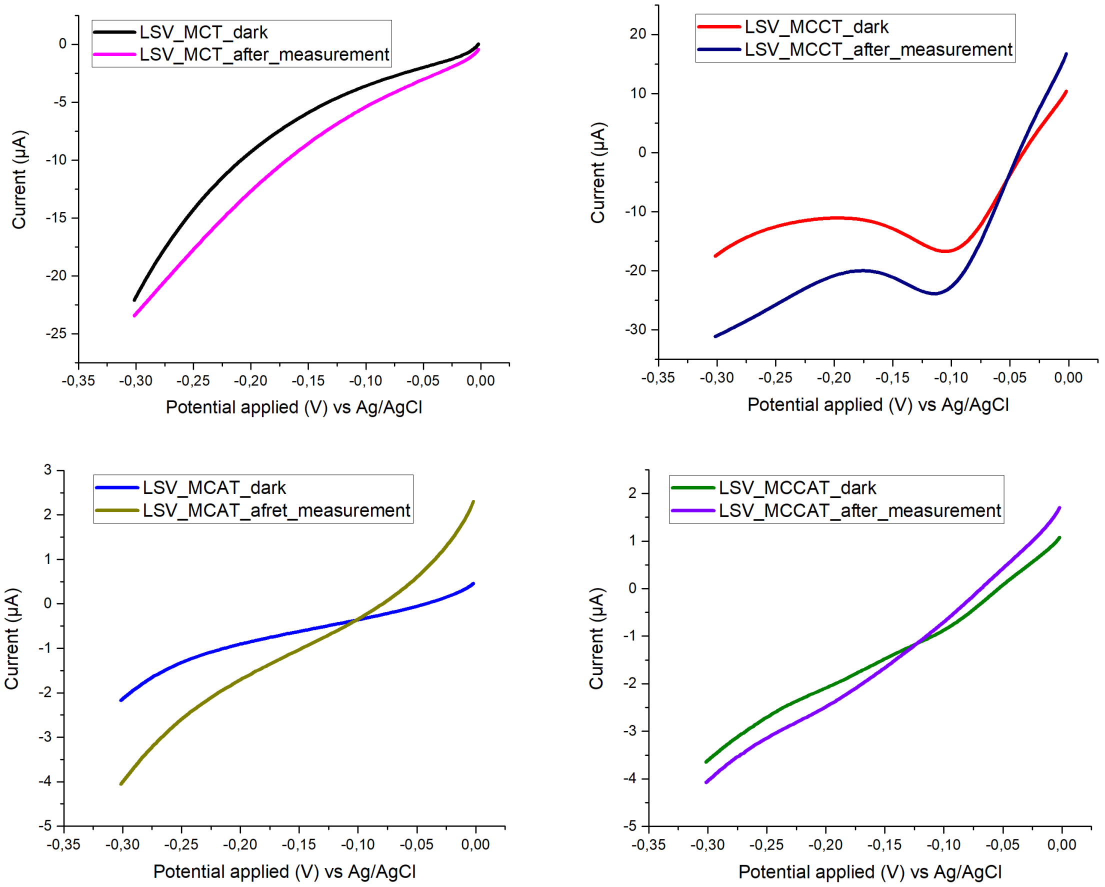

Figure 46: LSV measurement after about 1:30h with electrodes in cell: (a) Mo/CIGS/TiO_2; (b) Mo/CIGS/CdS/TiO_2; (c) Mo/CIGS/AZO/TiO_2; (d) Mo/CIGS/CdS/AZO/TiO_2.

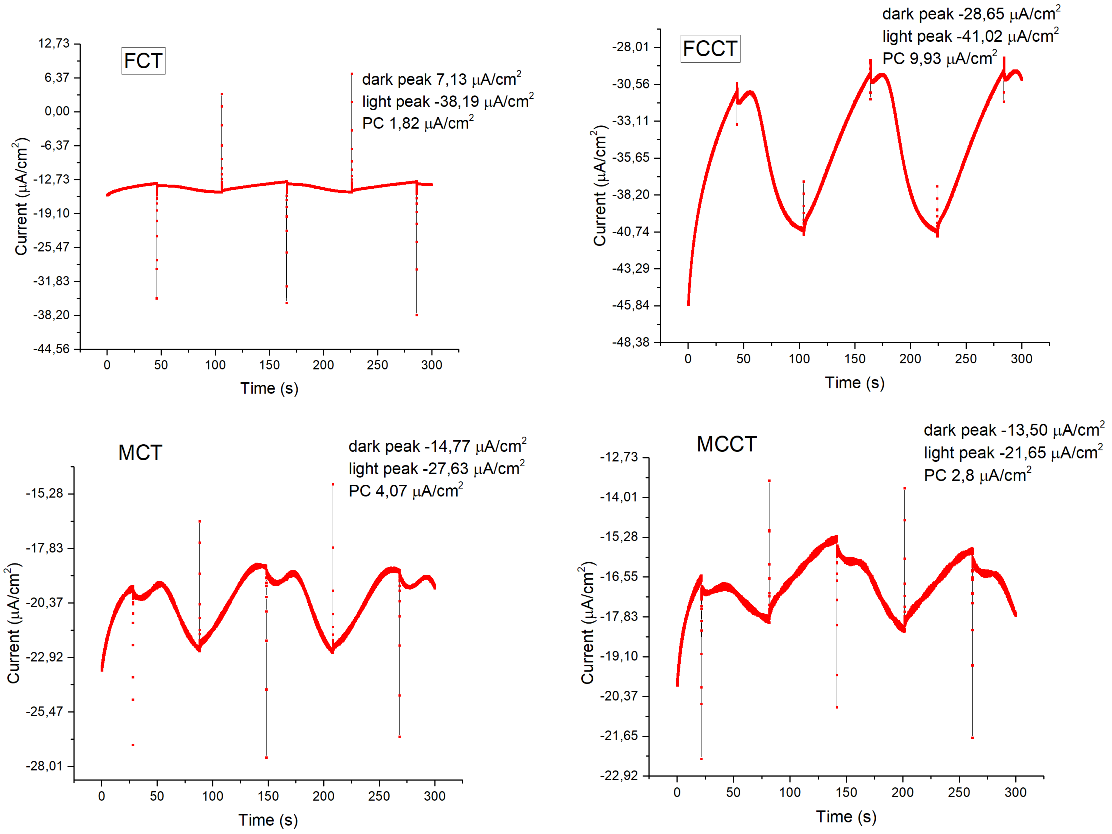

Figure 47: Transient photocurrent measurement for samples without AZO layer: (a) FCT, photocurrent detected = 1,82 $\mu A/cm^2$; (b) FCCT, PC detected = 9,93 $\mu A/cm^2$; (c) MCT, PC detected = 4,07 $\mu A/cm^2$; (d) MCCT, PC detected = 2,8 $\mu A/cm^2$.

current values, compared to the applied potential, while the FCCT electrode reaches current values about 5 orders of magnitude higher than FCT, even at low potentials (such as OCP).

5.2.4 Electrochemical Impedance Spectroscopy

Electrochemical impedance spectroscopy (EIS) is a technique which is used to measure the impedance of an electrochemical system. The approach of EIS is to apply a small amplitude sinusoidal excitation signal to the system under investigation and measure its response. A low amplitude sine wave $\Delta E sin(\omega t)$ a fixed frequency ω is superimposed on the DC polarization voltage applied to the working electrode, resulting in a current response of a sine wave superimposed on the DC current $\Delta i sin(\omega t + \phi)$ current response is shifted in phase with respect to the applied potential. This approach relies on the low magnitude perturbation of the system, so that the first Taylor series expansion factor for the current can be considered a good approximation to the total current response. The impedance of the system can be calculated using Ohm's law:

$$Z(\omega) = \frac{E(\omega)}{i(\omega)} \tag{16}$$

in which $Z(\omega)$ is the total impedance of the system and is a complex quantity with a magnitude and a phase which depends on the frequency of the signal. Therefore, by varying the frequency of the applied signal it is possible to obtain the impedance of the system as a function of the frequency. Typically, in electrochemistry a frequency range from 100 kHz to 0.1 Hz is used.

Data from EIS measurements are usually represented by using two different plots: the Nyquist plot and the Bode plot. The Nyquist plot consist to plot the negative imaginary impedance –Z" versus the real part of the impedance Z'. The Bode plot is actually two plots in one. The abscissa (x-axis) is a logarithmic scale of the frequency and one ordinate (y-axis) is the logarithm of the impedance Z while the second ordinate is the phase shift ϕ.

It is common to create an electronic circuit that represents the electrochemical system under investigation. A fit of the spectrum based on this equivalent circuit is made to identify the contribution of the single components. These models are built starting from passive element such as resistors, capacitors and inductors. The circuit is composed by combining these elements in series or in parallel and a certain physical meaning is then assigned to the various elements.

The simplest component is the resistor. As a result there is no phase shift ($\phi = 0°$) and the impedance Z, which is equal to R in this case, is independent of the AC frequency. This is visible in the Bode plot by two constant parallels to the abscissa. In the Nyquist plot a single point with Z" = 0 and Z = R is visible (Figure 48a).

Another very common element that is often encountered in real experiments is the capacitor. Capacitors store charge. Since the charge Q that can be stored is proportional to the applied potential, changing the potential at higher frequencies, will result in higher currents flowing, which means the impedance Z is low. Reducing the frequency of the AC potential will lead to a higher Z. This means that at a very high frequency a capacitor has no contribution to Z and at very low frequencies Z goes towards infinite. The phase shift ϕ of an ideal capacitor is 90° and the impedance Z is calculated according to:

$$Z_{cap} = \frac{1}{\omega C} \tag{17}$$

As a result the Bode plot shows a constant phase of 90° and a linear curve with a negative slope and the Nyquist plot shows a straight line along the ordinate (Figure 48b). Capacitors are easily formed in an electrochemical experiment. The ions in front of the electrode and the electrons (or their deficiency) in the electrode, form a capacitor (the electrochemical double layer) with a huge impact on electrochemical measurements. Unfortunately, other electronic components can form a capacitor as well. This happens at high frequency and leads to stray capacitance.

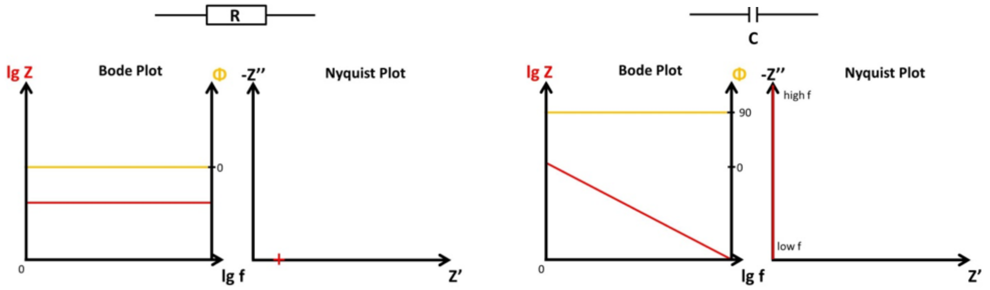

Figure 48: Representation of resistor and capacitor element in the equivalent circuit model: (a) Nyquist and Bode plot for resistor element; (b) Nyquist and Bode plot for capacitor element.[28]

A Capacitor and Resistor can be combined in different ways with rather different effects. If the connection is serial, the impedance Z can't be smaller than R. The capacitors impact decreases with increasing frequency. The resulting Nyquist and Bode plots can be seen in Figure 49a. A more interesting effect is observed when the resistor and the capacitor are in parallel. The current chooses the path of the lowest impedance. The impedance of the capacitor is frequency-dependent, which means the path the current choose will change: at high frequencies the impedance of the capacitor will be very low and the major part of the current will flow through the capacitor. With decreasing frequency the impedance of the capacitor increases and a bigger fraction of the current flows through the resistor. When the majority of the current flows through the resistor, the total imaginary resistance Z" will drop as the real part Z' increases. Since the

Nyquist plot represents the complex plane and each value is a complex number, so the axes should have the same scale. Under this condition an ideal capacitor in parallel with a resistor leads to a semicircle (Figure 49b).
This circuit is already quite close to a real system. The capacitor represents the electrochemical double layer C$_{dl}$, which can only store charge. The resistor represents the charge transfer resistance R$_{ct}$. This is the resistance for the electron to change the phase, e.g. from the electrode into the solution.

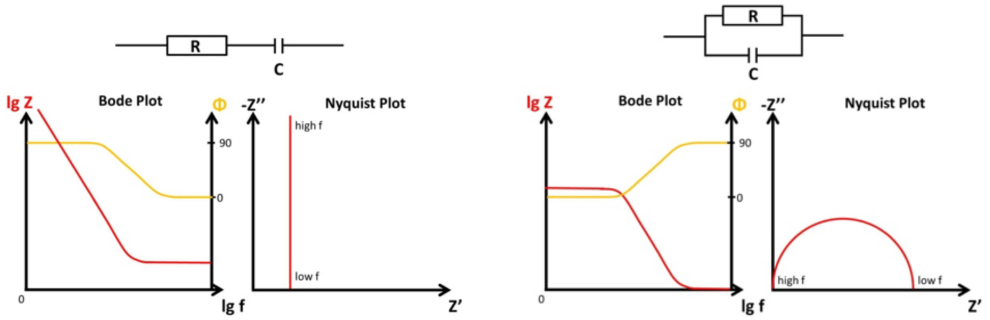

Figure 49: Representation of RC in series and in parallel in the equivalent circuit model: (a) Nyquist and Bode plot for RC in series; (b) Nyquist and Bode plot for RC in parallel.[28]

The model we refer to in our EIS measures is the Randles model (Figure 50).

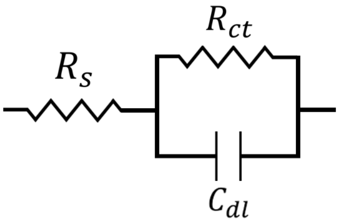

Figure 50: Randles circuit.[28]

The parallel resistance takes into account the flow of charge that follows the chemical reactions that take place at the semiconductor/electrolyte interface. In particular, at high frequencies C$_{dl}$ is close to 0 and the main contribution comes from the R$_{sol}$. So the beginning of the semi-circle is R$_{sol}$. At low frequencies the C$_{dl}$ has very high impedance and all the current goes through R$_{ct}$. So the impedance contribution at the point where the right end of the semi-circle would hit the 0 of the y-axis is R$_{sol}$ + R$_{ct}$. So R$_{sol}$ and R$_{ct}$ can easily be estimated just by looking at the semi-circle.[] Furthermore, the C$_{dl}$ could be calculated from the frequency at the highest point of the semi-circle (maximum of Z") ω_{max} using:

$$C_{dl} = \frac{1}{R_{ct}\omega_{max}} \tag{18}$$

In figures 51 and 52 show the EIS measurements carried out on our samples at -0.3V in light, over a frequency range of 100000 to 0.1 Hz. The fits were obtained using a NOVA software tool, where an equivalent circuit can be set for each EIS measurement. As we can observe from the associated equivalent circuits, it was not possible fit the data only with classic electronic components.

The current can go through the interface of the working electrode by capacitive current caused by the electrochemical double layer, represented by the double-layer capacity C_{dl}, which requires an electron transfer and so needs to go through the charge transfer resistance R_{ct}. Up to here, the expected EIS would be a semi-circle just as for the Randles circuit. If a free diffusing species is converted at the electrode, this behavior is not observed. At low frequencies oxidizing or reducing potentials are held long enough that depletion of the species in front of the electrode becomes relevant. The depletion of species in front of electrodes is well understood and described by the Cottrell equation.[29] Due to the lack of species in front of the electrode, fewer species are converted and less current flows while the same potential is applied. During an EIS measurement, this is measured as an increase in impedance. This increase is represented by the Warburg Impedance W, which is a virtual electronic component only used to make equivalent circuits for electrochemical experiments. The Warburg element's impedance is calculated by:

$$Z_W = \frac{\sigma}{\sqrt{\omega}} - j\frac{\sigma}{\sqrt{\omega}} \tag{19}$$

where Z_W is the impedance of the Warburg element and σ is the Warburg coefficient also known as A_W (it has the unit of $\Omega/s^{1/2}$ and it depends on the diffusion coefficient and the concentration of the species in the bulk of the oxidized and reduced species). The Warburg impedance is an example of a constant phase element and it is visible in the Nyquist plot as a straight line with a 45° angle to the abscissa.

The obtained values, shown in figure 53, confirm our hypothesis: the R_{ct} resistances are only a result of the fit and have no physical significance, they are too small ($\mu\Omega$). Our electrodes have a very low charge transfer resistance, leading to a dominance of the Warburg impedance. These results confirm a depletion of the species in front of the electrode, therefore, fewer species are converted and less current flows.

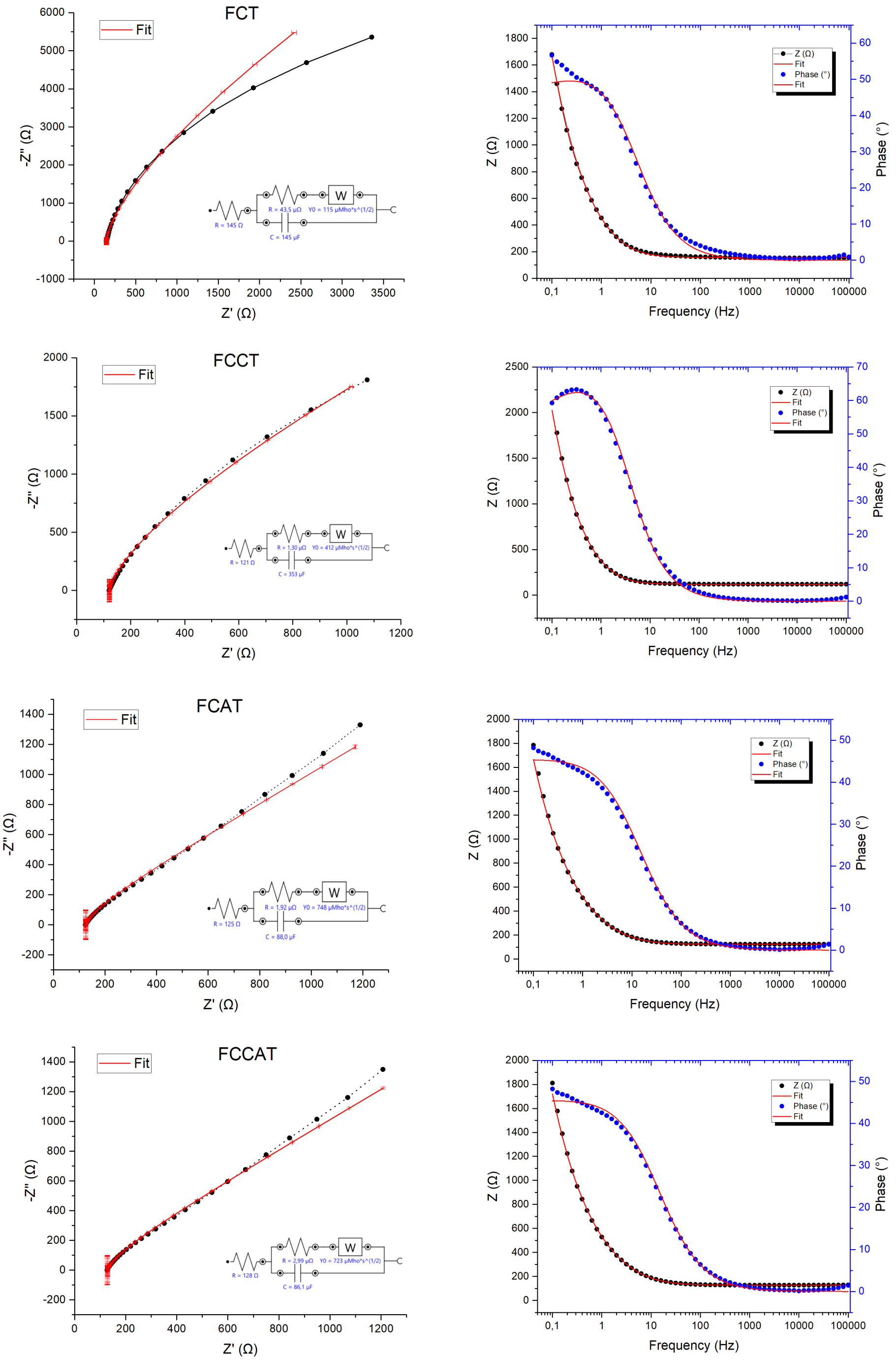

Figure 51: Electrochemical impedance spectroscopy on the electrodes on the FTO substrate. It is shown the Nyquist and Bode plot and the relative equivalent circuit.

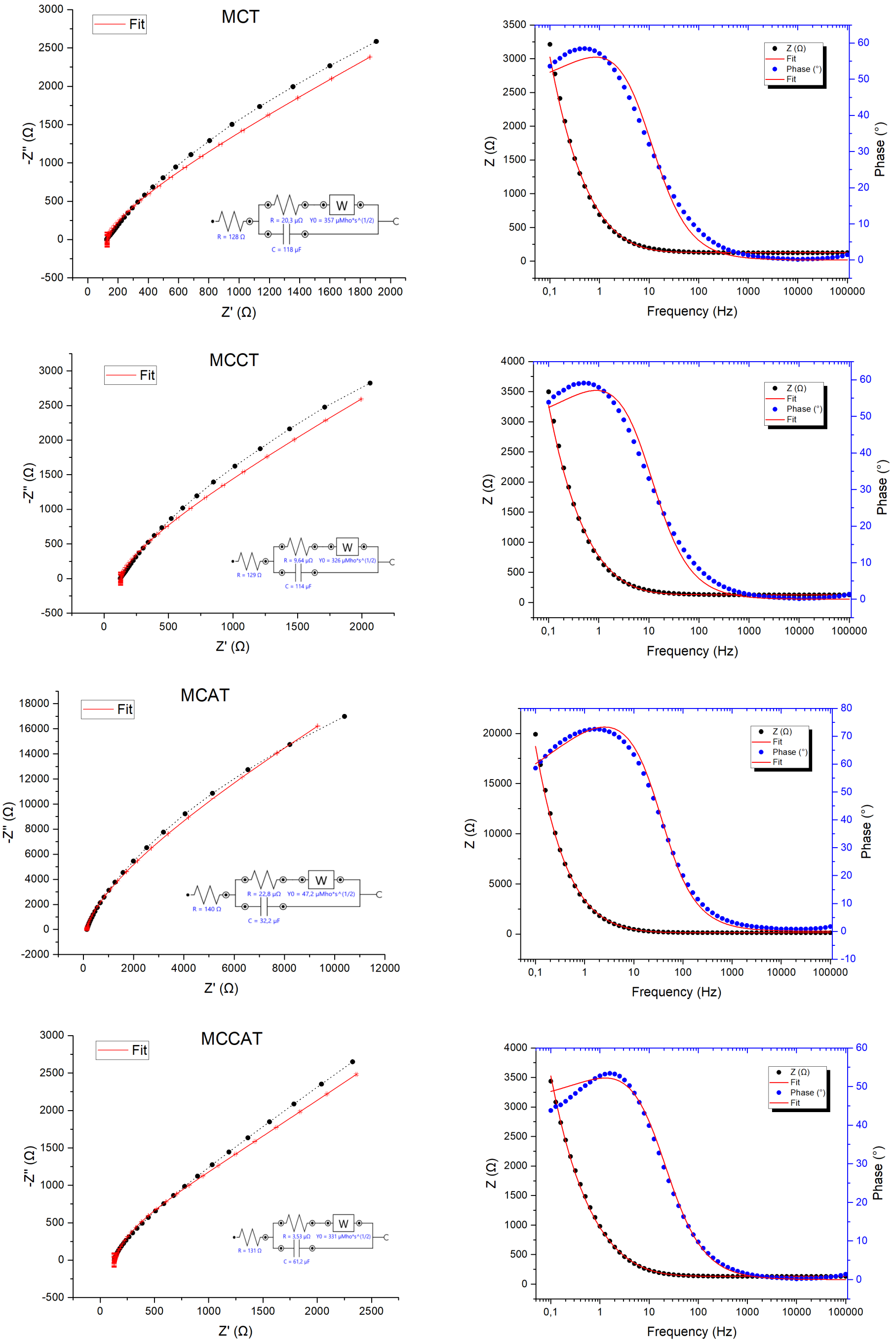

Figure 52: Electrochemical impedance spectroscopy on the electrodes on the molybdenum substrate. It is shown the Nyquist and Bode plot and the relative equivalent circuit.

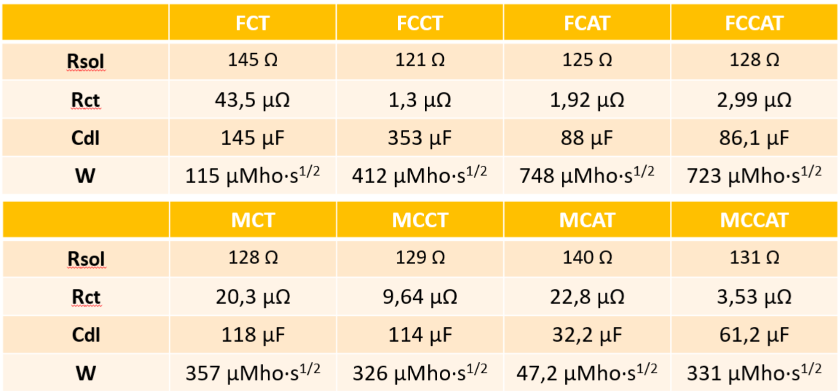

	FCT	FCCT	FCAT	FCCAT
Rsol	145 Ω	121 Ω	125 Ω	128 Ω
Rct	43,5 μΩ	1,3 μΩ	1,92 μΩ	2,99 μΩ
Cdl	145 μF	353 μF	88 μF	86,1 μF
W	115 μMho·s$^{1/2}$	412 μMho·s$^{1/2}$	748 μMho·s$^{1/2}$	723 μMho·s$^{1/2}$

	MCT	MCCT	MCAT	MCCAT
Rsol	128 Ω	129 Ω	140 Ω	131 Ω
Rct	20,3 μΩ	9,64 μΩ	22,8 μΩ	3,53 μΩ
Cdl	118 μF	114 μF	32,2 μF	61,2 μF
W	357 μMho·s$^{1/2}$	326 μMho·s$^{1/2}$	47,2 μMho·s$^{1/2}$	331 μMho·s$^{1/2}$

Figure 53: (a) Circuit element values of samples on FTO substrate; (b) Circuit element values of samples on Mo substrate.

6. Conclusion

The work done for this thesis is divided into three phases: the development of multilayer electrodes based on CIGS through the technique of RF magnetron sputtering, their composition and structural characterization and finally an electrochemical characterization carried out in the cell.
In the first phase, I initially integrated the software in Labview for remote control of the radio frequency machine (for more details see Appendix A), then we started the deposition of materials of our interest starting from the characteristics of the deposition found in literature, then we modified these parameters according to the characteristics of the deposited layers related to our purposes.
In the second phase, we used the SEM, and the EDX analysis, present in our laboratory and the diffractometer present in the laboratories of the chemistry department for structural and composition characterization. We obtained good results for the various layers of deposited material except for AZO where EDX analysis showed significant fluctuations in the presence of Al on the deposited layer.
In the last step, we tested the performance of the electrodes in the cell. We performed OCP analyses that showed different types of charge generation and recombination depending on the layers present. LSV analysis, to obtain the current-voltage characteristic. This analysis showed how the thin layer of CdS changes the shape of the function by presenting peaks or plateaus associated with a higher velocity at which the electrons are exchanged through the electrode-electrolyte interface, with respect to the rate at which reducing species can spread from the mass of the electrolyte to the surface of the electrode. In addition, we have verified that the AZO layer tends to block the charge transmission associated with a low conductivity. This feature was further verified by

a four-point measurement obtaining a sheet resistance of more than 4 orders of magnitude compared to the expected one. The TPC analysis, has the objective to verify the photocurrent produced by the various electrodes. We have obtained results not very rewarding. In particular, for each electrode the photocurrent did not exceed a few tens of μA, while our objectives were to obtain photocurrent of the order of mA. This results showed that our samples are not yet ready for a photocathode activity. The last analysis is EIS measurements. The related data were fit from an equivalent Randles circuit, where it was necessary to add a Warburg impedance (a virtual electronic component). This characteristic is attributable to a significant depletion of the species in front of the electrode causing a lower conversion of the species and less current flows. This means that our electrodes have a very low charge transfer resistance ($R_{ct)}$, which leads to a dominance of the Warburg impedance.

In conclusion, the electrodes produced have a good stability in the working conditions used, but a photocurrent obtained too low to meet the needs required. A possible step forward could be achieved by creating a better conductivity AZO layer. Despite the good conductivity of the CIGS layer and its optical absorption in the visible, range, the electrodes display low photocurrents. It appears therefore that the material, or the interface with CIGS, suffers from heavy recombination of photogenerated charge carriers. It is known that high-quality CIGS-based solar cells require several optimization steps, including doping with alkali elements, gradients in Cu concentration, and formation of a $MoSe_2$ layer at the interface with the Mo back contact. While the initial hope of this work was to obtain photoelectrodes with good performance in spite of the simplicity of the preparation procedure, the obtained results indicate that this is not possible without further treatments.

Appendix A

Software development in LabView

During my experience I integrated a software in LabView for remote control of the RF machine.
The software is based on the state machine architecture. A state machine is a programming architecture that allows dynamic flow to states depending on values from previous states or user inputs. A state can be defined as the status within the program while accomplishing the overall task of the program; examples of states may be initializing, waiting, running a calculation, checking status, etc. Events can be used to trigger moving from one state to the next; these can be programmatic events or user-defined, like pressing a button. To translate the state diagram into a LabVIEW programming architecture, you need the following infrastructure:

1. While Loop – continually executes the various states
2. Case Structure – each case contains code to be executed for each state
3. Shift Register – contains state transition information
4. Transition code – determines the next state in the sequence

At startup, the program is located in an initialization case structure (Figure 54), where it set the connection with Arduino, with the RF machine via a serial connection and initializes a cluster of arrays and a numeric value.

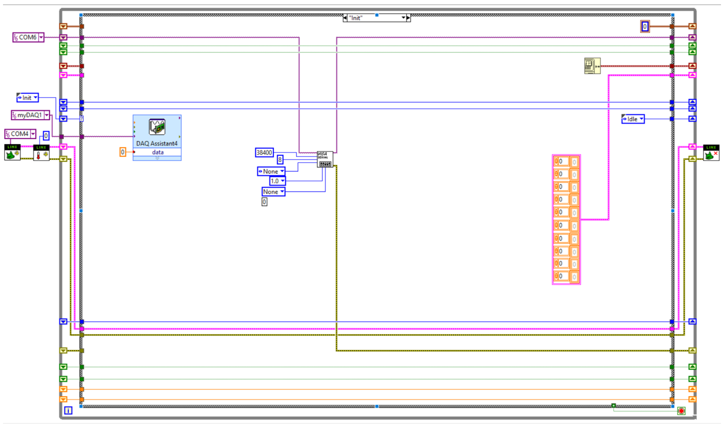

Figure 54: Initialization

Next, in a case idle in the figure 55, the program starts a Boolean value check of various switches, based on the last true value the program will be addressed in that specific label (case). After each cycle the program is directed into the idle case and start a new check of the respective boolean values and a subsequent cycle.

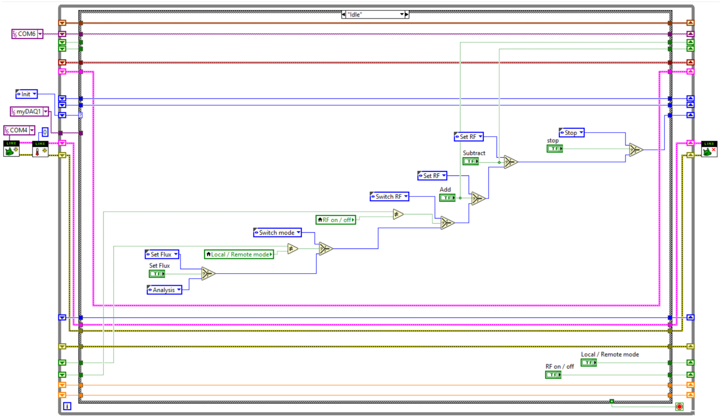

Figure 55: Idle

In the specific part that I developed, the user will have pressed the switch for remote control of the RF machine. The program is in a case (Figure 56) where it sends a message to the user warning him that he cannot return to manual control mode during the deposition phase. If yes, a string is sent which, once converted into a sequence of bits, the program interpret it as an instruction that sets the remote control.

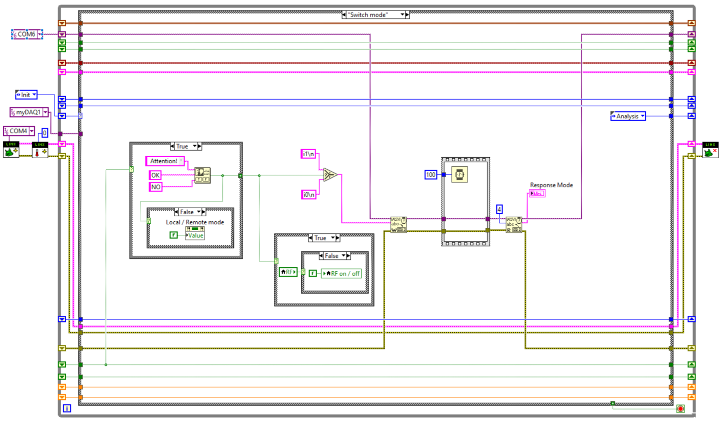

Figure 56: Switch mode

The same procedure is used to turn on the radio frequency (Figure 57a). The user will have the possibility to increase or decrease the RF value of a single unit or a value selected from a ring (Figure 57b).

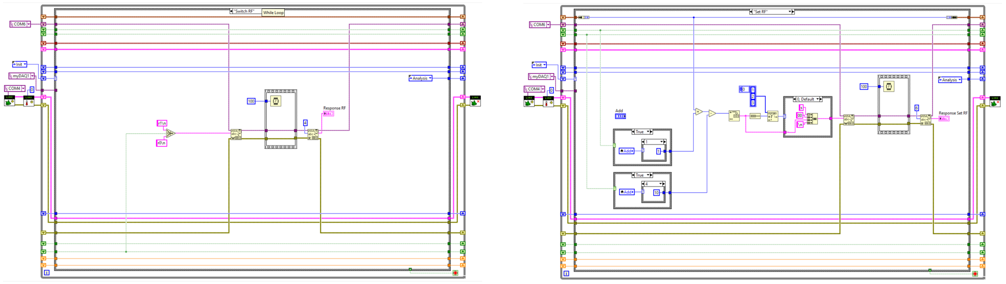

Figure 57: (a) Radio frequency switch on/off; (b) Set a value of the radio frequency

Then, on the G-control label in figure (Figure 58a), the program starts another state machine. First of all, it tells the machine that it wants to receive a response to check its status. This response is a string of 9 numbers: the first three represent the Forward power (W), the next three the Reflected power (W) and the last three a number in decimal basis. This number is converted to binary base (Figure 58b), where each bit represents a specific state (e.g., RF on/off, local/remote mode, Interlock close/open). The length of this sequence is evaluated. According to this and the value of each bit, the relative LEDs of the indicators are switched on/off (Figure 58c).

In the T-control case in figure 59, the same write and read operation is performed where additional radio frequency parameters such as DC bias (V), Tune (%) and load (%) are evaluated.

Finally, the program continues the cycle towards other cases (where analysis and display operations are carried out) until the value of the stop boolean switch will be true.

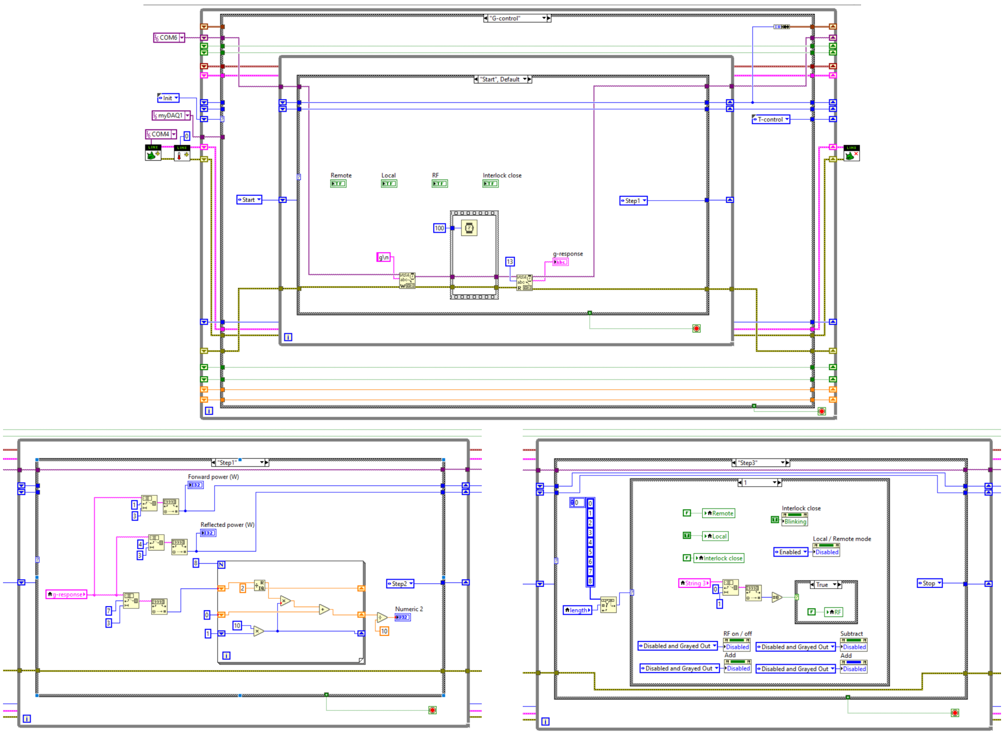

Figure 58: (a) G-control state machine; (b) String values and decimal to binary conversion; (c) Select the case based on the length of the binary sequence.

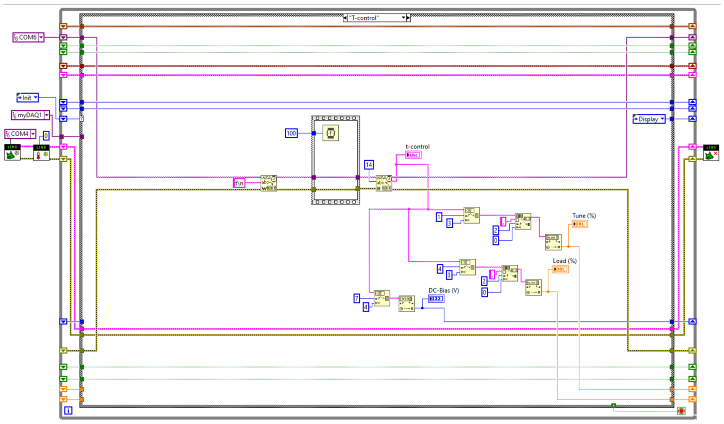

Figure 59: T-control

References

[1] The world's energy problem - Our world in data, Max Roser, 2020.

[2] Ad-Hoc Group on Science and Energy Technology (AHGSET), Committee on Energy Research and Technology (CERT), 2006

[3] Photoelectrochemical Hydrogen Production, Roel vad de Krol, Michael Gratzel, Springer, 2012.

[4] Water splitting: One way to store solar energy, Jimmy Brancho, 2015

[5] Developing new understanding of photoelectrochemical water splitting via in-situ techniques, Jiajie Cen, Qiyuan Wu, 2017

[6] Recent progress in material selection and device designs for photoelectrochemical water-splitting, I.R. Hamdani, A.N. Bhaskarwar, 2021

[7] A self-adjusting lin-long active pixel for wide dynamic range cmos image sensor, Minhaz Abedin, 2015

[8] The principle of photoelectrochemical water splitting, Peiyan Ma and Dunwei Wang, 2022

[9] Vengadesh, P. Nanocrystals — Synthesis, Characterization and Applications, 2012

[10] Recent progress in material selection and device designs for photoelectrochemical water-splitting, I.R. Hamdani, A.N. Bhaskarwar, 2021

[11] COmbined suN-Driven Oxidation and CO2 Reduction for renewable energy storage, CONDORproject.eu

[12] Enhanced photoelectrochemical hydrogen generation in neutral electrolyte using non-vacuum processed CIGS photocathodes with an earth-abundant cobalt sulfide catalyst, Mingqing Wang, Yung-Shan Chang, 2019

[13] Phase Diagram and Optical Energy Gaps for CuInyGa1-ySe2 Alloys, Tinoco, T.; Rincón, C.; Quintero, M.; Pérez, G. Sánchez, 1991

[14] Electrochemical Stability of Fluorine Doped Tin Oxide (FTO) Coating at Different pH Conditions, Alen Korjenic1 and Krishnan S Raja, 2019

[15] Molybdenum Back-Contact Optimization for CIGS Thin Film Solar Cell, Jaymin Ray, 2011

[16] Protective stainless steel micropillars for enhanced photocatalytic activity of TiO2 nanoparticles during wear, Filipp Temerova, Lena Ammosova, 2019

[17] Titanium Dioxide as a Catalyst Support in Heterogeneous Catalysis, Alexander Vorontsov, 2014

[18] Photovoltaic Properties of Aluminum Doped Zinc Oxide Electrodes Based on Variation of Aluminum Impurities in the Semiconductor, M. D. Tyona , R. U. Osuji, C. D. Lokhande, F. I. Ezema, 2018

[19] RF magnetron sputtering, Olivier BRIOT, 2018

[20] Sputtering process, sputtering deposition method, VacCoat, 2022

[21] X-ray reflection in accordance with Bragg's Law, Darrell Henry, 2004

[22] Scanning electron microscope, Wikipedia

[23] Properties of CuInGaSe2 Thin-Film Prepared from Multiple Layers via Ion Beam Sputtering Method, G.-X. Liang, 2013

[24] Growth and characterization of a CuIn0.7Ga0.3Se2/CdS photocathode, Matteo Peperoni, 2022

[25] Characterization of (CIGS)/(CdS) Hetrojunction for Solar Cell, Ikhlas H. Shallal and Balqees A. Ahmed, 2019

[26] Open Circuit Potential (OCP), Alex Peroff, 2021

[27] Linear-Sweep Voltammetry of Irreversible Electron Transfer in Surface-Confined Species Using the Marcus Theory, Douglas A. Skoog; F. James Holler; Stanley R. Crouch, 2017

[28] Bode and Nyquist Plot, Knowledge base, 2022

[29] Warburg impedance, Knowledge base, 2022